DOCTOR OF PHILOSOPHY

Electro-Optic Diagnostic Techniques For The CLIC Linear Collider

Pan, Rui

Award date:
2015

UNIVERSITY OF DUNDEE

ELECTRO-OPTIC DIAGNOSTIC TECHNIQUES FOR THE CLIC LINEAR COLLIDER

by

Rui Pan

A thesis submitted for the degree of
Doctor of Philosophy

in the
Division of Physics
School of Engineering, Physics and Mathematics
University of Dundee

May 2015

Contents

List of Figures

List of Tables

Abbreviations

BBO	β-**B**arium B**O**rate
CALIFES	**C**oncept d'**A**ccélerateur **LI**néaire pour **F**aisceau d'**E**lectrons **S**onde
CDR	**C**oherent **D**iffraction **R**adiation
CLEX	**CL**IC **EX**perimental area
CLIC	**C**ompact **LI**near **C**ollider
CSR	**C**oherent **S**ynchrotron **R**adiation
CTF3	**C**LIC **T**est **F**acility 3
CTR	**C**oherent **T**ransition **R**adiation
EO	**E**lectro-**O**ptic
EOSD	**E**lectro-**O**ptic **S**pectral **D**ecoding
EOSE	**E**lectro-**O**ptic **S**patial **E**ncoding
EOTD	**E**lectro-**O**ptic **T**emporal **D**ecoding
FEL	**F**ree **E**lectron **L**aser
FROG	**F**requency **R**esolved **O**ptical **G**ating
FWHM	**F**ull **W**idth at **H**alf **M**aximum
GaAs	**Ga**llium **As**enide
GaP	**Ga**llium **P**hosphide
ICCD	**I**ntensified **C**harge-**C**oupled **D**evice
ITO	**I**ndium-**T**in **O**xide
MCP	**M**icro **C**hannel **P**late
OTR	**O**ptical **T**ransition **R**adiation
PETS	**P**ower **E**xtraction and **T**ransfer **S**tructures
PHIN	**PH**oto **IN**jector test facility
PID	**P**roportional **I**ntegral **D**ifferential

PMT	**P**hoto **M**ultiplier **T**ube
QE	**Q**uantum **E**fficiency
RF	**R**adio **F**requency
rms	**r**oot **m**ean **s**quare
SHG	**S**econd **H**armonic **G**eneration
SVEA	**S**lowly **V**arying **E**nvelope **A**pproximation
TBL	**T**est **B**eam **L**ine
TBTS	**T**wo **B**eam **T**est **S**tand
TDC	**T**ransverse **D**eflecting **C**avity
Ti:Sa	**Ti**tanium-**Sapphire** laser
ZnTe	**Zn**c **Te**lluride

Physical Constants

Speed of Light	c	=	$2.997\ 924\ 58 \times 10^{8}\ \mathrm{ms}^{-1}$
An electron charge	e_0	=	$1.6 \times 10^{-19}\ \mathrm{C}$
An electron mass	m_e	=	$9.109 \times 10^{-31}\ \mathrm{kg}$
Vacuum permittivity	ϵ_0	=	$8.85 \times 10^{-12}\ \mathrm{Fm}^{-1}$

Acknowledgements

First of all, I would like to thank my supervisors Dr. Thibaut Lefevre, Dr. Steven P. Jamison and Prof. W. Allan Gillespie for their advice and patience on my PhD study and on this project.

I would like to thank Dr. Thibaut Lefevre for his big support on this project at CERN. Thanks for his help in connecting people, the laser lab can be build up and functioning quickly, the design of vacuum chambers can be arranged in time and manufactured. Thanks for building the laser transport beam line and aligning the laser in the accelerator with me together. His help is not only in the work but also help me integrate into the local life quickly.

I would like to thank Dr. Steven P. Jamison for his patient and professional technique support on this project. Thanks for teaching me the whole theory of the electro-optic techniques, sharing his experience on EO experiments and also providing me the opportunity in STFC Daresbury lab to train my experiment skills. Thanks for his very valuable commons and guiding me on the thesis writing.

I would like to thank Prof. W. Allan Gillespie for providing me the opportunity to start my PhD in University of Dundee and all the supports at University. Thanks for helping me deal with the paper work at the University side, then I can focus on my project study. Thanks for replying my emails very quick every time.

I have spent a wonderful time in the QP section of Beam department at CERN and Diagnostics and Lasers Group at STFC ASTeC. I would like to thank all my colleagues for their help on making a power supply for the pulse picker driver in the fibre laser, and their help on finding proper equipment and tools for the bunch profile monitor testing or experiments. My english has had a big improvement by discussing with them during the coffee time and lunch time every day.

I am very grateful to the CTF3 group for their successful operating the CALFIES beam line, and supporting my project on CALIFES. Thanks to Dr. Stefano Mazzoni for his help on streak camera measurements and EO monitor alignment. Thanks to Aurelie Noelle Goldblatt for her help on the motors conneters, controlling and also on teaching me the skills in ZEMAX simulation. Thanks to Wilfrid Farabolini for optimising and commissioning CALFIES for the bunch profile measurements and his effort on bunch compression. Thanks to Alexandra Andersson for providing timing signal for laser synchronization, and also for providing a solution for the trigger signal issue. Thanks to Dr. Mikhail Martyanov for lending me pulse picker, autocorrelator for the measurements and his inspiring discussions.

I own special thanks to Dr. David Walsh for his help on the bunch profile monitor alignment and all the valuable daily commons and discussions. Thanks to Matthew Cliffe and Dr. Edward W. Snedden for their help on the experiments at Daresbury lab. Thanks to Dr. Trina Thakker for her advice and very helpful discussion on the fibre laser selection.

I am very grateful to Prof. Carsten Walsh for running the DITANET program, in which I obtained many trainings on accelerator, beam diagnostics, and skills in scientific research. I would like to acknowledge the DITANET steering committee and the European Commission for supporting this project and supporting me to study and work in Europe. This research project has been supported by a Marie Curie Early Initial Training Network Fellowship of the European Community's Seventh Framework Programme under contract number (PITN-GA-2008-215080-DITANET)

Last but not the least, I would like to thank my family for their supporting. Special thanks to Qiongying Huang for always being there for me.

Declaration of Authorship

I, Rui Pan, declare that this thesis titled, 'ELECTRO-OPTIC DIAGNOSTIC TECHNIQUES FOR THE CLIC LINEAR COLLIDER' and the work presented in it are my own. I confirm that:

- This work was done wholly or mainly while in candidature for a research degree at University of Dundee.
- Where any part of this thesis has previously been submitted for a degree or any other qualification at this University or any other institution, this has been clearly stated.
- Where I have consulted the published work of others, this is always clearly attributed.
- Where I have quoted from the work of others, the source is always given. With the exception of such quotations, this thesis is entirely my own work.
- I have acknowledged all main sources of help.
- Where the thesis is based on work done by myself jointly with others, I have made clear exactly what was done by others and what I have contributed myself.

Signed: _____

Date: _____

I hereby certify that the candidate Rui Pan has fulfilled the conditions of the Resolution and Regulations appropriate for the degree of Doctor of Philosophy in the University of Dundee and that the candidate is qualified to submit this thesis in application for that degree.

Signed: _____

Date: _____

ELECTRO-OPTIC DIAGNOSTIC TECHNIQUES FOR THE CLIC LINEAR COLLIDER

Abstract

School of Engineering, Physics and Mathematics
University of Dundee

Doctor of Philosophy

by Rui Pan

One of the most promising devices to provide accurate measurement of the longitudinal bunch profile at the tens of femtosecond level is based on electro-optic techniques. In this thesis, a bunch profile monitor, based on electro-optic spectral decoding (EOSD), is currently developed for the CLIC Test Facility 3 at CERN. The monitor is optimised for bunch lengths over 3.5 ps with effective window of 16 ps, and sub-picosecond resolution. The measurement results from the EO monitor are compared with measurements by coherent transition radiation on a streak camera. The measurement on bunch charge dependence is studied. Timing resolution of the bunch profile monitor is studied in both theory and numerical calculation.

This thesis summarises a frequency analysis approach of electro-optic effect based on $\chi^{(2)}$ frequency mixing process. From the theory analysed in frequency domain, a non-crossed polarization measurement includes all three of the probe laser background term, the linear term to Coulomb field and the quadratic term to Coulomb field. Three methods are induced based on this frequency analysis result to retrieve Coulomb field value which is emitted from electron beam. The measured 1.3 MV/m field strength agrees with calculation result.

An experiment is designed to study the role of incident beam sizes and non-collinear incident beams in EO technique. Due to the phase matching process, the non-collinear angle of the incident beams induces a frequency dependent angular chirp in the beams emitted after the EO crystal. This frequency offset may lead to frequency loss in fibre coupling, and thus lead to bunch length broadening in a measurement for short electron bunch.

Chapter 1

Introduction

A 3 TeV e^+e^- Compact Linear Collider (CLIC) is currently being studied at CERN [1]. CLIC is based on a two-beam acceleration concept in which drive beams with high current and high bunching frequency are continuously decelerated to provide the required RF power for accelerating the colliding beams. To reach high luminosity the machine relies on nanometre transverse beam sizes. The bunch length must also be kept short to avoid any luminosity dilution [4]. The bunch length is of the order of few picoseconds in the injector complex, the bunch length is then compressed down to 150 fs rms (root mean square) just before the CLIC main linac. The beam diagnostics for longitudinal profile measurement are challenging. The shortest bunches must be measured with a resolution of 20 fs, and even at more modest sub-ps resolution, the diagnostics should be non-destructive. Only very few instruments can provide longitudinal profile measurement with femtosecond time resolution. The resolution of deflecting cavities has already been demonstrated better than 10 fs [5][6], but the measurements are destructive. Moreover, to reach similar resolution on high energy beams ($>$ 100 GeV) the devices would require the use of extremely high power or a very long deflecting cavity, which might not be practical.

A non-intercepting solution for longitudinal diagnostics can be based on the Electro-Optic (EO) technique [7]. This is based on the polarization change of a laser beam which passes through a birefringent crystal itself polarized by the Coulomb field of the electron beam. The first demonstration of EO sampling [8] [9] for electron bunch length measurement was done at FELIX, the FEL facility in the Netherlands. During the following years, EO single shot techniques have been introduced and demonstrated on several accelerators in many distinct forms, such as EO Spectral Decoding (EOSD) [10], EO Spatial Encoding (EOSE) [11], EO Temporal Decoding (EOTD) [12] and EO spectral upconversion [13].

This thesis starts with an introduction of the CLIC (Compact LInear Collider) concept, before discussing the CLIC test facility at CERN. Longitudinal bunch length diagnostics, including electro-optic methods, are reviewed in Chapter 1. Chapter 2 gives the detailed derivations of electro-optic effect in frequency domain and its applications on three distinct EO schemes. Chapter 3 demonstrates the design and implementation of an electro-optic based bunch profile monitor for CALIFES beams at CERN. Following it, Chapter 4 shows the measurement results and analysis from the bunch profile monitor as installed and commissioned. Methods for obtaining bunch Coulomb field value are also demonstrated in this chapter. An experiment on the impact of phase matching in non-collinear geometry of the EO measurement is studied in Chapter 5. The thesis ends with Chapter 6: conclusions and future perspectives.

1.1 Linear accelerator at CERN

This section presents an overview of the CLIC Test Facility 3 (CTF3) including the CALIFES beam line and how their parameters scale with the real CLIC design.

1.1.1 CLIC

The CLIC study aims at a centre-of-mass collision of multi-TeV (optimized on 3 TeV) e^+e^- collider. Considering the costing and size for this high energy purpose, a 100 MV/m accelerating gradient is required. However the only options for klystrons, as RF power sources, on the market cannot meet the CLIC requirement. Therefore a two-beam acceleration technique is used to optimize the production and the distribution of the required RF power on CLIC. The basic concept of the two-beam acceleration techniques is to use low energy long pulse klystrons to produce a drive beam. The drive beam is then decelerated and its power is extracted to accelerate the main beam through the power extraction and transfer structures (PETS). In this way, the drive beam can produce the required gradient for accelerating the main beam. A general layout of the CLIC complex is depicted in figure 1.1.

The drive beam is a 100 A peak current, 2.4 GeV energy, and time compressed beam running parallel to the main beam. When the drive beam is decelerated in PETS, it generates RF power with a high current and high bunching frequency, which is used to accelerate the main beam. The drive beam complex can thus

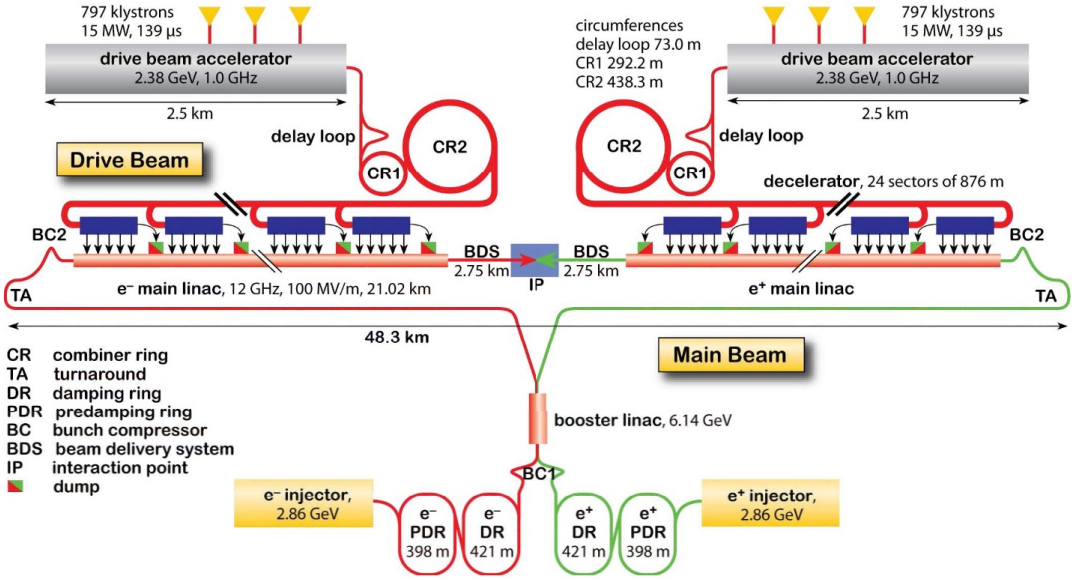

FIGURE 1.1: Layout of the 3 TeV CLIC Complex [1]: drive beam is accelerated by klystrons and beam bunch frequency is multiplied by the delay loop and combiner rings (CR). Then the drive beam is sent down to decelerator sectors. Its energy is extracted and is transferred to accelerate the main beam. The main beam is generated from injector linac. After the pre-damping ring (PDR) and damping ring (DR), the beam bunch is compressed by bunch compressor (BC) and accelerated by booster linac. Then the main beam is sent to the main linac to be accelerated to 1.5 TeV after the turnaround (TA) loop. After the beam delivery system (BDS), the beam is collided at the interaction point (IP).

be seen as a power source, and is equivalent to a 12 GHz relativistic klystron distributed over a distance of 48 km. To obtain the high current and high frequency, the electron pulses in the drive beam are compressed and bunch frequency is multiplied by going through the delay loop and combiner rings. Once the drive beam trains have been combined, they are sent down to the CLIC tunnel and distributed to their respective decelerator sectors using turn-around loops. Bunches are further compressed just before and after the turn-around loops. In the decelerator sector, the beam energy is gradually transformed into 12 GHz RF power over some hundreds of meters.

The main beam is generated and pre-accelerated in the injector linacs. From the exit of the damping rings, the main beam bunches are compressed in a first magnetic chicane, accelerated in a booster linac and transferred to the entrance of the main linac through more than 20 km of beam line. After a final 1.5 km long turn-around loop, bunches are compressed even further in a second magnetic chicane to a final bunch length of 147 fs rms. The beam is then accelerated in the Main Linac. The beam energy rises up to 1.5 TeV over a total distance of 20.5 km. Along the entire Linac, the beam properties (beam position, current, emittance,

TABLE 1.1: Longitudinal beam profile requirement for CLIC

Sub-systems	Bunch length [ps] rms.	Resolution [ps] rms.
	Main Beam	
e^- Injector Complex	17	2
e^+ Injector Complex	37	5
Injector Linac (e^-/e^+)	3	0.5
Pre-Damping Rings	17	2
Damping Rings	5	0.5
Bunch Compressors 1	1	0.1
Booster Linac	1	0.1
Transfer Lines	1	0.1
Bunch Compressors 2	0.15	0.02
Main Linac	0.15	0.02
Beam Delivery System	0.15	0.02
	Drive Beam	
Source and Linac	13	1
Delay Loops	7	1
Combiner Rings	7	
Transfer to tunnel	7	1
Bunch compressors	3-7	
Turnarounds	5	0.5
Decelerator	3	0.5
Dump lines	3	0.5

losses and bunch length) must be measured in a non-interceptive way to guarantee the overall performance of the machine and provide reliable information for feedback systems. The beam is finally transported through the Beam Delivery System (BDS) to the Interaction Point. After collisions, the beam, highly disrupted is then guided toward a huge water dump.

In order to make the complex collider becomes possible, precise beam instrumentations are required for beam dynamic consideration. The full knowledge of longitudinal bunch profile is necessary for tuning of the system. From the scheme of CLIC in year of 2012, 312 bunch profile (length) monitors are required for the Drive Beam and 75 for the Main Beam. The longitudinal beam profile requirement for CLIC is shown in table 1.1.

1.1.2 CTF3

A test facility for the CLIC scheme, CTF3, is located at CERN. A layout of CTF3 complex is depicted in figure 1.2. The accelerator drive beam in CTF3

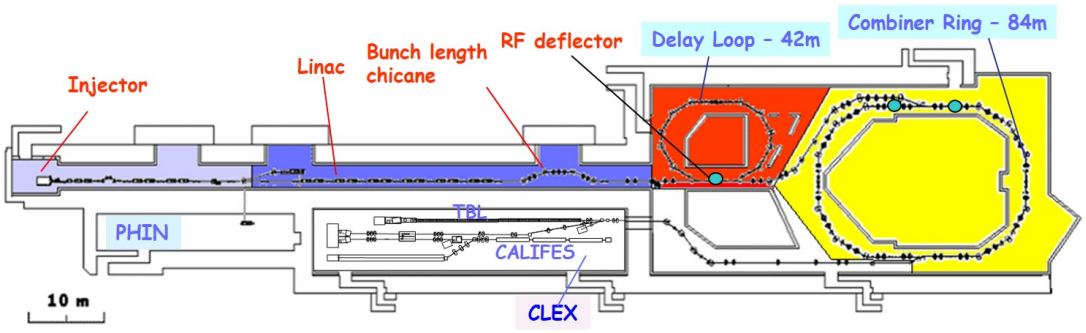

FIGURE 1.2: A schematic layout of CTF3 [2]: the accelerator drive beam starts from an injector and a linear accelerator (Linac). Following by a 42 m long Delay Loop and a 84 m long Combiner Ring, the beam current and bunch frequency of the drive beam are multiplied. The drive beam is provided to a CLic EXperimental area (CLEX). CLEX includes Test Beam Line (TBL), Two Beam Test Stand (TBTS), and CALIFES beam line. The PHIN area is a PHoto Injector test facility.

starts with an injector and a linear accelerator. Following by a 42 m long Delay Loop and an 84 m long Combiner Ring, the beam current and bunch frequency of the drive beam are multiplied. A 30 ampere drive beam with 12 GHz bunch repetition frequency can be provided to a CLic EXperimental area (CLEX). The PHIN area is a PHoto Injector test facility.

CLEX includes several beam lines to test the two beams acceleration scheme for CLIC, and also to test CLIC critical components and diagnostic. A small-scale version of a CLIC decelerator which includes 16 consecutive PETS is currently under test to study the efficiency of the drive beam deceleration in the so-called Test Beam Line (TBL)[14]. The main motivation is to produce a constant power production while maintaining the drive beam stable, with a minimum of particle losses. The two-beam concept is also studied experimentally in the Two Beam Test Stand (TBTS), where both the drive beam and a probe beam travel simultaneously in a CLIC module, passing through decelerating and accelerating structures respectively. The probe beam line, known as CALIFES, starts with a RF photo-injector, followed by 3 GHz accelerating structures taking the beam energy up to 200 MeV. The CALIFES beam line is also used as a diagnostic test bench.

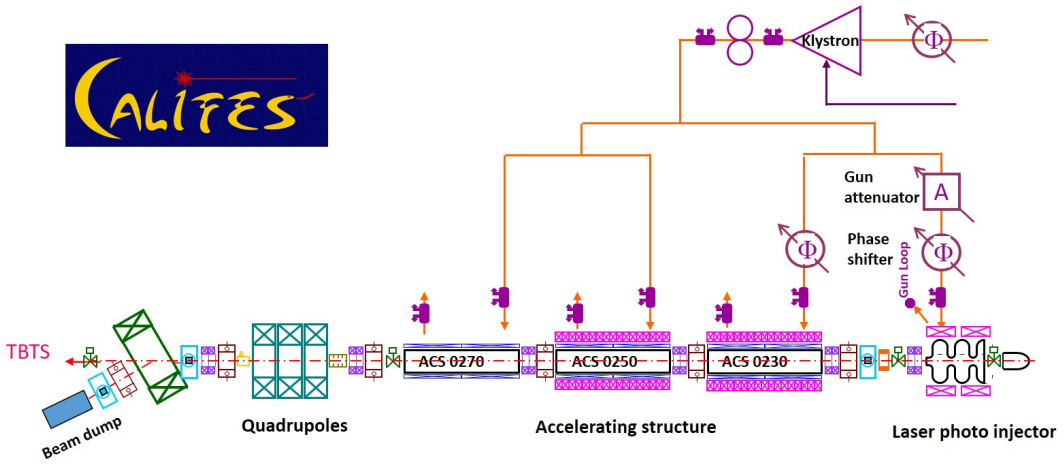

FIGURE 1.3: CALIFES layout[3]: the probe beam line is composed of one photo-injector, three travelling-wave structures, and one section equipped with beam diagnostics. The beam is then sent into TBTS.

1.1.3 CALIFES

The layout of the CALIFES beam line is depicted in figure 1.3. The accelerator is composed of one photo-injector, three travelling-wave structures, and one section equipped with beam diagnostics. The beam is then sent into TBTS where it can be accelerated in CLIC-type accelerating structures. The photo-injector uses a Cs_2Te photocathode illuminated by 262 nm laser pulses [15][16]. Typical bunches in CALIFES have a charge ranging from 85 to 600 pC depending on the laser pulse energy and the quantum efficiency of the photo-cathode. The electron bunch length, initially of 14.1 ps FWHM (Full Width at Half Maximum), is compressed using velocity bunching in the first accelerating structure and in normal conditions the bunches at the end of the linac are 6-7 ps FWHM. The machine can be run either in a single bunch mode, or a multi bunch mode with a typical pulse train consisting of 226 bunches over 150 ns at 5 Hz repetition rate. The RF system of CALIFES relies on a single klystron equipped with pulse compression and providing an RF pulse of 45 MW within 5.5 μs. The beam energy can reach up to 200 MeV at the end of the linac. Immediately afterwards, the beam enters a diagnostic section including emittance, bunch length and energy spread measurements.

1.2 Methods for bunch longitudinal profile measurement

Several techniques are capable of measuring the bunch length or longitudinal profile with a sub-picosecond resolution, such as coherent synchrotron radiation (CSR) [17], coherent transition radiation (CTR) [18] [19], coherent diffraction radiation (CDR) [20][21], or transverse deflecting cavity (TDC) [5][6][22].

Coherent radiation can be generated by a short bunch of an electron beam at the wavelengths longer than bunch length. The intensity of the coherent radiation is enhanced because its power is proportional to the square of the number of electrons within the bunch. In order to obtain bunch length information, which can be derived from the coherent radiation spectrum, the spectrum is usually measured by a Michelson interferometer or grating spectrometer. In another way, the bunch length can also be directly measured by observing the optical synchrotron or transition radiation with a streak camera.

Synchrotron radiation is generated when relativistic electron bunch is deflected in bending magnets. Optical transition radiation appears when a charged particle crosses inhomogeneous media, a boundary of two media for instance. Transition radiation is a destructive measurement, while CDR and CSR are non-intercepting (and largely non-invasive) diagnostics. Diffraction radiation appears when a charged beam passes through an aperture in a metallic screen due to the interaction of the electromagnetic field of the charge with the boundary. If the screen is a slit between two semi-planes, radiation is induced by the current changing in time on the screen. The two cones of induced radiation propagate in the backward direction of specular reflection generate an interference pattern, which includes the bunch information. Comparing to CTR, the impact of CDR on a particle beam is significantly reduced.

Two further methods of bunch length measurement are installed on CALIFES [23]. One uses a deflecting cavity driven by an additional klystron. When the beam passes through the cavity, the particles experience a time-varying kick. The longitudinal profile of the beam is thus transformed into a transverse profile and can be measured by imaging on an optical transition radiation screen downstream. In order to achieve fs resolution, TDC requires several meters long cavity and over 10 GHz RF frequency for GeV beam energy[24]. The other monitor measures the beam energy dispersion introduced intentionally by the CLIC acceleration in the two-beam test stand. When the beam goes through the accelerating structure, the particles experience a time-varying acceleration (or deceleration) depending

on the relative phase difference between the RF and the beam. The corresponding increase in energy spread is measured in a spectrometer line and provides a measurement of the bunch length. However, these two monitors require either the presence of the drive beam to power the accelerating structure or an extra driving klystron which is currently used for the regular operation of the CTF3 drive beam. In addition, both of these two methods are destructive. There is then a strong requirement to build a dedicated bunch profile monitor for CALIFES.

1.3 Electro-optic bunch profile measurements

Electro-optic diagnostics has been widely used in many institutes, laboratories or on accelerators, such as FELIX in Netherlands [25], BNL in USA [26], DESY in Germany [27],PSI in Switzerland [28], Fermilab in USA [29], SLAC in USA [30], SPring-8 in Japan [31], Daresbury Lab in UK [32], CERN in Switzerland/France [33], ELYSE in France [34], UCLA Pegasus photo-injector laboratory in USA [35], Sincrotrone Trieste Laboratory in Italy [36], SPARC-LAB in Italy [37], and KIT in Germany [38].

Electro-optic bunch profile monitors are relying on the same technique as used in Teraherz (THz) wave detection, electro-optic sampling. A paper about free-space electro-optic sampling of THz beams was published in 1995 by Q. Wu and X.-C. Zhang [39]. This setup was based on the linear electro-optic effect (Pockels effect) which converts the THz electric field into laser polarization variation. In their set-up, a picosecond long THz wave, generated by a gallium arsenide (GaAs) photoconductive emitter, was scanned by 150 fs long laser pulses in a 500 μm thick $LiTaO_3$ crystal. The delay of the probe laser pulse was controlled by a mechanical translation stage. In the following, zinc telluride (ZnTe) crystal and gallium phosphide (GaP) crystal are mainly used in THz spectroscopy.

An application of EO technique for bunch profile measurement based on EO sampling is reported by D. Oepts et al at the FELIX FEL facility in the Netherlands in 1999 [8]. A 0.5 mm thick ZnTe crystal is used to detect 12 kV/cm THz field strength by a 12 fs laser pulse at 800 nm centre wavelength. The EO sampling scheme is shown in figure 1.4. The ultrafast laser is used as probe to measure a several-ps Coulomb field profile. The arrival time of the probe laser can be controlled by an optical delay stage. A polarizer, setting in front of the crystal, can guarantee the incident laser is linearly polarized. In the EO crystal, the probe polarization is changed by the applied Coulomb field. The second polarizer analyses the polarization varies. Each time, the probe laser detects one specific time

point of the Coulomb field profile. The whole bunch profile can be reconstructed by using probe to scan through the Coulomb field profile. Since EO sampling is not a single-shot technique, timing jitter between laser probe and e-bunch plays a role in the measurement. A better signal to noise ratio, comparing to other EO techniques, is its advantage, because the signal intensity at each scanning point contributes to the entire probe pulse energy. It can also have a long scanning window up to tens of pico-second. EO sampling has also been applied in other diagnostics for electron bunches, such as wakefield measurement[9][40][29].

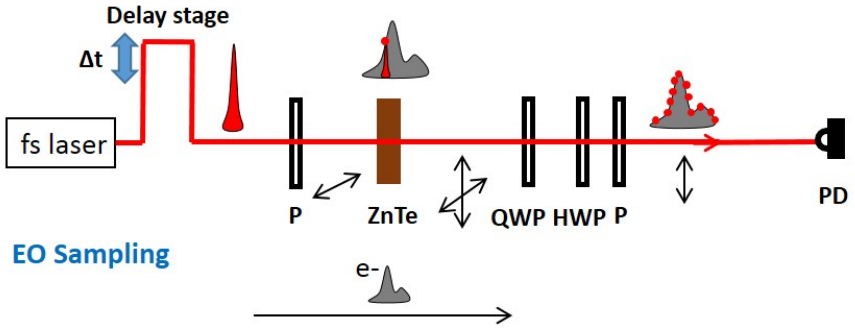

FIGURE 1.4: EO sampling scheme (P: Polarizer, QWP: Quarter-wave plate, HWP: Half-wave plate, PD: Photo Diode.)

A single-shot concept of THz detection was reported by Galvanaoskas et al in 1991[41]. In 1998, the single-shot detection of THz was also reported by Zhiping Jiang et al[42][43]. This detection technique encodes the THz profile into a laser pulse which has been chirped to several picoseconds long by a pair of gratings and is detected by a spectrometer and a camera. In 2002, a similar single shot EO technique was applied for bunch profile measurement by I. Wilke et al at FELIX FEL facility [10]. In this measurement, 30 fs laser pulses were linearly chirped to 20 ps (FWHM) duration and sent through a 0.5 mm thick ZnTe which is placed in the accelerator and used to interact with the Coulomb field. Since the bunch profile is encoded in the chirped laser pulse, and the time information is finally decoded from the laser spectrum, this EO measurement is called spectral decoding (EOSD). The EOSD scheme is shown in figure 1.5. EOSD has a simple set up including a wavelength stretcher, EO crystal and crossed-polarizers detection. It is fundamentally limited in its time resolution through the frequency-time mapping process[44][45]. While the precise value of the time resolution limit depends on the laser parameters in a given implementation, in practice the resolution is usually larger than 500 fs. This will be discussed in details in section 2.4.4.

A single-shot spatio-temporal THz field imaging technique was demonstrated by Zhiping Jiang et al. in 1998 [43], which implies a starting of applying spatial single-shot techniques. In 2000, a new EO single-shot technique relying on a

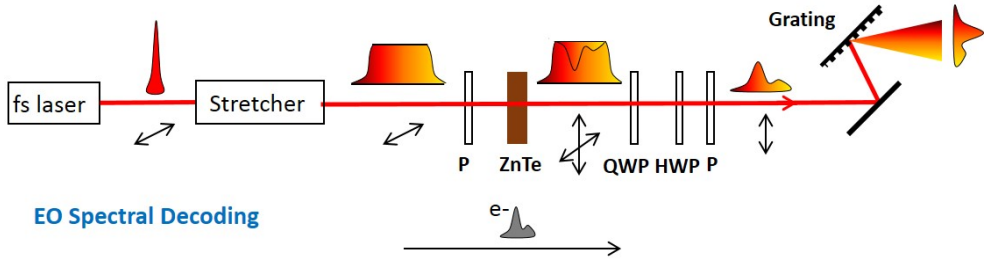

FIGURE 1.5: EO Spectral Decoding scheme (P: Polarizer, QWP: Quarter-wave plate, HWP: Half-wave plate.)

non-collinear geometry was reported by Jie Shan et al [46] for the THz beam detection. Several demonstrations of spatial single-shot detection were developed and applied in bunch profile measurements[47][30][26]. This technique, known as Electro Optic Spatial Encoding (EOSE) was also applied for jitter measurements between the electron bunch and the laser pulse at DESY by A.Azima in 2006[11]. One of the EOSE schemes is shown in figure 1.6. In this measurement, an ultrashort laser pulse with a large ($\approx$ 5 mm) transverse beam size interacts with the Coulomb field pulse in a non-collinear geometry. This arrangement leads to a time-space mapping of the EO interaction, as different transverse parts of the probe arrive at the EO crystal with different time delays. Through imaging of the probe beam, and using of polarization optics to convert the EO interaction into an optical intensity variation, it becomes possible to read out the effect of the EO interaction as a function of time.

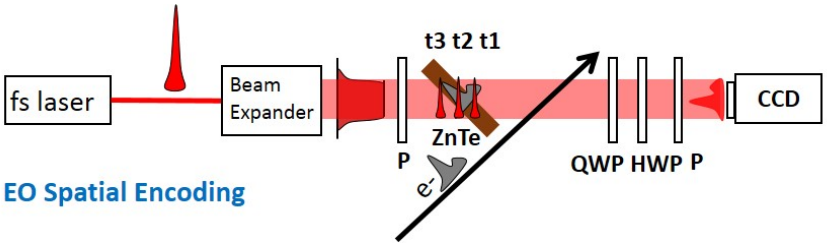

FIGURE 1.6: EO Spatial Encoding scheme (P: Polarizer, QWP: Quarter-wave plate, HWP: Half-wave plate.)

A high temporal resolution, single shot characterization technique for THz pulse was demonstrated in 2003 [48]. This technique, named electro-optic temporal decoding (EOTD), was applied in bunch temporal profile measurement by G. Berden, et al. at FELIX in 2004[12]. The shortest bunch lengths can be measured down to 60 fs rms by a 65 μm GaP [5][27] and 170 fs rms by a 300 μm ZnTe [49]. The resolution of EOTD is limited by the lowest resonance of EO material. The EOTD scheme is shown in figure 1.7. In temporal decoding, the ultrafast optical beam is split into two separate beams, a probe and a gate. The probe is stretched to a pulse length of typically 20 ps, for example by passing through

a grating pair. This stretched probe pulse is focused at the electro-optic crystal inside the accelerator beam pipe at the measurement location, and samples the bunch-induced birefringence in the electro-optic crystal. The stretched duration sets the time window for the measurement. The phase retardation induced in the crystal by the bunch field is translated into an intensity modulation on the stretched pulse by passing it through an arrangement of polarizers. The decoding process is through an optical cross correlation measurement, where the gate beam serves as a short-pulse reference. The cross-correlator produces a time-space mapping in a similar way to that described for EOSE. This encoded intensity is then cross-correlated with the short pulse in a β-Barium Borate (BBO) crystal. The non-collinear nature of the cross correlation geometry provides a mapping of time to spatial position in the BBO crystal and the CCD. EOTD requires high power laser for the reading out. The probe laser typically used for EOTD is an amplified Ti:Sa laser with pulse length of a few tens of femto-second, centre wavelength at 800 nm and pulse energy >1 mJ. The EOTD technique overcomes the time resolution limit in EOSD technique by reading the signal from time domain instead of reading it from frequency domain.

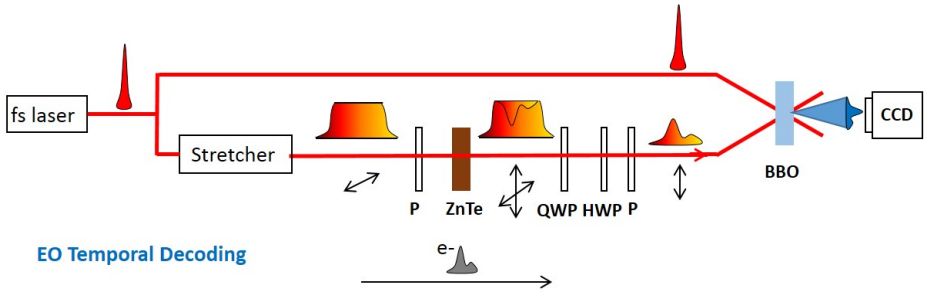

FIGURE 1.7: EO Temporal Decoding scheme (P: Polarizer, QWP: Quarter-wave plate, HWP: Half-wave plate, BBO: β-Barium Borate crystal.)

In 2010, S.P. Jamison et al observed $\chi^{(2)}$ sum and difference frequency mixing induced spectral broadening of a narrow bandwidth probe by measuring Coulomb field of an electron bunch, and proposed a new method, spectral upconversion, for bunch profile measurement with a very narrow-band laser probe[13]. The sideband generation concept was also examined for spectral resolution, sideband amplitude and the effects of probe timing with a laser-driven broadband THz source by J. van Tilborg et al [50]. The EO spectral upconversion scheme is shown in figure 1.8. Due to the frequency mixing process, the sum- and difference-frequencies $\omega_{opt} \pm \omega_{THz}$ can be observed. Then the spectrum intensity of the THz wave (Coulomb field induced), including bunch profile information, is shifted to the probe optical region, and can be observed, but the spectral phase information is lost. In order to obtain the bunch temporal information, the spectral

phase information needs to be retrieved. The phase retrieval technique by frequency resolved optical gating (FROG) for the upconversion method was studied in [51][52][53].

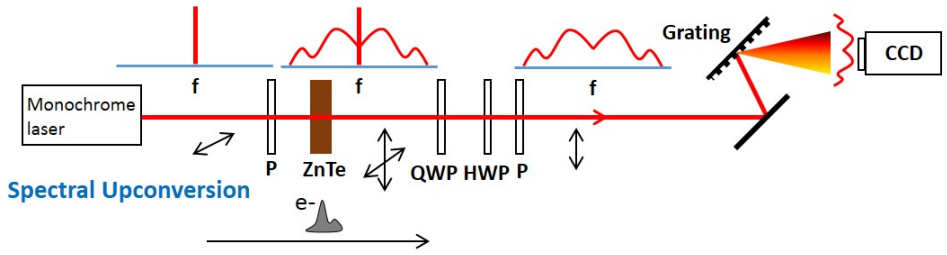

FIGURE 1.8: EO Spectral Upconversion scheme (P: Polarizer, QWP: Quarter-wave plate, HWP: Half-wave plate.)

As fibre laser technology has developed, Ytterbium fibre lasers have been employed in the bunch profile measurements, alternating the high-costing and complex Ti:Sa lasers in 2007[54]. In the following years, a compact EO bunch profile monitor, based on EO sampling and EOSD scheme, was demonstrated in [55][56][57] for SwissFEL. The monitor integrates all the required mirrors, polarizers, wave plates, splitters and EO crystal in a 418 mm by 123 mm area. A 0.5 mm GaP crystal is applied and its back is coated by reflective coating in order to save a second mirror for extraction. The laser is coupled in and out of the monitor by optical fibres.

A design of a novel EO based 3D bunch charge distribution monitor was introduced in 2007 by H. Tomizawa and his co-workers for SPring-8 [58]. In the design, eight EO crystals are assembled surrounding the e-beam axis radially. The EO signals from the eight channels are encoded in one chirped broadband laser pulse on different wavelengths. Finally the longitudinal and transverse bunch charge distributions are restructured with tens of femto-second resolution within a single shot. The feasibility test by two ZnTe crystals has been done in 2010 [59]. A single organic DAST crystal was applied in bunch measurement and a EO based timing feedback system was built in 2012 [60]. The monitor requested octave 300 nm broadband probe pulse with a linear chirp rate of 1 fs/nm was demonstrated in 2013 [31].

1.4 Project aims

In the framework of the Compact Linear Collider (CLIC) study, the main electron beam will have a bunch length as short as 150 fs rms. The requirement is to

measure the detailed longitudinal profile of the bunch with a resolution of 20 fs rms. In parts of machine, the bunch length is > 1 ps, and a non-invasive bunch profile monitor is also required. A full knowledge of the bunch profile is desired rather than just the value of the bunch length, and the measurement must be totally non-intercepting. The optimum solution to this problem is electro-optic measurement of the bunch Coulomb field, which can yield very reliable results at CLIC parameters.

The research carried out within the PhD project described here is based on designing, implementation and testing an EO bunch profile monitor for the CALIFES beam of CTF3 at CERN. The new monitor is the first bunch profile monitor based on EO technique in CTF3. The feasibility of applying EO technique on CLIC can be tested by studying and evaluating the performance of the EO bunch profile monitor on CALIFES beams.

Among all the EO techniques, the EO sampling provides best signal to noise ratio since the full laser pulse energy is used to measure one sample point of a profile. However the EO sampling is not a single shot technique, therefore the bunch by bunch position jitter, timing jitter, charge jitter play an important role in the bunch profile measurement. The EOTD overcomes the short bunch broadening limitation which is described in Chapter 2, and provides the best temporal resolution among all EO techniques. To achieve a cross auto-correlation measurement for the EO signal, it requires powerful laser source. The laser source is usually Ti:Sa laser with pulse energy >1 mJ, which is not available at CTF3. The EO spectral upconversion also requires a powerful monochrome laser source, which makes it being out of the choice for CALIFES. The EOSE provides a simple setup to measure the bunch profile. However due to its non-linear incident beams scheme and the phase mismatching in the EO crystal, the measured profile is distorted. The EOSD has a relative simple scheme and requires only several nJ pulse energy, therefore a economical ultrafast fibre laser can be used for the laser source and it is practical at CTF3. The EOSD scheme is finally chosen as scheme of the bunch profile monitor for CALFIES. The details of the monitor is discussed in Chapter 3.

Chapter 2

Theoretical background

The description of electro-optic (EO) process can be given as a time varying refractive index, or as a non-linear frequency mixing process. The refractive index method has been developed by several researchers [61][62][63][64], and is widely used. The theory can well describe any anisotropic/isotropic EO crystal, any possible probe propagation direction, polarization and also arbitrary direction of the THz wave. It is suitable for complex detection geometries.

The linear electro-optic effect can be seen as a low frequency approximation of the three-wave mixing. The method of frequency domain analysis[65][66][13] can provide a general result for the EO effect. This result can be used to describe not only EO sampling, but also single-shot THz detection techniques. With the weak THz signal approximation, the frequency analysis result is consistent with the refractive index analysis method. The frequency analysis approach can be also used to describe an intense incident THz signal with an extension [67]. However, the intense THz incident beam is not the case in this thesis.

This chapter presents theoretical background of EO bunch profile measurement, the EO principle, its detection and limitations, based on frequency analysis method. Its applications on EO sampling, EO spectral decoding and EO spectral upconversion are also discussed.

2.1 Bunch profile and its Coulomb field

An EO bunch profile monitor measures the Coulomb field of a charged relativistic particle bunch. The similarity between the Coulomb field and electron bunch itself depends on the beam energy and observation position. The distinction

between bunch density and Coulomb field longitudinal profile must be taken into account as it may degrade the absolute time resolution of the monitor. For a non-relativistic particle, the Coulomb field is homogeneously distributed around the particle and will not be representative of the bunch longitudinal profile. However, when an electron is moving close to the velocity of light, its Coulomb field is compacted, perpendicular to its direction of propagation with an opening angle $\theta = \frac{2}{\gamma}$ [68], where γ is the relativistic Lorenz factor $\gamma = \frac{1}{\sqrt{1-\left(\frac{\nu}{c}\right)^2}}$ and ν, c are the velocity of particle and light respectively. At very high energy, hundreds of MeV for instance, the opening angle becomes so small that the profile of the Coulomb field becomes an almost perfect replica of the bunch temporal profile. The Coulomb field of an electron can be described as:

$$\boldsymbol{E}_{\mathrm{e0}}(\boldsymbol{r}) = \frac{e_0}{4\pi\epsilon_0} \cdot \frac{1}{\gamma^2\left(1-\beta^2\sin^2\psi\right)^{3/2}} \cdot \frac{\boldsymbol{r}}{r^3}, \tag{2.1}$$

where $\boldsymbol{r}$ is the vector from the electron to an observation point, ψ is the angle between the electron direction of motion and $\boldsymbol{r}$, e_0 is the charge of an electron, ϵ_0 is vacuum permittivity and $\beta = \nu/c$. Comparing longitudinal motion direction ($\psi = 0, \pi$) with transverse radial direction ($\psi = \pi/2$), the electric field strength in the longitudinal polarization is $1/\gamma^3$ of the transverse field strength. Therefore, for a relativistic particle, the longitudinal electric field component can usually be neglected.

Only considering the transverse component, equation 2.1 is transformed into cylindrical coordinates at a radial displacement r_0 from the beam propagation path. Its field strength can be written as:

$$E_{\mathrm{e0}}(r_0, t) = \frac{e_0\gamma}{4\pi\epsilon_0} \cdot \frac{r_0}{\left(r_0^2 + \gamma^2\nu^2\left(t-t_0\right)^2\right)^{3/2}}, \tag{2.2}$$

where is assumed that the electron has a constant speed ν moving along the longitudinal direction, and t is the time in longitudinal direction, centred at $t = t_0$.

Equation 2.2 can be Fourier transformed into the frequency domain to give $\widetilde{E}_{\mathrm{e0}}(r_0, \omega) = \mathrm{FT}\left[E_{\mathrm{e0}}(r_0, t)\right]$:

$$\widetilde{E}_{\mathrm{e0}}(r_0, \omega) = \frac{e_0}{4\pi\epsilon_0} \cdot \frac{1}{\gamma\nu^2} \cdot \sqrt{\frac{2}{\pi}}|\omega|\boldsymbol{K}_1\left(\frac{r_0}{\gamma\nu}|\omega|\right), \tag{2.3}$$

where $\boldsymbol{K}_1$ is a modified Bessel function of the second kind. Based on the equation 2.3, the radially offset Coulomb field spectrum for one electron is as shown in the

figure 2.1. The calculation is based on 200 MeV electron energy at observation positions of 1 mm to 6 mm offset to electron propagation axis. The plots highlight that the high frequency components decay as the offset distance increases. Frequency bandwidth is reduced from 15 THz at 1 mm offset to 3 THz at 6 mm offset (FWHM). This bandwidth narrowing leads to temporal profile broadening. Therefore, better timing resolution can be obtained with the observation point closer to the beam.

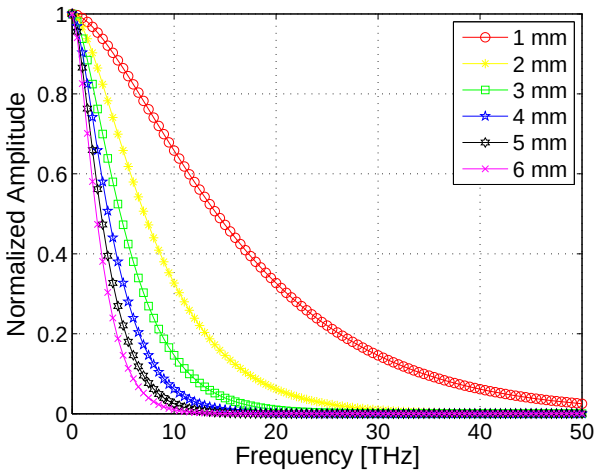

FIGURE 2.1: Coulomb field spectrum of one electron. Electron energy is 200 MeV, observe position offset to axis is from 1 mm to 6 mm.

To calculate the Coulomb field of an electron bunch, an electron density distribution function $\rho(t)$ is introduced. A bunch total field can be described by a convolution of one electron field with the electron density distribution:

$$E_{\text{Colm}}(r_0, t) = E_{\text{e0}}(r_0, t) * \rho(t). \tag{2.4}$$

An an example calculation of the Coulomb field, a Gaussian electron density distribution with duration σ_0 is supposed here. Then, with bunch charge Q, the charge density $\rho(t)$ can be expressed as

$$\rho(t) = \frac{1}{\sqrt{\pi}\sigma_0} \cdot \frac{Q}{e_0} \cdot e^{-\frac{(t-t_0)^2}{\sigma_0^2}}. \tag{2.5}$$

Figure 2.2 shows Coulomb field broadening and its amplitude, with varies of bunch lengths, beam energy, and radial offset as calculated using equation 2.4 and 2.5. A broadening ratio is defined as broadened length (τ) over original length (τ_0), and radial offset is the distance between an observation point and the center of an bunch. The bunch length and pulse length, mentioned in this thesis, are

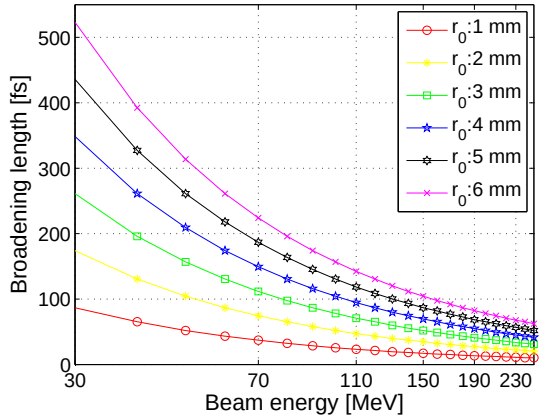

(a)

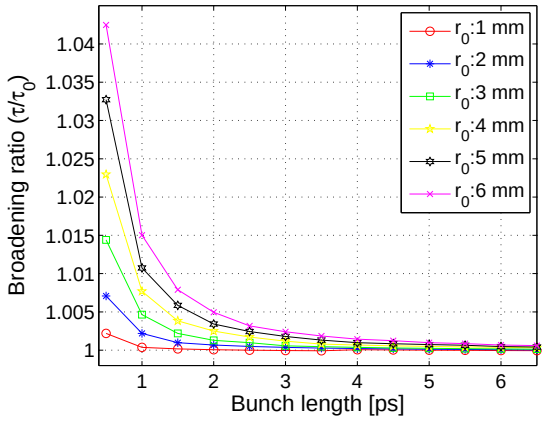

(b)

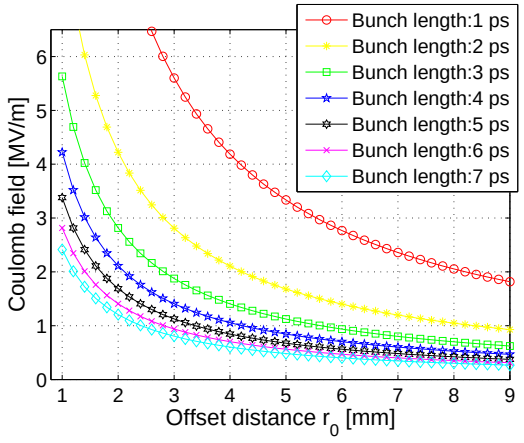

(c)

FIGURE 2.2: Calculation on Coulomb field broadening ratio and amplitude with bunch charge, bunch length (FWHM), beam energy, and radial offset: (a) Coulomb field broaden length for one electron as function of beam energy from 30 MeV to 250 MeV, for radial offset from 1 mm to 6 mm; (b) Relative increase in Coulomb field duration as function of bunch length for radial offset from 1 mm to 6 mm. Bunch charge = 0.3 nC, and beam energy = 200 MeV; (c) Coulomb field amplitude as function of radial offset for bunch charge 0.3 nC, Bunch length from 1 ps to 7 ps, and beam energy = 200 MeV.

defined by full width at half maximum (FWHM), unless specifically mentioned otherwise. Figure 2.2(a) shows the broadening length, as calculated from equation 2.2, for one electron as function of beam energy for radial offset from 1 mm to 6 mm. It can be seen that for an electron bunch with 200 MeV energy at offset position of 2 mm, the broadening length is only 22 fs. The broadening increases with the radial offset. In these calculations the beam is assumed to be entirely on-axis, with no radial extent. The broadening ratio (τ/τ_0) as function of the transverse offset is shown in figure 2.2(b). For a short bunch less than 1 ps length, the broadening is more obvious. While for a long bunch, such as 6 ps, the broadening is less than 0.2%. The calculations are done under condition of 0.3 nC bunch charge and 200 MeV beam energy. Figure 2.2(c) shows the amplitude of the Coulomb field for different distances of the observer from the electron bunch and gives a reference for the Coulomb field generated by 0.3 nC bunch charge and bunch length from 1 ps to 7 ps. Taking CALIFES parameters as an example, the Coulomb field at 2 mm offset, with 0.3 nC bunch charge, 6 ps bunch length and 200 MeV beam energy, is 1.4 MV/m. Since the Coulomb field is proportional to the bunch charge, then the Coulomb field strength with same bunch length but different charges can be easily calculated. The optimum distance of the observer position would depend on a compromise among the expected time resolution, the signal to noise ratio of the EO monitor and the risk of damaging the crystal if the beam directly impinges on it.

2.2 Linear electro-optic effect

The electro-optic effect describes the change of a material refractive index induced by applying a static or slowly varying electric field on it. Historically the linear electro-optic effect is explained by the index ellipsoid. In an anisotropic optical medium, the electric displacement D and electric field E has a relationship of

$$D_i = \epsilon_0 \sum_j \epsilon_{ij} E_j. \tag{2.6}$$

For a lossless and non-optically active material, the dielectric permeability tensor ϵ_{ij} has only 6 independent elements, ϵ_{xx}, ϵ_{yy}, ϵ_{zz}, $\epsilon_{xy} = \epsilon_{yx}$, $\epsilon_{xz} = \epsilon_{zx}$, and $\epsilon_{yz} = \epsilon_{zy}$, because of its symmetry. There is a new coordinate system, the principal

axis system, can always be found to show the relationship as:

$$\begin{bmatrix} D_X \\ D_Y \\ D_Z \end{bmatrix} = \epsilon_0 \begin{bmatrix} \epsilon_{XX} & 0 & 0 \\ 0 & \epsilon_{YY} & 0 \\ 0 & 0 & \epsilon_{ZZ} \end{bmatrix} \begin{bmatrix} E_X \\ E_Y \\ E_Z \end{bmatrix}. \tag{2.7}$$

As described in [69], the impermeability tensor is defined as $\eta_{ij} = \frac{1}{\epsilon_{ij}} = \frac{1}{n_{ij}^2}$. The impermeability η_{ij} can also be expressed by a series expansion with an applied electric field,

$$\eta_{ij} = \eta_{ij}^{(0)} + \sum_k r_{ijk} E_k + \sum_{k,l} s_{ijkl} E_k E_l + \cdots, \tag{2.8}$$

where the r_{ijk} describes the Pockels effect (linear electro-optic effect) and s_{ijkl} describes the Kerr effect, called Pockels and Kerr coefficients respectively. As defined above, the r_{ijk} has only six independent elements and conventionally expressed as $r_{hk}, h = 1, 2, 3, 4, 5, 6$, where it is defined that the each component x,y and z: $xx \to 1$, $yy \to 2$, $zz \to 3$, $yz = zy \to 4$, $xz = zx \to 5$ and $xy = yx \to 6$. .

2.2.1 Review on Pockels effect in ZnTe and GaP crystal

To apply the EO effect as a bunch profile monitor, ZnTe or GaP crystals are commonly used. Because of a high symmetry in the zinc blende structure crystals ($\bar{4}3m$ point group), the Pockels coefficients have only one independent element $r_{41} = r_{52} = r_{63}$ and can be easily expressed by

$$r_{ijk} = \begin{cases} r_{41} & : i \neq j \neq k \\ 0 & : \text{others.} \end{cases} \tag{2.9}$$

Therefore the impermeability tensor can be expressed by

$$\eta_{ij}(\boldsymbol{E}_{THz}) = \frac{1}{\epsilon}\delta_{ij} + \sum_{k=1,2,3} r_{ijk} E_k^{THz}. \tag{2.10}$$

For the application of Coulomb field detection by EO crystal, ZnTe (or GaP) is cut on its (110) plane as shown in figure 2.3. Figure 2.3(a) shows the crystal optical axis (x',y',z') and 2.3(b) shows that the Coulomb field induced THz wave normal incidents into the (110) plane of the EO crystal and its polarization has an angle b refer to the new y-axis. The new coordinate system in 2.3(b) is the crystal optical axis coordinate rotated by 45° around the [001] axis. Assuming

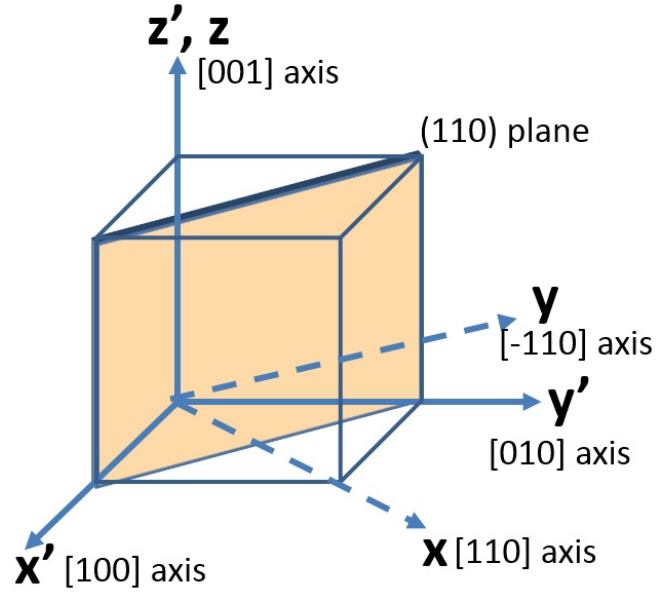

(a) Crystal frame

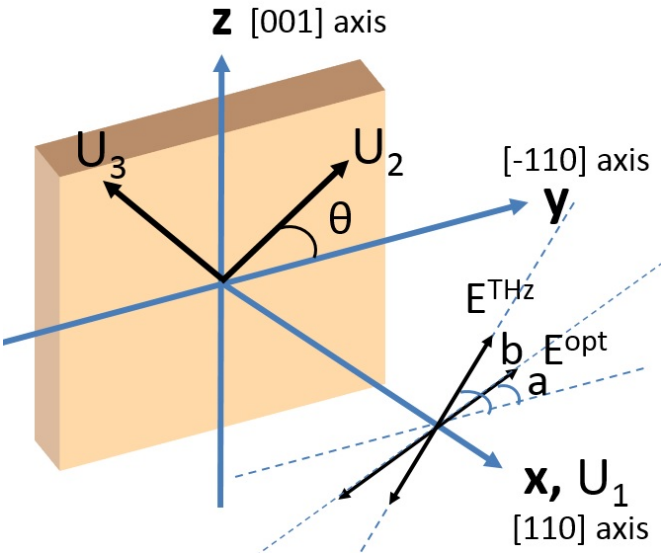

(b) New coordinate frame

FIGURE 2.3: Scheme of coordinate frames: (a) Crystal frame (x',y',z') with crystal optical axis as the frame axis. Frame (x,y,z) shows the new coordinate system which is 45 degree rotation around z' axis from the crystal frame; (b) New coordinate frame for fields normal incident into (110) plane: $[\bar{1}10]$-axis is defined as y-axis and be considered as horizontal. Fields propagate alone -x axis. The angle of laser polarization (E^{opt}) to y-axis is a, and Coulomb field (E^{THz}) to y-axis is b. U_1, U_2 and U_3 show the principal axis in this frame.

the incident electric field $\boldsymbol{E}_{THz}$ travelling alone the -x-axis as shown in 2.3(b), then its electric field in the old crystal coordinate system, which is in the figure 2.3(a) frame, can be expressed by

$$\boldsymbol{E}_{THz} = E_{THz} \begin{pmatrix} -\frac{1}{\sqrt{2}} \cos b \\ \frac{1}{\sqrt{2}} \cos b \\ \sin b \end{pmatrix}. \tag{2.11}$$

Following the equation 2.9, 2.10 and 2.11, the impermeability tensor can be calculated:

$$\boldsymbol{\eta}(\boldsymbol{E}_{THz}) = \frac{1}{n_0^2}\boldsymbol{I} + r_{41}E_{THz} \begin{pmatrix} 0 & \sin b & \frac{1}{\sqrt{2}} \cos b \\ \sin b & 0 & -\frac{1}{\sqrt{2}} \cos b \\ \frac{1}{\sqrt{2}} \cos b & -\frac{1}{\sqrt{2}} \cos b & 0 \end{pmatrix}, \tag{2.12}$$

where $\boldsymbol{I}$ is the identity matrix. In order to simplify the calculation, the principal axes of equation 2.12 need to be found. In the frame of the principal axes, the impermeability tensor takes the form of a diagonalise matrix. To diagonal the above matrix, its eigenvalues have to be calculated:

$$\begin{aligned} \lambda_1 &= \tfrac{1}{n_0^2} + r_{41}E_{THz} \sin b, \\ \lambda_2 &= \tfrac{1}{n_0^2} - \tfrac{r_{41}E_{THz}}{2} \left(\sin b + \sqrt{1 + 3\cos^2 b}\right), \\ \lambda_3 &= \tfrac{1}{n_0^2} - \tfrac{r_{41}E_{THz}}{2} \left(\sin b - \sqrt{1 + 3\cos^2 b}\right). \end{aligned} \tag{2.13}$$

Their corresponded normalized eigenvectors in the crystal frame are:

$$\begin{aligned} U_1' &= \tfrac{1}{\sqrt{2}} \begin{pmatrix} 1 \\ 1 \\ 0 \end{pmatrix} \\ U_2' &= \tfrac{1}{2}\sqrt{1 + \tfrac{\sin b}{\sqrt{1+3\cos^2 b}}} \begin{pmatrix} -1 \\ 1 \\ \frac{2\sqrt{2}\cos b}{\sqrt{1+3\cos^2 b}+\sin b} \end{pmatrix} \\ U_3' &= \tfrac{1}{2}\sqrt{1 - \tfrac{\sin b}{\sqrt{1+3\cos^2 b}}} \begin{pmatrix} 1 \\ -1 \\ \frac{2\sqrt{2}\cos b}{\sqrt{1+3\cos^2 b}-\sin b} \end{pmatrix}. \end{aligned} \tag{2.14}$$

Since the relationship between the eigenvalues and the refractive index is $n_i = \frac{1}{\sqrt{\lambda_i}}$, the refractive index equation can be expended by Taylor series. Therefore

the main refractive index can be obtained:

$$\begin{aligned}
n_1 = n_0 \quad & - \tfrac{1}{2} n_0^3 r_{41} E_{THz} \sin b \\
& + \tfrac{3}{8} n_0^5 \left(r_{41} E_{THz} \sin b\right)^2 \\
& - \tfrac{5}{16} n_0^7 \left(r_{41} E_{THz} \sin b\right)^3 \\
& + \cdots , \\
n_2 = n_0 \quad & + \tfrac{1}{4} n_0^3 r_{41} E_{THz} \left(\sin b + \sqrt{1 + 3\cos^2 b}\right) \\
& + \tfrac{3}{32} n_0^5 \left[r_{41} E_{THz} \left(\sin b + \sqrt{1 + 3\cos^2 b}\right)\right]^2 \\
& + \tfrac{5}{128} n_0^7 \left[r_{41} E_{THz} \left(\sin b + \sqrt{1 + 3\cos^2 b}\right)\right]^3 \\
& + \cdots , \\
n_3 = n_0 \quad & + \tfrac{1}{4} n_0^3 r_{41} E_{THz} \left(\sin b - \sqrt{1 + 3\cos^2 b}\right) \\
& + \tfrac{3}{32} n_0^5 \left[r_{41} E_{THz} \left(\sin b - \sqrt{1 + 3\cos^2 b}\right)\right]^2 \\
& + \tfrac{5}{128} n_0^7 \left[r_{41} E_{THz} \left(\sin b - \sqrt{1 + 3\cos^2 b}\right)\right]^3 \\
& + \cdots .
\end{aligned} \tag{2.15}$$

In normal experimental conditions, the THz wave or Coulomb field is weak and satisfies $n_0^2 r_{41} E_{THz} \ll 1$. Then the $[n_0^2 r_{41} E_{THz}]^2$ and higher order terms can be ignored. For a crystal with a thickness d, a laser with frequency ω incidents the crystal with same orientation as above. The phase retardation along the two principal axis U_2 and U_3 can be calculated [70]:

$$\begin{aligned}
\Gamma(b) &= \frac{\omega d}{c}(n_2 - n_3) \\
&= \frac{1}{2}\frac{\omega d}{c} n_0^3 r_{41} E_{THz} \sqrt{1 + 3\cos^2 b} \\
&\quad + \frac{3}{8}\frac{\omega d}{c} n_0^5 \left(r_{41} E_{THz}\right)^2 \sin b \sqrt{1 + 3\cos^2 b} \\
&\quad + \cdots .
\end{aligned} \tag{2.16}$$

In order to know the principal axis angle θ, as referenced to the $[\bar{1}10]$-axis, a dot product can be applied on these two axis, from which it follows that

$$\cos 2\theta = \frac{\sin b}{\sqrt{1 + 3\cos^2 b}}. \tag{2.17}$$

In the case of the incident THz wave polarization is parallel to the $[\bar{1}10]$-axis, which implies $b = 0$, then the principal axis angle $\theta = \frac{\pi}{4}$. The second term in the phase retardation equation 2.16 will vanish and the next term is considered.

Then the phase retardation becomes:

$$\begin{aligned}\Gamma(b) &= \frac{\omega d}{c} n_0^3 r_{41} E_{THz} + \frac{5}{8}\frac{\omega d}{c} n_0^7 \left(r_{41} E_{THz}\right)^3 + \cdots \\ &= \frac{\omega d n_0}{c} n_0^2 r_{41} E_{THz} \left[1 + \frac{5}{8}\left(n_0^2 r_{41} E_{THz}\right)^2 + \cdots\right].\end{aligned} \tag{2.18}$$

Ignoring the third term of the phase retardation due to its small value, the phase term of an electric field then becomes:

$$\begin{aligned}e^{-i\Gamma(b)} &= e^{-i\frac{\omega d}{c} n_0^3 r_{41} E_{THz}} \cdot e^{-i\frac{5}{8}\frac{\omega d}{c} n_0^7 (r_{41} E_{THz})^3} \\ &\approx \left[1 - i\frac{\omega d}{c} n_0^3 r_{41} E_{THz} - \frac{1}{2}\left(\frac{\omega d}{c}\right)^2 n_0^6 \left(r_{41} E_{THz}\right)^2\right] \cdot \left[1 - i\frac{\omega d}{c}\frac{5}{8} n_0^7 \left(r_{41} E_{THz}\right)^3\right] \\ &= 1 - i\frac{\omega d n_0}{c} n_0^2 r_{41} E_{THz} - \frac{1}{2}\left(\frac{\omega d n_0}{c}\right)^2 \left(n_0^2 r_{41} E_{THz}\right)^2 - i\frac{\omega d n_0}{c}\frac{5}{8}\left(n_0^2 r_{41} E_{THz}\right)^3 \\ &- \left(\frac{\omega d n_0}{c}\right)^2 \frac{5}{8}\left(n_0^2 r_{41} E_{THz}\right)^4 + i\frac{5}{16}\left(\frac{\omega d n_0}{c}\right)^3 \left(n_0^2 r_{41} E_{THz}\right)^5.\end{aligned} \tag{2.19}$$

The first two terms in the above equation 2.19 can also be obtained via an alternative derivation described in subsection 2.3.1. For a THz wave with 1 MV/m field strength, the term $n_0^2 r_{41} E_{THz}$ is in the order of 10^{-5} for ZnTe crystal and 780 nm probe, so that the third term and the following terms in equation 2.19 can be neglected. The third term only needs to be considered if the THz field strength is of the order of 1 GV/m for ZnTe, or 100 MV/m for $LiNbO_3$.

2.3 Analysis in frequency domain

The above standard phase retardation formula 2.16 comes from DC or low frequency applied EO effect. To understand the whole THz pulse effect and consider all frequency components, eg: for EO spectral decoding, it is useful to look at it in frequency domain.

In order to study the electro-optic effect in frequency domain, the time domain optical wave equation, which described the relationship between electric field $\boldsymbol{E}$ and induced polarization $\boldsymbol{P}$, is taken as a starting point from Maxwell's equations we have:

$$\nabla \times \nabla \times \boldsymbol{E} + \frac{1}{c^2}\frac{\partial}{\partial t^2}\boldsymbol{E} = -\frac{1}{\epsilon_0 c^2}\frac{\partial^2 \boldsymbol{P}}{\partial t^2}. \tag{2.20}$$

where the bold font denotes vector quantities. On the left side of equation 2.20, $\nabla \times \nabla \times \boldsymbol{E} = \nabla(\nabla \cdot \boldsymbol{E}) - \nabla^2 \boldsymbol{E}$. The term $\nabla(\nabla \cdot \boldsymbol{E})$ is small if slowly varying envelope approximation (SVEA) is applied. In particular, the electric field $\boldsymbol{E}$ is supposed to be a transverse, infinite plane wave, and then it implies that $\nabla \cdot \boldsymbol{E} = 0$. With basic relationships about polarization and electric field $\boldsymbol{P}(t) = \boldsymbol{P}^{(1)}(t) + \boldsymbol{P}^{NL}(t) = \epsilon_0 \chi^{(1)} \boldsymbol{E}(t) + \boldsymbol{P}^{NL}(t)$, and $\epsilon^{(1)} = 1 + \chi^{(1)}$, the equation 2.20 becomes:

$$\nabla^2 \boldsymbol{E} - \frac{\epsilon^{(1)}}{c^2} \frac{\partial^2}{\partial t^2} \boldsymbol{E} = \mu_0 \frac{\partial^2 \boldsymbol{P}^{NL}}{\partial t^2}. \tag{2.21}$$

The above equation describes a wave in a lossless and dispersionless medium. To include dispersion, each frequency component needs to be considered. Let's consider only the left side of the above equation. The wave time domain expression $\boldsymbol{E}(t, x)$ can be supposed to be a plane wave propagation alone -x-axis and becomes $E(t, x)$, and it can be also expressed by all of its frequency (ω) components:

$$\begin{aligned} E(t, x) &= \int \widetilde{E}(\omega, x)\, e^{-i\omega t} d\omega, \\ \widetilde{E}(\omega, x) &= \widetilde{A}(\omega, 0)\, e^{ikx}, \end{aligned} \tag{2.22}$$

where the tilde symbol stands for the varies in frequency domain, k is wave vector, and $\widetilde{A}(\omega, 0)$ is the initial amplitude of the electric field at position $x = 0$. Then the main part in the second term of equation 2.21 becomes:

$$\begin{aligned} \frac{\partial^2}{\partial t^2} E &= \int \frac{\partial^2}{\partial t^2} \left[\widetilde{A}(\omega, 0)\, e^{i(kx - \omega t)} \right] d\omega \\ &= \int -\omega^2 \widetilde{A}(\omega, 0)\, e^{i(kx - \omega t)} d\omega. \end{aligned} \tag{2.23}$$

Since the plane wave is assumed to be propagating in -x-axis, then the operator ∇^2 can be replaced by $\frac{\partial^2}{\partial x^2}$. Therefore the first term of equation 2.21 becomes:

$$\begin{aligned} \nabla^2 E &= \int \frac{\partial^2}{\partial x^2} \left[\widetilde{A}(\omega, 0)\, e^{i(kx - \omega t)} \right] d\omega \\ &= \int \left[\frac{\partial^2}{\partial x^2} \widetilde{A}(\omega, 0) + 2ik \frac{\partial}{\partial x} \widetilde{A}(\omega, 0) - k^2 \widetilde{A}(\omega, 0) \right] e^{i(kx - \omega t)} d\omega. \end{aligned} \tag{2.24}$$

With a similar definition as equation 2.22, the induced polarization can be expressed by:

$$\begin{aligned} P^{NL}(t,x) &= \int \widetilde{P}^{NL}(\omega,x)\, e^{-i\omega t} d\omega, \\ \widetilde{P}^{NL}(\omega,x) &= \widetilde{P}^{NL}(\omega,0)\, e^{ikx}. \end{aligned} \tag{2.25}$$

Thus, the right side of equation 2.21 is:

$$\frac{\partial^2}{\partial t^2} P^{NL} = \int -\omega^2 \widetilde{P}^{NL}(\omega,x)\, e^{-i\omega t} d\omega. \tag{2.26}$$

Applying the SVEA, $|\frac{\partial^2}{\partial x^2}\widetilde{A}(\omega,0)| \ll |2ik\frac{\partial}{\partial x}\widetilde{A}(\omega,0)|$, equation 2.24 can be simplified by neglecting the term $\frac{\partial^2}{\partial x^2}\widetilde{A}(\omega,0)$. Finally putting equation 2.23, 2.24 and 2.26 into equation 2.21, then the wave equation in the frequency domain can be obtained as:

$$\left[\left(\frac{\omega}{c}\right)^2 \cdot \epsilon - k^2 + 2ik\frac{\partial}{\partial x}\right] \widetilde{A}(\omega,0)\, e^{ikx} = -\omega^2 \mu_0 \widetilde{P}^{NL}(\omega,x). \tag{2.27}$$

Turning to examine the expression for the polarization $\widetilde{P}^{NL}(\omega,x)$, only the second order contribution $\widetilde{P}^{(2)}(\omega,x)$ of the induced polarization is considered here. This nonlinear effect can be described by the relationship of polarization change induced by applied electric fields as:

$$\widetilde{P}_i^{(2)}(\omega_3) = \int_{-\infty}^{+\infty} \epsilon_0 \sum_{jk} \widetilde{\chi}_{ijk}^{(2)}(\omega_3;\omega_1,\omega_2)\, \widetilde{E}_j(\omega_1)\widetilde{E}_k(\omega_3-\omega_1) d\omega_1, \tag{2.28}$$

where $\widetilde{\chi}_{ijk}^{(2)}$ is known as the second-order nonlinear optical susceptibility and it is a third-order tensor. The generated frequency has a restriction that $\omega_3 = \omega_1 + \omega_2$. The i, j, k refer to the wave polarization direction in Cartesian coordinate. The equation 2.28 shows the induced polarization at the i axis by the two broadband incident waves, which includes all frequency combinations.

In order to explain the $\widetilde{\chi}_{ijk}^{(2)}$ related geometry in the crystal under a simply form, only the contribution by two frequency components in equation 2.28 is considered and $\widetilde{p}_i(\omega_3) = \epsilon_0 \sum_{jk} \widetilde{\chi}_{ijk}^{(2)}(\omega_3;\omega_1,\omega_2)\, \widetilde{E}_j(\omega_1)\widetilde{E}_k(\omega_2)$ is defined. For ZnTe or GaP crystal, the $\widetilde{\chi}_{ijk}^{(2)}$, referring to crystal axis as shown in figure 2.3, is:

$$\widetilde{\chi}_{ijk}^{(2)}(\omega) = \begin{cases} \widetilde{\chi}^{(2)}(\omega) & : i \neq j \neq k \\ 0 & : \text{others.} \end{cases} \tag{2.29}$$

In order to transform the $\widetilde{\chi}^{(2)}_{ijk}$ from crystal frame in figure 2.3(a) to lab frame in figure 2.3(b), the tensor is rotated according to:

$$\widetilde{\chi}^{(2)}_{lmn} = \sum_{ijk} R_{li} R_{mj} R_{nk} \widetilde{\chi}^{(2)}_{ijk}, \tag{2.30}$$

where R is the rotation matrix. Then the induced polarization in the new frame is:

$$\widetilde{p}_l = \sum_m \sum_n \widetilde{\chi}^{(2)}_{lmn} \widetilde{E}_m \widetilde{E}_n, \tag{2.31}$$

and it can be rewritten in full expansion:

$$\widetilde{\boldsymbol{p}}(\omega_3) = \epsilon_0 \widetilde{\chi}^{(2)}(\omega_3; \omega_1, \omega_2) \begin{bmatrix} \widetilde{E}^{THz}_z(\omega_1) & 0 & \widetilde{E}^{THz}_x(\omega_1) \\ 0 & -\widetilde{E}^{THz}_z(\omega_1) & -\widetilde{E}^{THz}_y(\omega_1) \\ \widetilde{E}^{THz}_x(\omega_1) & -\widetilde{E}^{THz}_y(\omega_1) & 0 \end{bmatrix} \begin{bmatrix} \widetilde{E}^{opt}_x(\omega_2) \\ \widetilde{E}^{opt}_y(\omega_2) \\ \widetilde{E}^{opt}_z(\omega_2) \end{bmatrix}. \tag{2.32}$$

The subscripts x, y, z show the polarization direction described in fig 2.3(b), and 'opt' stands for laser electric field at ω_2, 'THz' for Coulomb field (which is in teraherz frequency range) at ω_1, in order to show clearly the frequency components respected to our experiments. The angle of laser polarization ($\widetilde{E}^{opt}$) to y-axis is defined as a, and Coulomb field ($\widetilde{E}^{THz}$) to y-axis is b. Therefore, each components has such relationship to its whole field: $\widetilde{E}^{THz}_y = \widetilde{E}^{THz} \cos b$, $\widetilde{E}^{THz}_z = \widetilde{E}^{THz} \sin b$, $\widetilde{E}^{opt}_y = \widetilde{E}^{opt} \cos a$ and $\widetilde{E}^{opt}_z = \widetilde{E}^{opt} \sin a$. The both two input fields are propagation along -x-axis, and then they don't have x polarization components ($\widetilde{E}^{opt}_x = \widetilde{E}^{THz}_x = 0$). With these definitions, the equation 2.32 can be rewritten as:

$$\begin{bmatrix} \widetilde{p}_x \\ \widetilde{p}_y \\ \widetilde{p}_z \end{bmatrix} = \epsilon_0 \widetilde{\chi}^{(2)} \widetilde{E}^{THz} \widetilde{E}^{opt} \begin{bmatrix} \sin b & 0 & 0 \\ 0 & -\sin b & -\cos b \\ 0 & -\cos b & 0 \end{bmatrix} \begin{bmatrix} 0 \\ \cos a \\ \sin a \end{bmatrix}, \tag{2.33}$$

or equivalently:

$$\begin{aligned} \widetilde{p}_x &= 0, \\ \widetilde{p}_y &= -\epsilon_0 \widetilde{\chi}^{(2)} \widetilde{E}^{THz} \widetilde{E}^{opt} \sin(a+b), \\ \widetilde{p}_z &= -\epsilon_0 \widetilde{\chi}^{(2)} \widetilde{E}^{THz} \widetilde{E}^{opt} \cos a \cos b. \end{aligned} \tag{2.34}$$

The above equations imply that the induced polarization $\widetilde{p}$ depends on the polarization angles of the input fields. Some specific cases have been taken for examples: If the input laser and Coulomb field only has y polarization component ($a = 0$ and $b = 0$), then the generated polarization only has z component $\widetilde{p}_z = -\epsilon_0 \widetilde{\chi}^{(2)} \widetilde{E}^{THz} \widetilde{E}^{opt}$; Similarly, if $a = 0$ and $b = \pi/2$, or $b = 0$ and $a = \pi/2$, the

induced polarization has only $\widetilde{p}_y$; If $a = \pi/2$ and $b = \pi/2$, no new polarization generated.

In a general case, the lab frame can be transformed into the principal axis frame in which the generated polarization components are parallel to the input optical wave components. Mathematically, transforming the 3 by 3 matrix in equation 2.33 to its principal axis frame means diagonalising it. The eigenvalues can be calculated as

$$\begin{aligned} \lambda_1 &= \sin b, \\ \lambda_2 &= -\tfrac{1}{2}\left(\sin b + \sqrt{1+3\cos^2 b}\right), \\ \lambda_3 &= -\tfrac{1}{2}\left(\sin b - \sqrt{1+3\cos^2 b}\right), \end{aligned} \tag{2.35}$$

with corresponding normalized eigenvectors are:

$$\begin{aligned} U_1 &= \begin{pmatrix} 1 \\ 0 \\ 0 \end{pmatrix}, \\ U_2 &= \tfrac{\sqrt{2}}{2}\sqrt{1+\tfrac{\sin b}{\sqrt{1+3\cos^2 b}}} \begin{pmatrix} 0 \\ 1 \\ \frac{2\cos b}{\sqrt{1+3\cos^2 b}+\sin b} \end{pmatrix}, \\ U_3 &= \tfrac{\sqrt{2}}{2}\sqrt{1-\tfrac{\sin b}{\sqrt{1+3\cos^2 b}}} \begin{pmatrix} 0 \\ -1 \\ \frac{2\cos b}{\sqrt{1+3\cos^2 b}-\sin b} \end{pmatrix}. \end{aligned} \tag{2.36}$$

The new principal axis vectors U_1, U_2 and U_3 are actually identical with the vectors 2.14 rotated by 45° around z-axis from crystal frame. The principal axis angle θ refer to y-axis can be calculate from the dot production of U_1 and y-axis $[0, 1, 0]$, and has the same form as equation 2.17 that: $\cos 2\theta = \frac{\sin b}{\sqrt{1+3\cos^2 b}}$.

A maximum induced polarization is usually we are expecting in the experiment. It can be obtained in the case that Coulomb field and laser's polarizations are only in y-axis, which means angle $a = 0$ and $b = 0$. Without loss of generality, the induced polarization is discussed in one principal axis and can be expressed by:

$$\widetilde{p}(\omega) = \epsilon_0 \widetilde{\chi}^{(2)}\left(\omega; \Omega_0, \omega - \Omega_0\right) \widetilde{E}^{THz}(\Omega_0) \widetilde{E}^{opt}(\omega - \Omega_0). \tag{2.37}$$

The above equation 2.37 shows the contribution from two frequency components ω and Ω_0. To consider broadband incident waves, equation 2.28 can be modified to be in principal axis. Specific to THz detection case, the ω_1 is defined as a broadband THz frequency wave in Ω range, and ω_3 as a general optical wave in ω range. Therefore, the equation for the broadband waves is a integration over

the whole THz wave spectrum:

$$\begin{aligned}\widetilde{P}(\omega) &= \epsilon_0 \int_{-\infty}^{+\infty} \widetilde{\chi}^{(2)}(\Omega)\widetilde{E}^{THz}(\Omega)\widetilde{E}^{opt}(\omega-\Omega)d\Omega \\ &= \epsilon_0 \left[\widetilde{\chi}^{(2)}(\omega)\widetilde{E}^{THz}(\omega)\right] * \widetilde{E}^{opt}(\omega).\end{aligned} \tag{2.38}$$

To clarify the notations, let $\omega_{opt} = \omega - \Omega$ and $\omega_{sum} = \omega$. Then equation 2.38 can be substituted into the wave equation 2.27, and the generated electric field can be obtained by solving this equation. As shown in reference[66], the solution is

$$\begin{aligned}\widetilde{E}_{sum}(\omega, x) =& \frac{i\omega^2}{2c^2 k^R_{opt}(\omega)} e^{-ik_{opt}(\omega)x} \cdot \\ & \int_{-\infty}^{+\infty} d\Omega \left\{ \widetilde{\chi}^{(2)}\left(\omega; \Omega, \omega-\Omega\right) \left[\frac{e^{i\Delta k(\omega,\Omega)x}-1}{i\Delta k(\omega,\Omega)}\right] \widetilde{E}_{THz}(\Omega,0)\widetilde{E}_{opt}(\omega-\Omega,0) \right\},\end{aligned} \tag{2.39}$$

where the wavevector mismatch $\Delta k = k_{opt}(\omega_{sum} - \omega_{THz}) + k_{THz}(\omega_{THz}) - k_{opt}(\omega_{sum})$, and $\widetilde{E}(\omega, 0) = \widetilde{A}(\omega, 0)$. To include both the sum frequency and difference frequency generation, the $k(-\omega) = -k^*(\omega)$ is also defined. With a definition that the absorption is the imagenary part of the wavevector k^I_{opt}: $k^I_{opt}(\omega) \equiv \beta(\omega)$, and a reasonable restriction that optical refractive index n_{opt} is constant which implies zero group dispersion as shown in equation 2.40:

$$k^R_{opt}(\omega_{opt}) = \frac{\omega_{opt}}{c} n_{opt}, \text{ and } k^R_{opt}(\omega) = \frac{\omega}{c} n_{opt}, \tag{2.40}$$

where k^R_{opt} is the real part of the wavevector.

The total output wave is constituted by sum of the input optical wave and the sum-, difference- frequency field:

$$\widetilde{E}_{total}(\omega, x) = \widetilde{E}_{opt}(\omega, x) - i\omega B e^{i\omega\tau} \left[\widetilde{E}^{eff}_{THz}(\omega, 0) * \widetilde{E}_{opt}(\omega, 0)\right] \tag{2.41}$$

where

$$B = -\frac{x}{c n_{opt}} e^{-i\beta x}, \tag{2.42}$$

$$\tau = n_{opt} x / c, \tag{2.43}$$

$$\widetilde{\xi}\left(\omega; \Omega, \omega-\Omega\right) = \frac{e^{i\Delta k(\omega,\Omega)x}-1}{i\Delta k(\omega,\Omega)x}, \tag{2.44}$$

$$\widetilde{E}^{eff}_{THz}(\omega) = \widetilde{\chi}^{(2)}(\omega) \cdot \widetilde{\xi}(\omega) \cdot \widetilde{E}_{THz}(\omega), \tag{2.45}$$

where the $\widetilde{\xi}(\omega)$ is the phase matching term.

Equation 2.41 can be transformed to time domain:

$$E_{total}(t,x) = E_{opt}(t,x) + B\frac{d}{dt}\left[E_{THz}^{eff}(t-\tau,0)E_{opt}(t-\tau,0)\right], \tag{2.46}$$

$$E_{THz}^{eff}(t,0) = \chi_t^{(2)}(t) * \xi_t(t) * E_{THz}(t,0). \tag{2.47}$$

Equation 2.41 and 2.46 are the general results for the EO effect with $\chi^{(2)}$. These results can be applied in specific cases, such as EO sampling, EO spectrum decoding, and upconversion measurement.

2.3.1 EO sampling

The principle of EO sampling is based on Pockel effect and its scheme can be found in figure 1.4. In this case, the femtosecond laser pulse is used as a probe to scan through the whole picosecond THz wave profile, which requires the laser pulse has a broadband in frequency domain and meanwhile the THz frequency band should be narrow. The convolution term in equation 2.41 can be expanded as:

$$\widetilde{M}(\omega) = \int \widetilde{E}_{opt}(\omega-\Omega)\cdot\widetilde{E}_{THz}^{eff}(\Omega)d\Omega. \tag{2.48}$$

Now the optical electric field is defined as:

$$\widetilde{E}_{opt}(\omega) = |\widetilde{E}_{opt}(\omega)|\cdot e^{i\phi(\omega)}. \tag{2.49}$$

In the EO sampling case, the optical frequency and THz frequency have a relation of $\omega \gg \Omega$, and the bandwidth of optical laser and the bandwidth of THz have a relation of $\Delta\omega \gg \Delta\Omega$. Therefore a reasonable approximation can be made:

$$|\widetilde{E}_{opt}(\omega-\Omega)| \approx |\widetilde{E}_{opt}(\omega)|. \tag{2.50}$$

In addition, the optical laser pulse is assumed near transform-limited, which implies its spectral phase is frequency independent of THz frequency offsets. Thus,

$$e^{i\phi(\omega-\Omega)} \equiv e^{i\phi(\omega)}. \tag{2.51}$$

Putting the definition equation 2.49, the approximation equation 2.50 and equation 2.51 into the convolution term of equation 2.41, the $\widetilde{E}_{opt}(\omega-\Omega) \approx \widetilde{E}_{opt}(\omega)$ term is not related to Ω anymore and can be moved out of the integration, therefore only the $\widetilde{E}_{THz}^{eff}(\Omega)$ term left. Please note here, a term $e^{i\Omega t}$ is induced here as

the time delay between the optical wave and the THz wave by scanning. Then the integration can be seen as an inverse Fourier transform:

$$\int \widetilde{E}_{THz}^{eff}(\Omega) \cdot e^{i\Omega t} d\Omega = E_{THz}^{eff}(t). \tag{2.52}$$

A phase delay term $e^{i\omega\tau}$ outside the convolution in equation 2.41 shows the gained phase by propagation from 0 to distance x for the input optical wave. Therefore, applying $\widetilde{E}_{opt}(\omega, x) = \widetilde{E}_{opt}(\omega, 0)e^{i\omega\tau}$, we can get:

$$\widetilde{E}_{total}(\omega, x) = \widetilde{E}_{opt}(\omega, x) \left[1 - i\omega B \cdot E_{THz}^{eff}(x, t)\right]. \tag{2.53}$$

With a low THz field strength restriction:

$$\omega B E_{THz}^{eff}(t) \ll 1, \tag{2.54}$$

and applying a reverse Taylor series expansion and ignoring the higher orders that $1 + x \approx e^x$, equation 2.53 can be rewritten to:

$$\widetilde{E}_{total}(\omega) = \widetilde{E}_{opt}(\omega) \cdot e^{-i\omega B \cdot E_{THz}^{eff}(t)}. \tag{2.55}$$

From the above equation, the phase retardation $\Phi = \omega B \cdot E_{THz}^{eff}(t)$. To expend it in details, apply equation 2.42 and also the relationship $\chi^{(2)} = -r_{41}n^4$ [63] into the phase retardation, then we can get:

$$\Phi = \frac{\omega x}{c} n_{opt}^3 r_{41} E_{THz}^{eff}(t) \cdot e^{-k_{opt}^I x}. \tag{2.56}$$

If a lossless media is assumed here, then there is no absorption which leads to $e^{-k_{opt}^I x} = 1$. Then this result is consistent with the maximum phase retardation from the refractive index approach in equation 2.16.

2.3.2 EO Spectral Decoding

EOSD encodes the THz profile into a linear chirped optical pulse and its scheme can be found in figure 1.5. The laser pulse is still broadband compared to the THz wave, but the optical spectral phase depends on frequency which implies $e^{i\phi(\omega-\Omega)} \neq e^{i\phi(\omega)}$ due to the linear chirp. With a Taylor expansion on the phase term of equation 2.49, the phase of an optical electric field can be expressed at

ω_0 by

$$\phi(\omega) = \phi(\omega_0)+\phi^{'}(\omega_0)(\omega-\omega_0)+\frac{1}{2}\phi^{''}(\omega_0)(\omega-\omega_0)^2+\frac{1}{6}\phi^{'''}(\omega_0)(\omega-\omega_0)^3+\cdots, \quad (2.57)$$

where $\phi^{'}(\omega_0) = \frac{d\phi}{d\omega}|_{\omega=\omega_0}$, $\phi^{''}(\omega_0) = \frac{d^2\phi}{d\omega^2}|_{\omega=\omega_0}$, and $\phi^{'''}(\omega_0) = \frac{d^3\phi}{d\omega^3}|_{\omega=\omega_0}$ are defined here. For an ideal linear chirp, the phase only has the first three terms, therefore:

$$\phi(\omega) = \phi(\omega_0) + \phi^{'}(\omega_0)(\omega - \omega_0) + \frac{1}{2}\phi^{''}(\omega_0)(\omega - \omega_0)^2. \quad (2.58)$$

Focusing on the convolution term in equation 2.41, and substituting equation 2.58, it can be seen that

$$\begin{aligned}\widetilde{M}(\omega) &= \int \widetilde{E}_{opt}(\omega - \Omega) \cdot \widetilde{E}^{eff}_{THz}(\Omega)d\Omega \\ &= \int |\widetilde{E}_{opt}(\omega)|e^{-i\phi(\omega-\Omega)}\widetilde{E}^{eff}_{THz}(\Omega)d\Omega.\end{aligned} \quad (2.59)$$

The phase can be expressed by

$$\phi(\omega - \Omega) = \phi(\omega) - \phi^{'}(\omega_0)\Omega - \phi^{''}(\omega_0)(\omega - \omega_0)\Omega + \frac{1}{2}\phi^{''}(\omega_0)\Omega^2. \quad (2.60)$$

An approximation is made for the amplitude of the broadband laser pulse,

$$|\widetilde{E}_{opt}(\omega - \Omega)| \approx |\widetilde{E}_{opt}(\omega)|. \quad (2.61)$$

Putting equation 2.60 and 2.61 into 2.59, the core convolution term can be rewritten as:

$$\widetilde{M}(\omega) = |\widetilde{E}_{opt}(\omega)|e^{-i\phi(\omega)}\cdot\int e^{i\left[\phi^{'}(\omega_0)+\phi^{''}(\omega_0)(\omega-\omega_0)\right]\Omega}\cdot e^{-i\frac{\phi^{''}(\omega_0)}{2}\Omega^2}\cdot\widetilde{E}^{eff}_{THz}(\Omega)d\Omega, \quad (2.62)$$

with the definition

$$\tau \equiv \phi^{''}(\omega_0)(\omega - \omega_0). \quad (2.63)$$

Equation 2.62 can be rewritten as [71]

$$\begin{aligned}\widetilde{M}(\omega) &= \widetilde{E}_{opt}(\omega)\cdot\int e^{-i\frac{\phi^{''}(\omega_0)}{2}\Omega^2}\cdot\widetilde{E}^{eff}_{THz}(\Omega)\cdot e^{it_0\Omega}\cdot e^{i\tau\Omega}d\Omega \\ &= \widetilde{E}_{opt}(\omega)\cdot\left\{E^{eff}_{THz}(\tau + t_0) * \left[\sqrt{\frac{\pi}{\beta}}\cdot e^{\left(\frac{i\tau^2}{4\beta}-\frac{i\pi}{4}\right)}\right]\right\},\end{aligned} \quad (2.64)$$

where $\beta \equiv \frac{\phi''(\omega_0)}{2}$, $\tau = 2\beta(\omega - \omega_0)$, and the inverse Fourier transform

$$\mathrm{FT}^{-1}\left[e^{-i\beta\Omega^2}\right] = \frac{1}{2\pi}\sqrt{\frac{\pi}{\beta}} \cdot e^{\left(\frac{i\tau^2}{4\beta} - \frac{i\pi}{4}\right)}. \tag{2.65}$$

Therefore, to sum up the above equations, the equation 2.59 can be finally expressed by

$$\begin{aligned} \widetilde{M}(\omega) &= \int \widetilde{E}_{opt}(\omega - \Omega) \cdot \widetilde{E}^{eff}_{THz}(\Omega) d\Omega \\ &= \sqrt{\frac{\pi}{\beta}} \cdot \widetilde{E}_{opt}(\omega) \cdot \left[E^{eff}_{THz}(\tau + t_0) * e^{\left(\frac{i\tau^2}{4\beta} - \frac{i\pi}{4}\right)}\right] \\ &= \sqrt{\frac{\pi}{\beta}} \cdot \widetilde{E}_{opt}(\omega) \cdot E^{b}_{THz}(\tau + t_0), \end{aligned} \tag{2.66}$$

where $E^{b}_{THz}(\tau) = E^{eff}_{THz}(\tau) * e^{\left(\frac{i\tau^2}{4\beta} - \frac{i\pi}{4}\right)}$. The convolution term shows the resolution limitation for EOSD, which is described in details in the subsection 2.4.4.

2.3.3 Spectral upconversion

In a spectral upconversion measurement, a monochromatic optical laser is used as probe. Its scheme can be found in figure 1.8. This technique requires a narrow bandwidth laser probe. Then the THz profile can be frequency up converted as the side bands of the central laser frequency without overlapping.

A monochromatic wave can be defined as

$$\widetilde{E}_{opt}(\omega) = A \cdot \delta(\omega - \omega_0), \tag{2.67}$$

where A is the amplitude of the optical wave. Following the same approach on the previous subsection, a different optical electric field definition 2.67 is put into equation 2.59:

$$\begin{aligned} \widetilde{M}(\omega) &= \int \widetilde{E}_{opt}(\omega - \Omega) \cdot \widetilde{E}^{eff}_{THz}(\Omega) d\Omega \\ &= A \cdot \int \delta(\omega - \omega_0 - \Omega) \cdot \widetilde{E}^{eff}_{THz}(\Omega) d\Omega \\ &= A \cdot \delta(\omega - \omega_0) * \widetilde{E}^{eff}_{THz}(\omega) \\ &= A \cdot \widetilde{E}^{eff}_{THz}(\omega - \omega_0). \end{aligned} \tag{2.68}$$

From the above equation, the result of the convolution term is a replica of THz spectral profile but centered at optical laser frequency ω_0.

2.4 Electro-optic detection

2.4.1 Jones matrices

The core component of a EOSD system is a two-crossed-polarizer setup. It contains a polarizer, EO crystal, a quarter-wave plate ($\lambda/4$ wave plate), a half-wave plate ($\lambda/2$ wave plate) and another polarizer which is crossed with respect to the previous one. A scheme of this setup is shown in figure 2.4. In the figure, optical beam and THz beam propagate in the blue arrow direction. Polarizations of optical beam and THz beam to horizontal plane have angles of a and b respectively. The principal axis of EO crystal has an angle of θ. Quarter wave plate ($\lambda/4$) has an angle α and half wave plate ($\lambda/2$) has an angle of φ.

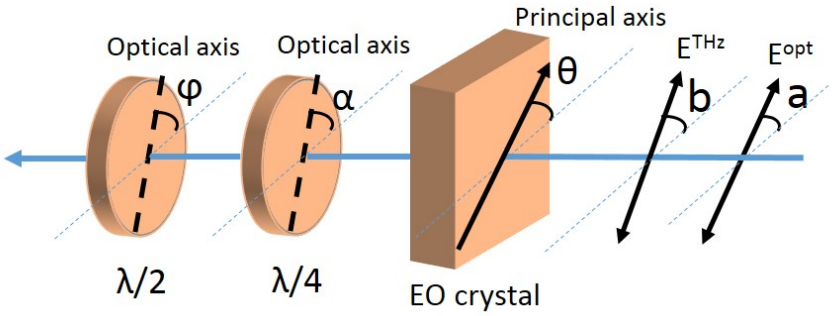

FIGURE 2.4: EO detection scheme: the blue arrow through all optical components shows the optical beam and THz beam propagation direction. Polarizations of optical beam and THz beam to horizontal plane have angles of a and b respectively. The principal axis of EO crystal has an angle of θ. The quarter wave plate ($\lambda/4$) has an angle α and half wave plate ($\lambda/2$) has an angle of φ.

The EO crystal induces a frequency mixing between the Coulomb field and laser pulse due to its non-linear coefficient. A combination of $\lambda/4$ wave plate and $\lambda/2$ wave plate can compensate the residual birefringence in the EO crystal and adjust the background in the output signal. The residual birefringence comes from the holder pressure applied on the crystal, or through strain introduced in crystal growth. Using a Jones matrix formalism, the output electric field polarization

can be described by the following matrix:

$$\begin{bmatrix} \widetilde{E}^{y}_{out}(\omega) \\ \widetilde{E}^{z}_{out}(\omega) \end{bmatrix} = R(\varphi) M_{\mathrm{H}} R(-\varphi) R(\alpha) M_{\mathrm{Q}} R(-\alpha) R(\theta) M_{\mathrm{EO}} R(-\theta) \begin{bmatrix} \cos(a) \\ \sin(a) \end{bmatrix} \widetilde{E}_{opt}(\omega), \tag{2.69}$$

where the $R(\theta)$ is rotation matrix:

$$R(\theta) = \begin{bmatrix} \cos\theta & -\sin\theta \\ \sin\theta & \cos\theta \end{bmatrix}, \tag{2.70}$$

$$R(-\theta) = \begin{bmatrix} \cos\theta & \sin\theta \\ -\sin\theta & \cos\theta \end{bmatrix}. \tag{2.71}$$

M_{H} and M_{Q} are Jones matrices for half-wave plate and quarter-wave plate respectively:

$$M_{QW} = \begin{bmatrix} e^{i\frac{\pi}{4}} & 0 \\ 0 & e^{-i\frac{\pi}{4}} \end{bmatrix}, \tag{2.72}$$

$$M_{HW} = \begin{bmatrix} e^{i\frac{\pi}{2}} & 0 \\ 0 & e^{-i\frac{\pi}{2}} \end{bmatrix}. \tag{2.73}$$

The frequency mixing in the EO crystal is described in M_{EO} matrix as [66]:

$$M_{\mathrm{EO}} = \begin{bmatrix} \left(1 + \frac{i\omega x}{nc} \cdot \lambda_2 \cdot \widetilde{E}^{eff}_{\mathrm{Thz}} *\right) & 0 \\ 0 & \left(1 + \frac{i\omega x}{nc} \cdot \lambda_3 \cdot \widetilde{E}^{eff}_{\mathrm{THz}} *\right) \end{bmatrix}, \tag{2.74}$$

where λ_2, λ_3 are eigenvalues from equation 2.35 and include the THz polarization angle. $\widetilde{E}^{eff}_{\mathrm{THz}}(\Omega)$ is defined as the effective THz wave (Coulomb field). It includes the nonlinear coefficient of the EO crystal and the phase matching term which can be seen in equation 2.45. Usually the polarization of the optical beam is parallel to horizontal plane, in which case the angle $a = 0$. The THz wave polarization is also usually set in horizontal $b = 0$, then $\lambda_2 = 1$, $\lambda_3 = -1$ and the angle of crystal principal axis $\theta = \pi/4$. For a crossed polarization detection, there is a polarizer after the last half wave plate to only let the vertically polarized optical beam pass. Therefore the output signal only has $\widetilde{E}^{z}_{out}(\omega)$ components. To simplify the expression, let $\widetilde{E}_{out}(\omega) = \widetilde{E}^{z}_{out}(\omega)$. Through a calculation on equation 2.69, we

can obtain:

$$\begin{aligned}\widetilde{E}_{out}(\omega) = &-\frac{\sqrt{2}}{2}\left[\widetilde{E}_{opt}(\omega)\sin 2(\alpha-\varphi)+\sin 2(\theta-\varphi)\frac{x\omega}{cn}\widetilde{E}^{eff}_{THz}(\omega)*\widetilde{E}_{opt}(\omega)\right]\\ &-\frac{\sqrt{2}}{2}i\left[\widetilde{E}_{opt}(\omega)\sin 2\varphi+\sin 2(\alpha-\theta-\varphi)\frac{x\omega}{cn}\widetilde{E}^{eff}_{THz}(\omega)*\widetilde{E}_{opt}(\omega)\right].\end{aligned} \tag{2.75}$$

The above equation shows the output electric field, where the φ is the angle of half-wave plate, α is quarter-wave plate angle, and θ is EO crystal angle. However the measured signal is the intensity of this field. Therefore $I = \frac{1}{2}\epsilon_0 c\widetilde{E}_{out}(\omega)\cdot \widetilde{E}^{*}_{out}(\omega)$ should be calculated. A general result is shown in equation 2.76:

$$\begin{aligned}I =& I_1+I_2+I_3,\\ I_1 =& \frac{\epsilon_0 c}{4}\left|\widetilde{E}_{opt}(\omega)\right|^2\cdot\left[\sin^2 2(\alpha-\varphi)+\sin^2(2\varphi)\right],\\ I_2 =& \frac{\epsilon_0 c}{4}\left\{\widetilde{E}_{opt}(\omega)\cdot\left[\widetilde{E}^{eff}_{THz}(\omega)*\widetilde{E}_{opt}(\omega)\right]^{*}+\widetilde{E}^{*}_{opt}(\omega)\cdot\left[\widetilde{E}^{eff}_{THz}(\omega)*\widetilde{E}_{opt}(\omega)\right]\right\}\\ &\cdot\frac{x\omega}{cn}\left[\sin 2(\alpha-\varphi)\sin 2(\theta-\varphi)+\sin 2\varphi\sin 2(\alpha-\theta-\varphi)\right],\\ I_3 =& \frac{\epsilon_0 c}{4}\left|\widetilde{E}^{eff}_{THz}(\omega)*\widetilde{E}_{opt}(\omega)\right|^2\left(\frac{x\omega}{cn}\right)^2\left[\sin^2 2(\alpha-\theta-\varphi)+\sin^2 2(\theta-\varphi)\right].\end{aligned} \tag{2.76}$$

For a EOSD scheme, the convolution term in I_2 can be transformed as in the equation 2.66, since the $\widetilde{E}^{opt}(\omega-\Omega)$ can be written as a Taylor expansion about ω. Then the second term can be rewritten to:

$$\begin{aligned}I_2 =& \frac{\epsilon_0 c}{2}\left|\widetilde{E}_{opt}(\omega)\right|^2\frac{x\omega}{cn}\sqrt{\frac{\pi}{\beta}}\left[E^{eff}_{THZ}(\tau+t_0)*\cos\left(\frac{\tau^2}{4\beta}-\frac{\pi}{4}\right)\right]\\ &\times\left[\sin 2(\alpha-\varphi)\sin 2(\theta-\varphi)+\sin 2\varphi\sin 2(\alpha-\theta-\varphi)\right].\end{aligned} \tag{2.77}$$

With the same transform, the third term I_3 can be rewritten to:

$$\begin{aligned}I_3 =& \frac{\epsilon_0 c}{2}\left|\widetilde{E}_{opt}(\omega)\right|^2\left(\frac{x\omega}{cn}\right)^2\frac{\pi}{2\beta}\left|E^{eff}_{THz}(\tau+t_0)*e^{\left(\frac{i\tau^2}{4\beta}-\frac{i\pi}{4}\right)}\right|^2\\ &\times\left[\sin^2 2(\alpha-\theta-\varphi)+\sin^2 2(\theta-\varphi)\right],\end{aligned} \tag{2.78}$$

or in the form of:

$$I_3 = \frac{\epsilon_0 c}{2}\left|\widetilde{E}_{opt}(\omega)\right|^2 \left\{\left|E^{eff}_{THz}(\tau) * \cos\left(\frac{\tau^2}{4\beta} - \frac{\pi}{4}\right)\right|^2 + \left|E^{eff}_{THz}(\tau) * \sin\left(\frac{\tau^2}{4\beta} - \frac{\pi}{4}\right)\right|^2\right\} \cdot \left(\frac{x\omega}{cn}\right)^2 \frac{\pi}{2\beta}\left[\sin^2 2(\alpha - \theta - \varphi) + \sin^2 2(\theta - \varphi)\right]. \tag{2.79}$$

The equation 2.76 is a general result for the EO detection settings. The first term I_1 of this result is the leaked laser background, which only depends on the intensity of probe laser pulse. The second term I_2 is related to laser intensity and THz wave electric field. And the third term I_3 is related to laser intensity and THz wave intensity. Since all the three terms are related to laser probe intensity, the result signal can be normalized by laser intensity easily.

2.4.2 Crossed polarization detection

For setting of an ideal crossed polarization detection, a scheme of which is shown in figure 1.5, the angles of the half-wave plate and the quarter-wave plate are equal to zero ($\alpha = 0, \varphi = 0$). Therefore, the matrix 2.69 can be simplified, and the optical polarization angle a is remained in the matrix. As an ideal crossed polarization, a second polarizer is induced in the matrix after the EO crystal matrix, which is always set to perpendicular to the input optical polarization. It is shown in equation 2.80:

$$\widetilde{E}_{\text{out}}(\omega) = \begin{bmatrix} -\sin a & \cos a \end{bmatrix} R(\theta) M_{\text{EO}} R(-\theta) \begin{bmatrix} \cos a \\ \sin a \end{bmatrix} \widetilde{E}^{opt}(\omega). \tag{2.80}$$

The result, including the optical polarization angle and THz polarization angle, is

$$\widetilde{E}_{\text{out}}(\omega) = \frac{i\omega x}{nc}\frac{\sqrt{1+3\cos^2 b}}{2} \cdot \sin[2(\theta - a)] \cdot \widetilde{E}^{eff}_{THz}(\omega) * \widetilde{E}_{opt}(\omega). \tag{2.81}$$

Therefore, the intensity can be calculated in a expression of

$$I_{CP} = \frac{\epsilon_0 c}{2}\left(\frac{x\omega}{cn}\right)^2 \left|\widetilde{E}^{eff}_{THz}(\omega) * \widetilde{E}_{opt}(\omega)\right|^2 \cdot \frac{(1+3\cos^2 b)}{4}\sin^2[2(\theta - a)]. \tag{2.82}$$

This result includes the polarization angles of input optical beam a and THz beam b. In the case that Coulomb field and laser polarization are only in the

horizontal plane ($a = b = 0$), the EO crystal principal axis angle θ is $\frac{\pi}{4}$ as usual. The crossed polarization detection can be expressed by

$$\begin{aligned} I_{CP} &= \frac{\epsilon_0 c}{2}\left(\frac{x\omega}{cn}\right)^2 \left|\widetilde{E}_{THz}^{eff}(\omega) * \widetilde{E}_{opt}(\omega)\right|^2 \\ &= I_{laser} \cdot \left(\frac{x\omega}{cn}\right)^2 \frac{\pi}{\beta}\left|E_{THz}^{eff}(\tau + t_0) * e^{\left(\frac{i\tau^2}{4\beta} - \frac{i\pi}{4}\right)}\right|^2, \end{aligned} \tag{2.83}$$

where $I_{laser} = \frac{1}{2}\epsilon_0 c\left|\widetilde{E}_{opt}(\omega)\right|^2$. The result shows it is proportional to THz wave intensity in the crossed polarization setting.

This result can be also obtained from equation 2.76 under the setting that $\alpha = 0$, $\varphi = 0$, and $\theta = \frac{\pi}{4}$. In this case, the I_1 and I_2 terms vanish, and only the I_3 term remains.

2.4.3 Balanced detection

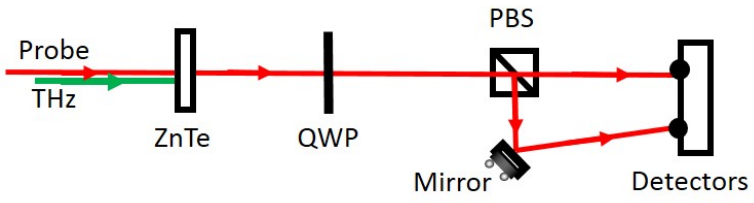

FIGURE 2.5: Balance detection scheme. QWP: Quarter Wave Plate, PBS: Polarizing Beam Splitter

In the balanced detection arrangement, which is shown schematically in figure 2.5, the laser pulse encodes the Coulomb field (THz wave) in the same way as previously described. However, after the ZnTe crystal the probe goes through a quarter-wave plate and a polarising beam splitter, and finally the two orthogonally polarized beams are captured by two photodiodes. The final signal is the difference in intensities measured by the two photodiodes. The balance detection signal can be calculate through the matrix 2.69 by setting half wave plate angle $\varphi = 0$ and quarter wave plate angle $\alpha = \frac{\pi}{4}$. The measured signal intensity is:

$$I_{BD} = |\widetilde{E}_{\text{out}}^{y}(\omega)|^2 - |\widetilde{E}_{\text{out}}^{z}(\omega)|^2. \tag{2.84}$$

The intensities on each photodiode includes all three terms described by equation 2.76. For the difference signal of the balance detection scheme, we obtain

$$I_{BD} = I_{laser}\frac{x\omega}{cn}\sqrt{\frac{\pi}{\beta}}\left[E_{THZ}^{eff}\left(\tau + t_0\right) * \cos\left(\frac{\tau^2}{4\beta} - \frac{\pi}{4}\right)\right] \cdot \sin[2(a-\theta)] \cdot \sqrt{1+3\cos^2 b}. \tag{2.85}$$

If the input Coulomb field and the probe laser pulse have only a horizontal polarization component, which means $a = b = 0$ and $\theta = \frac{\pi}{4}$, then the result 2.85 has the same form but double the value as the second term in equation 2.76: $I_{BD} = 2I_2$. The result shows it is proportional to THz wave electric field in the balance detection setting.

2.4.4 Detection limitations

For an EOSD measurement, a bunch temporal profile is encoded in a laser pulse spectrum. The relationship between time scaling and frequency scaling depends on the chirp parameter of the laser pulse. Since the chirp is fixed when performing measurements, the time-frequency mapping relationship is fixed too. However, for a short bunch, a fast modulation is applied in the EO crystal, and it distorts the mapping relationship and leads to a broadening and interference in the signal.

A calculation for the broadening of measured bunch lengths (blue and green) and the original bunch lengths (red) is shown in figure 2.6. This calculation is based on equation 2.77 and 2.78, referring to the parameters of CALIFES EO bunch profile monitor, with 130 fs transform limited laser pulse chirped to 13.8 ps. The Coulomb field is assumed to be a Gaussian shape with bunch length from 0.7 ps to 10.5 ps. The bunch length broadening starts from 5 ps bunch length. The shorter the bunch length, the larger the broadening appears. This limitation determines the shortest bunch that this EOSD system can measure, which is different from system resolution.

It is possible to explain the broadening through equations 2.83 and 2.85. From the EOSD crossed polarization measurement, the actual measured signal is not the Coulomb field itself but a convolution of it and a term of $e^{\left(\frac{i\tau^2}{4\beta} - \frac{i\pi}{4}\right)}$. Meanwhile, for a EOSD balance detection, the measured signal is a convolution between the Coulomb field and a term $\cos\left(\frac{\tau^2}{4\beta} - \frac{\pi}{4}\right)$. These two convolution terms leads to a broadening on the measured signal for short bunches. Their behaviour is shown in figure 2.7.

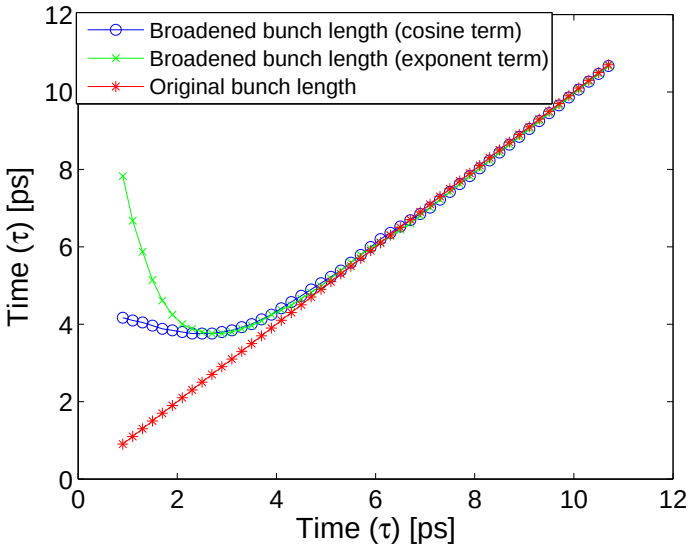

FIGURE 2.6: Calculation for bunch length broadening from EOSD: x-axis is original bunch length from 0.7 ps to 10.5 ps and y-axis is the calculated bunch length from EOSD. Red star line shows no broadening, blue circle line shows the broadening from the cosine term and green cross line shows the broadening from the exponent term

In figure 2.7(a), the original 6 ps Gaussian bunch profile and the cosine and sine terms are shown. Since $\tau = 2\beta(\omega - \omega_0)$, these two oscillating terms are only related to the chirp parameter β, which is related to original laser duration and chirped duration [45] according to $\beta = \frac{1}{2}\sqrt{\sigma_0^2\sigma_c^2 - \sigma_0^4} \approx T_0 T_c/[8\ln(2)]$, where T_0 and T_c refer to the laser transform limited and chirped FWHM durations respectively. Once the chirp is determined, the sine and cosine terms are fixed.

The effect of the convolution can be summarised by referring to a width of the convolution cosine and sine functions. The length of the cosine term can be defined by the length of the middle peak, which is the width when the cosine term equals to zero: $w = \sqrt{12\pi\beta} \approx 2.6\sqrt{T_0 T_c}$. For a 130 fs laser pulse chirped to 13.8 ps, the width $w = 3.5$ ps. For a 6 ps long bunch, the convolution result is mainly determined on the shape of the bunch as shown in figure 2.7(b). The cross polarization detection and balance detection have a similar result. Reducing the bunch length to 3 ps, less than the width of cosine term but larger than the sine term $w_2 = \sqrt{4\pi\beta} = 2.0$ ps, the measured signal starts to broaden slowly. An example calculation is shown in figure 2.7(c). For a 1 ps bunch length, which is smaller than the width of the sine and cosine terms, the signal is broadened significantly, as shown in figure 2.7(d). In this case, the measured signal from cross polarization detection only shows the broaden signal, but signal from balance detection records an additional oscillation arising from interference in EO-generation and input optical pulses.

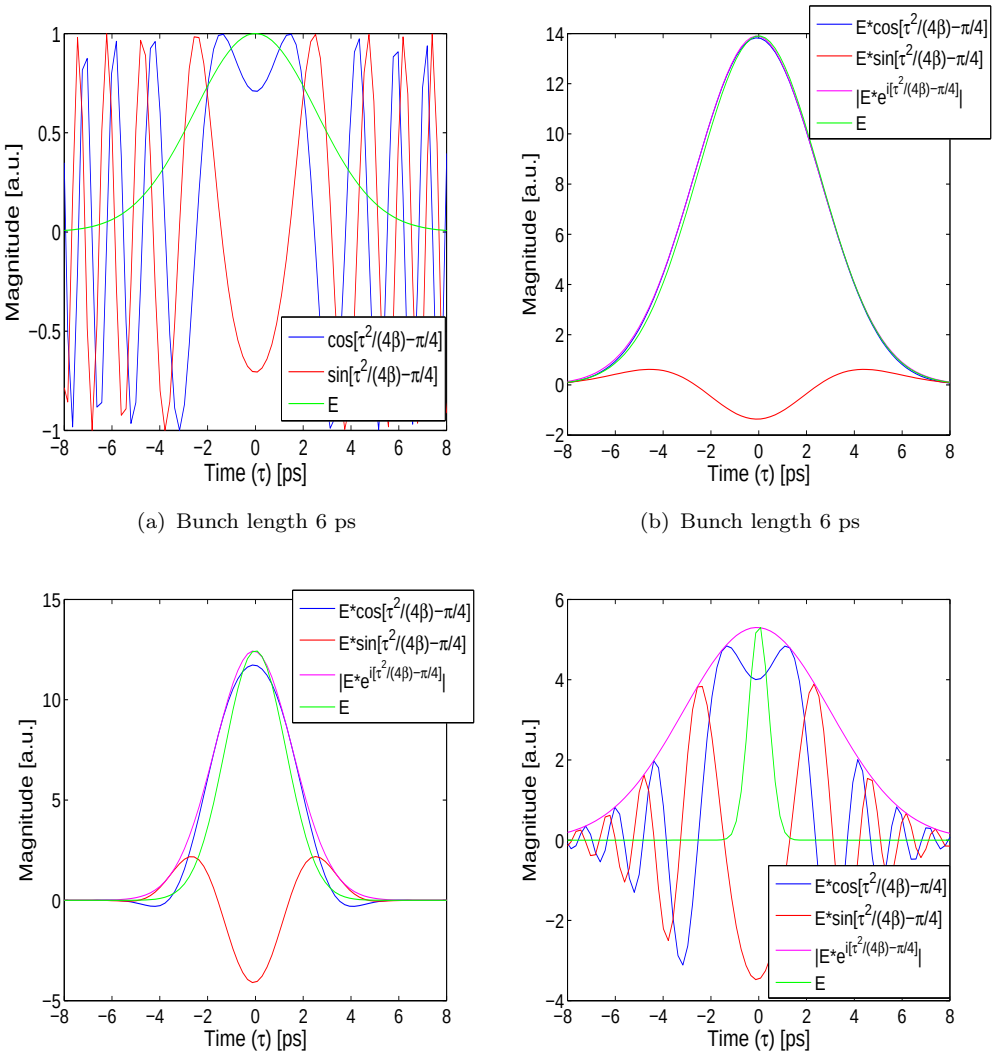

(a) Bunch length 6 ps

(b) Bunch length 6 ps

(c) Bunch length 3 ps

(d) Bunch length 1 ps

FIGURE 2.7: The role of the convolution terms: Green line shows the bunch Coulomb field profile in a function of time τ. (a) shows the bunch profile, the sine term and cosine term for a 6 ps bunch duration. (b)(c)(d) show the convolution results on each terms comparing to the original bunch profile for 6 ps, 3 ps and 1 ps respectively.

2.5 Detection signal dependence on crystal orientation

For an EO measurement a high signal to noise ratio is highly desirable. To achieve a high signal magnitude, which is related to the orientation of crystal, polarization of input Coulomb field (THz wave) and laser wave, is required. In this section, the relationship between EOSD signal intensity, orientations of crystal and input

waves is discussed. An example is given on the optimization method for the implementation of a rotated [110]-axis crystal.

2.5.1 Definition and theory

An often used (110)-plane cut ZnTe crystal is assumed here. The [110]-axis is set to horizontal as y-axis (lab frame). Coulomb field polarization angle is defined as b, corresponding to a rotation from the y-axis, and laser polarization angle to y-axis is defined as a, as shown in figure 2.3(b).

The detection signal can be calculated by equation 2.82 and 2.85, depending on the setup scheme of the measurement. In order to study quantitatively, some apecific parameters are assumed here: $\omega_0 = 2.35 \times 10^{15}$ rad $\cdot$ s^{-1} (i.e. $\lambda = 800$ nm), $d = 4$ mm is the thickness of crystal, $n_0 = 3.22$ is the refractive index of laser pulse in the crystal and $r_{41} = 4.04 \times 10^{-12}$ m/V. Based on equation 2.17, the angle of principal axis to y-axis θ can be written as:

$$\theta\,(b) = \frac{1}{2}\arccos\left(\frac{\sin b}{\sqrt{1+3\cos^2 b}}\right). \tag{2.86}$$

With the above physical parameter choices the detection signal intensity with Coulomb field angle b, probe beam angle a and crystal angle θ can be calculated.

2.5.2 Crystal installation

A 4 mm ZnTe crystal with its [$\bar{1}$10]-axis not paralleling to one edge is tested here by balanced detection setup. In the crystal testing, the polarization of laser on the table was parallel to the table plane (horizontal), and THz (terahertz) polarization is perpendicular to the table (vertical). The THz peak signals are recorded with rotating ZnTe angle by 5° (from 0° to 150°) or 10° (from 150° to 360°) step. A random starting angle is considered as 0° crystal angle. The signals on two photo diodes are re-balanced between each measurement using quarter wave plate after ZnTe. Laser power is re-balanced on photo diodes using reflective ND filter wheel (continuous). The crystals were tested by detecting the THz wave generated from a photo conductive antenna. The measured THz wave peak value and calculated value are shown in figure 2.8 and the signals are normalized. The measured blue plot almost overlapped with the calculated red plot. The small difference may be induced by the resident birefringence in the

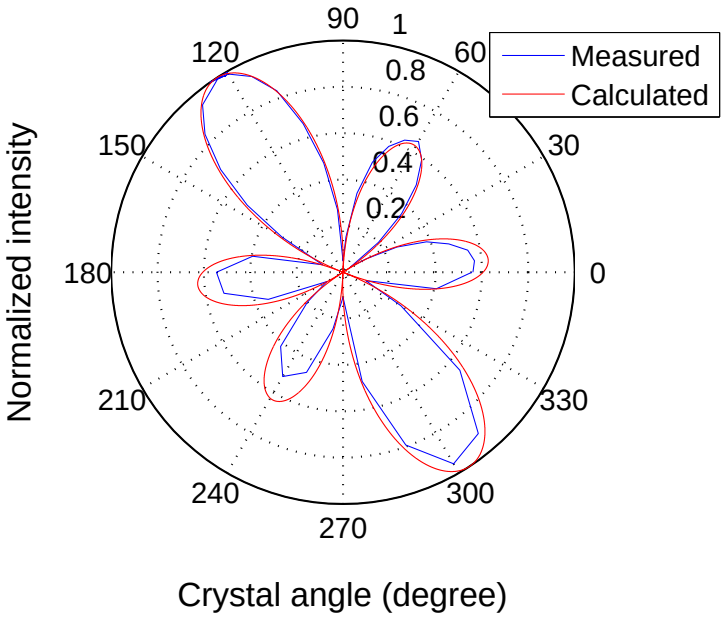

FIGURE 2.8: Crystal angle dependence of THz signal detection: Blue line shows the normalized measured THz signal depends on crystal angle by EO sampling in a balance detection setup. Red line shows the calculation result. The ZnTe crystal in the measurement has a thickness of 4 mm.

crystal. Based on this result, the axis perpendicular to the maximum peak value axis is the $[\bar{1}10]$-axis, and its $[\bar{1}10]$-axis is 21.34° to one edge.

For the simplest alignment, usually a crystal with horizontal $[\bar{1}10]$-axis is selected to be installed in the accelerator. The laser polarization is set to horizontal as well. With an electron beam passing the crystal at the center of the pipe (and with the crystal at the vertical mid-line as well) a horizontal polarization Coulomb field is present at the crystal. Based on the above settings, a maximum EOSD signal will be measured.

For our crystal the [110]-axis is rotated by 21° to the crystal edge. Physically the crystal is mounted with edges in horizontal or vertical in the accelerator and the principal axes of the crystal are rotated with respect to the Coulomb field. With the titled axis crystal, two methods are considered to optimize the EO signal. One method relies on the signal dependence on beam position, while a second approach relies on the laser polarization dependence.

2.5.2.1 Beam position dependence

The principle of the beam position dependence method is to set the polarization of laser and Coulomb field both parallel to the $[\bar{1}10]$-axis of the crystal. As

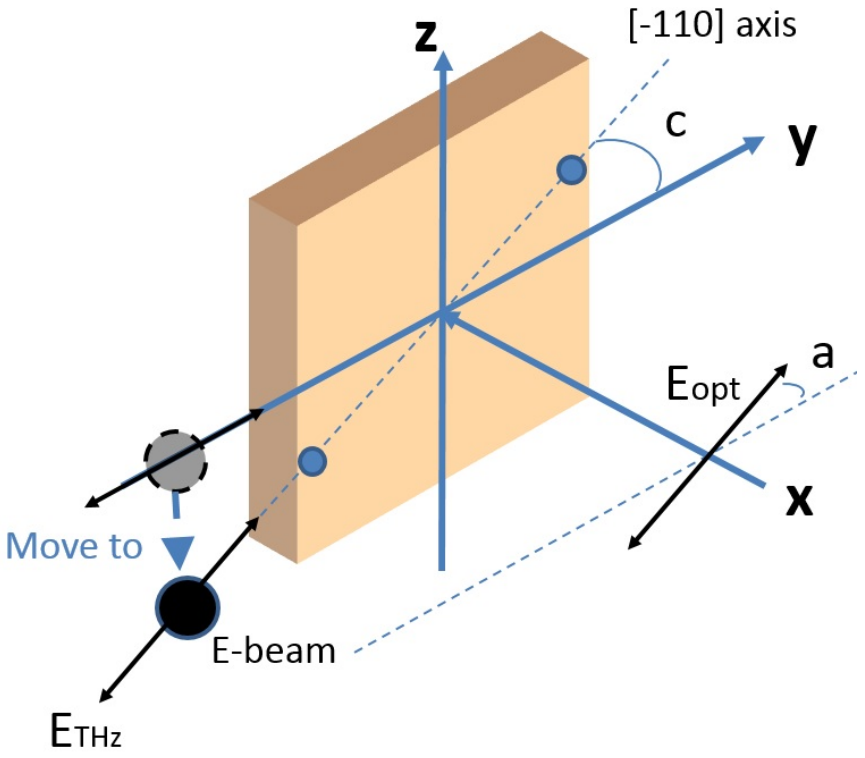

FIGURE 2.9: Scheme of beam position dependence method: crystal installed with $[\bar{1}10]$-axis tilted angle c to y-axis, the polarization of the incident laser has the same tilted angle $a = c$ and set the electron beam lower to the centre in y-z plane. Laser beam and electron beam propagate in x direction.

shown in the figure 2.9, the crystal is installed with $[\bar{1}10]$-axis rotated angle c to y-axis. The polarization of incident laser beam has the same rotated angle $a = c$, and the electron beam is set lower to the center in the extension line of the $[\bar{1}10]$-axis. If 6 mm is supposed between the laser and the electron beam, with 21.34° tilted angle, the electron beam should be set lower 6 mm $\times \tan 21° = 2.3$ mm, and the distance between them becomes to $\frac{6}{\cos 21°}$ mm $= 6.43$ mm. Under these settings, the optimized EOSD signal can be obtained. However, since the electron beam is further away from the laser, the Coulomb field, proportional to $1/r^2$ (r is the distance between electron beam and the laser probe), will drop to $\left(\frac{6}{6.43}\right)^2 = 87\%$. The intensity of the EOSD measured signal is proportional to the magnitude square of the Coulomb field for the crossed polarization detection, which is $(87\%)^2 = 75\%$. In conclusion, for crossed polarization detection, due to the extension on the distance r, the measured maximum EOSD signal will drop down to $\cos^4(c)$.

For CALIFES, the crystal is installed after three quadrupoles and there is no beam position monitor at the position of crystal. Therefore, it is difficult to accurately determine the distance which the electron beam is moved. If the

electron beam is moved vertically 1.5 mm, correspondingly to a 20° rotation in Coulomb field angle, from the maximum signal position, the EOSD signal will drop to 32% of the maximum signal.

2.5.2.2 Laser polarization dependence

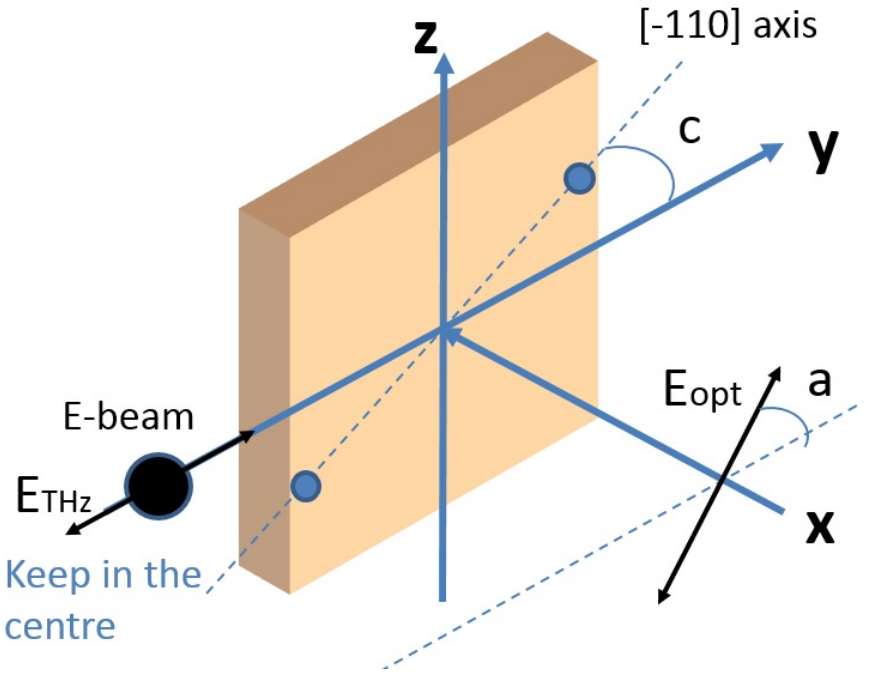

FIGURE 2.10: Scheme of laser polarization dependence method: crystal installed with [$\bar{1}$10]-axis tilted angle c to y-axis, the polarization of the incident laser has a specific tilted angle a and keep the electron beam in the center of beam pipe. Laser beam and electron beam propagate in x direction.

In the laser polarization dependence method, to avoid the above disadvantages, the electron beam is set to the center of the pipe as in normal operating consitions. Meanwhile the crystal is installed with the rotated [$\bar{1}$10]-axis as shown in the figure 2.10. However, by setting the polarization of the laser to a specific angle, a maximum EOSD signal can appear with this fixed Coulomb field angle of 0°.

Figure 2.11 shows the calculation results of EO signal with crystal angle. In the figure, EO signal means a laser intensity normalized signal from crossed polarization setup and it is proportional to Coulomb field intensity. At 0° crystal angle, one edge of the square shape crystal is parallel to horizontal, and the [$\bar{1}$10]-axis of the crystal has 21° offset to horizontal. If the input laser and the Coulomb field from bunches all have horizontal polarization, then the output EO signal can only reach 27% of the maximum signal as shown in figure 2.11(a) at 0° crystal angle. The maximum signal appears at −21° crystal angle, when the polarization

of laser, polarization of Coulomb field and $[\bar{1}10]$-axis are all in horizontal. However, at as the orientation of the crystal can not be changed, an optimized EO signal can also be obtained by changing laser beam polarization. Figure 2.11(b) shows change of the EO signal with crystal angle when input laser polarization is rotated to 36° to horizontal (15° to $[\bar{1}10]$-axis). An optimized EO signal appears when the crystal at 0°. Then the magnitude of this signal can reach up to 66% of the maximum signal magnitude in figure 2.11(a).

2.5.3 Conclusion

For the crossed polarization detection with a 21° rotated $[\bar{1}10]$-axis on ZnTe crystal as the CALFIES experimental configuration, using the method of beam position dependence, described in subsection 2.5.2.1, will induce 25% intensity drop on the measured signal. However, it is not practical at this position on CALFEIS beam line since lack local beam position measurement. However, the method of the laser polarization optimisation, described in subsection 2.5.2.2, will induce 34% drop in signal magnitude below maximum, ideal configuration. With the rotated axis crystal installed in the accelerator, this method is suggested.

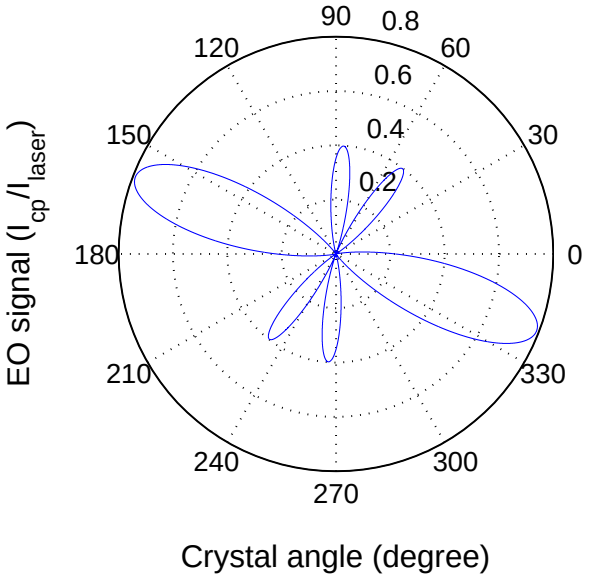

(a) Laser polarization: 0 degree

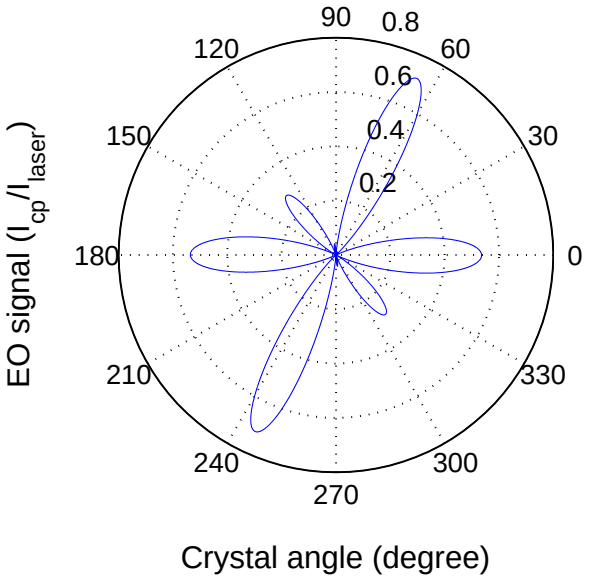

(b) Laser polarization: 36 degree

FIGURE 2.11: Laser intensity normalized EO signal at crossed polarization setup varies with crystal angles. A 2 MV/m horizontal polarized Coulomb field is supposed. $[\bar{1}10]$-axis of the 4 mm ZnTe crystal has 21 degree offset to horizontal. (a) Laser polarization angle is 0 degree to horizontal; (b) Laser polarization angle is 36 degree to horizontal.

Chapter 3

EOSD bunch profile monitor for CALIFES

This Chapter describes details of the EOSD bunch profile monitor. The Chapter is composed by three sections: the first section introduces the EOSD technique and presents numerical calculations for an expected resolution; the second section focuses on details of each part of the bunch profile monitor system, including laser system, pulse stretcher, transfer lines, implementation on the beam line, detection system and synchronization; the last section reports a preliminary beam measurements on laser pulse and e-bunch synchronization.

3.1 Overall design of an EOSD system for CALIFES

3.1.1 EOSD technique

The principle of operation of an EOSD longitudinal profile monitor is shown in figure 1.5: the Coulomb field of an electron bunch is encoded into a linearly chirped broadband laser pulse. Since the laser is chirped linearly, the frequency components of the laser pulse are evenly distributed in time. When the Coulomb field and laser pulse go through the crystal simultaneously, the polarization of the laser pulse varies with the amplitude of the Coulomb field. Crossed polarizers are set on both sides of the crystal in order to transfer the polarization variation into a laser intensity variation. The bunch profile information is thus encoded in the chirped laser pulse both in time domain and frequency domain. To extract the

bunch profile information, a bespoke spectrometer, using a diffraction grating, converts the probe laser beam temporal profile into its spectral profile, which is then detected by a high sensitivity intensified CCD camera.

The core component of the EOSD system is the two-crossed-polarizer set-up. It contains a polarizer, EO crystal, a quarter wave plate, a half wave plate and another polarizer which is crossed with respect to the previous one. As described in Chapter 2, the EO crystal induces a frequency mixing between the Coulomb field and laser pulse due to its non-linear coefficient, resulting in an effective polarization rotation. A combination of a quarter-wave plate and a half-wave plate can compensate the residual birefringence in the EO crystal thereby minimising the background signal for the output probe. The output of the EOSD system is expressed by equation 2.83.

In addition to the geometric factors already discussed in Chapter 2, the frequency response of the EO crystal due to phase matching condition needs to be considered. The response function of the EO crystal due to the phase matching process is shown in section 2.3. The phase mismatching can be expressed approximately as the difference between the optical pulse group velocity and the THz pulse phase velocity:

$$\begin{aligned}
\Delta k\left(\omega,\Omega\right) &= k^{opt}(\omega_s) - k^{opt}(\omega) - k^{THz}(\Omega) \\
&= \left[k^{opt}(\omega) + \frac{\partial k^{opt}(\omega_s)}{\partial \omega_s}\Omega|_{\omega_s=\omega} + \frac{1}{2}\frac{\partial^2 k^{opt}(\omega_s)}{\partial \omega_s^2}\Omega^2|_{\omega_s=\omega} + \dots\right] - k^{opt}(\omega) - k^{THz}(\Omega) \\
&\approx \left[k^{opt}(\omega) + \frac{\partial k^{opt}(\omega_s)}{\partial \omega_s}\Omega|_{\omega_s=\omega}\right] - k^{opt}(\omega) - k^{THz}(\Omega) \\
&= \Omega \cdot \left(\frac{\partial k^{opt}(\omega_s)}{\partial \omega_s}|_{\omega_s=\omega} - \frac{k^{THz}(\Omega)}{\Omega}\right) \\
&= \Omega \cdot \left(\frac{1}{v_g^{opt}(\omega)} - \frac{1}{v_{ph}^{THz}(\Omega)}\right),
\end{aligned} \tag{3.1}$$

where $\omega_s = \omega + \Omega$, ω and Ω stands for the optical pulse ('opt' index) frequency and THz pulse ('THz' index) frequency respectively, the optical pulse group velocity $v_g^{opt} = \frac{\partial \omega}{\partial k}$, and THz pulse phase velocity $v_{ph}^{THz} = \frac{c}{n^{THz}}$. The sum-frequency wavevector $k^{opt}(\omega_s)$ is rewritten by its Taylor expansion at $\omega_s = \omega$, and the higher order expansions are omitted. The refractive index used in this thesis was obtained from [70], and is expressed as:

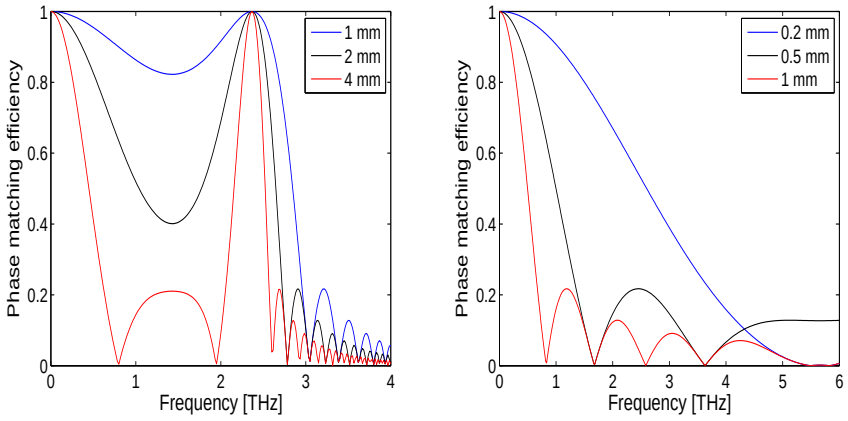

(a) ZnTe (b) GaP

FIGURE 3.1: Efficiency of crystal response functions for ZnTe and GaP: (a) ZnTe with thickness of 1 mm, 2 mm and 4 mm; (b) GaP with thickness of 0.2 mm, 0.5 mm and 1 mm.

$$n_{opt}(f) = \Re\left\{\sqrt{a_1 + \frac{a_2\lambda^2}{\lambda^2 - a_3}}\right\} = \Re\left\{\sqrt{a_1 + \frac{a_2}{1 - a_3(f/c \cdot 10^6)^2}}\right\}, \tag{3.2}$$

where $a_1 = 4.27$, $a_2 = 3.01$, and $a_3 = 0.142\ (\mu m)^2$ for ZnTe, and $a_1 = 2.680$, $a_2 = 6.40$, and $a_3 = 0.0903279\ (\mu m)^2$ for GaP. The input wavelength λ is in the unit of μm and frequency f is in the unit of Hz. The refractive indexes of ZnTe and GaP are shown in figure 3.2(a) and 3.2(b) respectively. The complex dielectric function $\epsilon(f)$ and the refractive index n_{THz} for THz beam are [70]:

$$\epsilon(f) = e_{el} + \frac{s_0 f_0^2}{f_0^2 - f^2 - i\gamma_0 f_0}, \tag{3.3}$$

$$n_{THz}(f) + ik(f) = \sqrt{\epsilon(f)}, \tag{3.4}$$

where $e_{el} = 7.4$, $f_0 = 5.3$ THz, $s_0 = 2.7$, $\gamma_0 = 0.09$ THz for ZnTe, and $e_{el} = 8.7$, $f_0 = 10.98$ THz, $s_0 = 1.8$, $\gamma_0 = 0.02$ THz for GaP. The input THz frequency f is in the unit of THz. The refractive indexes of ZnTe and GaP are shown in figure 3.2(c) and 3.2(d) respectively. As shown in the figures, the lowest resonance frequency is 5.3 THz for ZnTe and 11 THz for GaP. Using the above refractive index data, the phase matching efficiency of the field $\eta = \left|\frac{e^{i\Delta k(\omega,\Omega)L}-1}{\Delta k(\omega,\Omega)L}\right|$ has been calculated and is shown in figure 3.1 with varying crystal thickness (1 mm, 2 mm, 4 mm for ZnTe, and 0.2 mm, 0.5 mm, 1 mm for GaP).

For a 1 mm thick ZnTe crystal, there is a cut off in frequency correspondence at 3 THz. The cut off frequency also reduces with thicker crystals because of

the phase mismatch between the Coulomb field and the laser field. Better time resolution would be obtained by using a 2 mm (or below) GaP crystal, because of its broader bandwidth, as shown in figure 3.1(b). The frequency response of a 200 um GaP extends up to 4 THz, however at the price of lower $\chi^{(2)}$ value and thinner thickness.

The susceptibility $\chi^{(2)}$ can be approximated as being only dependent on the THz frequency as discussed in section 2.3. It can be calculated using $\chi^{(2)}(f) = r_{41}(f)\epsilon^2(f)$ [63]. The frequency dependent linear electro-optic coefficient $r_{41}(f)$ can be written in the form of [70]:

$$r_{41}(f) = d_E \left(1 + \frac{C f_0^2}{f_0^2 - f^2 - i\gamma_0 f}\right), \tag{3.5}$$

where $d_E = 4.25 \times 10^{-12}$ m/V, $C = -0.07$, $f_0 = 5.3$ THz, $\gamma_0 = 0.09$ THz for ZnTe crystal; and $d_E = 1 \times 10^{-12}$ m/V, $C = -0.53$, $f_0 = 10.98$ THz, $\gamma_0 = 0.02$ THz for GaP crystal. The plots of the EO coefficient for ZnTe and GaP crystal are shown in figure 3.2(e) and 3.2(f) respectively. The resonances in figure 3.2(c) and 3.2(d) are due to the excitation of a transverse optical lattice oscillations. These resonance frequencies are at 5.3 THz for ZnTe and 11 THz for GaP.

3.1.2 Laser source selection

Compared to the EOTD scheme, EOSD requires lower laser pulse energy. It can be realised with a commercial fibre laser and can readily provide a sub-picosecond resolution which is suitable for the electron beam in CALIFES. The laser is nonetheless a crucial component of the EOSD system. Its stability and pulse duration directly affect the quality of the final measured signal. Laser pulse energy directly impacts on the final signal-to-noise ratio of the measurement. The intensity of the measured signal also depends on the Coulomb field strength which is related to bunch charge, the characteristics of the EO crystal and the sensitivity of the camera. Some examples of EOSD experiments are now given to convey typical parameters. A laser pulse energy of 1.5 nJ at 1030 nm, with 7 ps chirped laser pulse duration from initial 43 fs, has been demonstrated for measuring a 1.4 ps e-bunch profile of 50 pC charge at 6 mm offset position using a 500 μm thick GaP crystal [56]; Similarly, a laser pulse with 4 nJ energy at 800 nm centre wavelength, chirped to several picoseconds duration from an initial 20 fs, was used to measure a 4 ps length bunches with 0.5 nC bunch charge at 4-5 mm offset position using a 65 um thick GaP crystal [27]. Both of the measurements were performed at Deutsches Elektronen-Synchrotron, Hamburg.

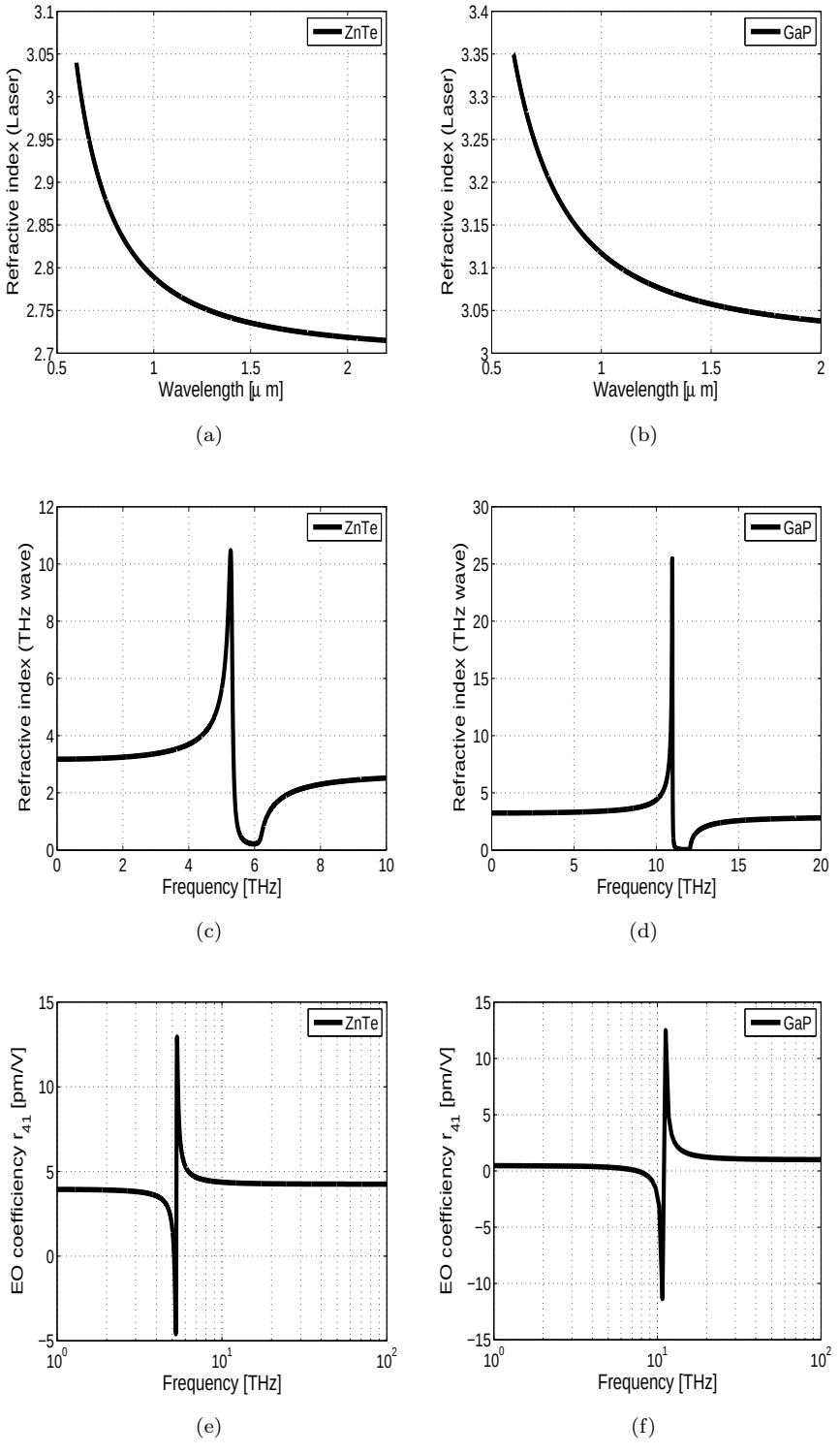

FIGURE 3.2: Parameters of ZnTe/GaP crystal: (a) Refractive index at laser wavelengths in ZnTe; (b) Refractive index at laser wavelengths in GaP; (c) Refractive index at THz range in ZnTe; (d) Refractive index at THz range in GaP; (e) Real part of EO coefficient r_{41} for ZnTe; (f) Real part of EO coefficient r_{41} for GaP.

Table 3.1: Laser performance comparison

Laser	Wave - length (nm)	Input Pulse Energy (nJ)	Crystal	Crystal Thickness (mm)	EO Co-efficient (pm/V)	Output Pulse Energy (pJ)
Ytterbium laser	1060	10	GaP	2.3	0.97	2.39
Erbium laser 1	780	1.8	ZnTe	1.0	3.9	6.26
Erbium laser 2	780	1.2	ZnTe	1.0	3.9	4.17
Erbium laser 3	780	2.7	ZnTe	1.0	3.9	9.39

The wavelength of the laser should be chosen to minimize pulse distortion due to phase-matching in the EO crystal. A 1030 nm wavelength is usually preferred for GaP, and 800 nm for ZnTe, due to the availability of lasers at these wavelengths. As mentioned previously, the thickness of the crystal also plays an important role for getting optimum phase matching. Typically in order to measure several picosecond long bunches, crystal thickness should be thinner than 200 um for GaP and 4 mm for ZnTe at 800 nm center wavelength. However the laser amplitude to be detected after the crossed polarizer is directly proportional to the thickness and the electro-optical coefficient of the crystal. The coefficients [72] are 0.97 pm/V and 3.9 pm/V respectively for GaP and ZnTe. The measured signal to noise ratio can be enhanced if using lasers with high pulse energy combined with high sensitivity and low noise camera. In Table 3.1, estimations of the EOSD expected output signal energy are presented considering different crystals and commercially available laser systems in the year 2011. In order to estimate the output signal energy from the bunch profile monitor, we calculated it based on a 1.4 ps FWHM bunch length with 0.2 nC bunch charge and 185 MeV beam energy. The detection crystal is set at 5 mm away from the electron beam. At the crystal position, a 1.6 MV/m Coulomb field strength is then expected. The last column of Table 3.1 gives the estimations of the expected pulse energy to be detected in a 'crossed polarizer' configuration, which can be considered as one figure of merit for the system's performance. All the laser pulses are assumed to be chirped to 3 ps.

The ytterbium laser in the table is a standard ytterbium fibre laser from MenloSystems (Orange A). This laser can provide a 10 nJ pulse energy and 150 fs pulse duration. In order to satisfy the phase matching condition better, a 2.3 mm GaP crystal is assumed here. For this laser and crystal, a 3 THz bandwidth can

be obtained. Although a higher laser pulse energy is available from the ytterbium laser, it would imply using a GaP crystal which has a lower EO coefficient. As a consequence, only 2.39 pJ pulse energy is expected for the output signal.

Erbium laser 1 is an erbium fibre laser from Toptica Photonics (FemtoFiber pro NIR). This laser can only provide 1.8 nJ pulse energy, and the laser pulse duration is 120 fs. For 780 nm wavelength, the performance of several millimetres thick ZnTe is still acceptable. For this laser and a 1 mm ZnTe crystal, a 3 THz bandwidth can be obtained. Although a lower energy laser pulse than the ytterbium laser is provided, the EO coefficient of ZnTe crystal is higher. As a consequence, 6.26 pJ pulse energy is expected for the output signal.

Erbium laser 2 is a customized laser design based on a laser from MenloSystems (C-Fibre A 780), which adds a 20 m fibre link between oscillator and amplifier. In this scheme, the laser oscillator can be installed in the laser lab to avoid any risk of the radiation damage and the laser amplifier can be set close to the beam line and shielded. With the fibre link, the free space laser transport beam line from laser lab to accelerator area is not necessary. However, it needs extra effort to compensate for the dispersion of the fibre link. With the lower coupling efficiency of the polarisation maintaining fibre, one third of laser energy might be lost. Based on calculation using 1 mm ZnTe, a 4.17 pJ output pulse energy can be expected.

Erbium laser 3 is also a customized laser, but from Toptica Photonics (FemtoFiber pro NIR), and has a pulse picker between the oscillator and amplifier. The pulse picker chooses one in two pulses from the oscillator to pass to the amplifier. In this way the laser's repetition rate can be reduced from 75 MHz down to 37.5 MHz to enhance the pulse energy. The expected output pulse energy from the amplifier could reach 2.7 nJ. As a consequence, a 9.39 pJ pulse energy is expected for the output signal.

Considering the stronger output signal, ZnTe with a 780 nm laser centre wavelength is considered as an appropriate choice for better signal to noise ratio at the price of limited time resolution. The resolution still can cover the CALIFES requirement for bunch profile measurement, which is discussed in the next subsection. The Erbium laser 3, providing the strongest output signal, has been finally selected for CALIFES.

3.1.3 Expected Resolution

The resolution of the EOSD system is determined by the following [73]:

- The distance between crystal and e-bunch: for 2 mm distance between crystal and e-bunch (180 MeV), the resolution limit imposed by the Coulomb field spread will be approximately 10 fs, based on the calculation.
- The frequency response of the EO crystal (material and thickness): the cut off frequency of ZnTe crystal is around 3 THz at a thickness of 1 mm, so the resolution limit induced by phase matching will be approximately 200 fs. For a 4 mm ZnTe, the cut off frequency is 0.8 THz, which implies a 700 fs resolution based on calculation.
- The resolution of the spectrometer: The resolution of the detection is limited by optical diffraction and grating parameters, as well as the sensor. An expected best resolution can be achieved is estimated by the spectrometer dispersion as follows. If a wavelength range of 60 nm covers a detector array of 1000 pixels, this will give a dispersion of 0.06 nm/pixel. A 20 nm bandwidth laser pulse chirped to 3 ps is expected, which gives a dispersion of 9 fs/pixel and full window of 9 ps.
- Limitation from the compressed laser pulse duration and the chirped duration: when the length of the electron bunch is too short, a distortion appears in the spectrum of the output signal. Our laser pulse is 100 fs and will be chirped to 3 ps, giving a limiting duration of the bunch of approximately 1 ps for EOSD. These details were discussed in section 2.4.4.

Therefore the resolution of our EO monitor is expected to be sub-picosecond for bunches longer than 1 ps. In the regular running of CALIFES, a bunch length of more than 6 ps FWHM is typical. In order to adapt to the longer bunch length, a 4 mm ZnTe is used and the laser is chirped to 13.8 ps. Due to this change, with the similar calculation method, the distortion of profile will appear if the bunch length is shorter than 3.5 ps FWHM. The estimated resolution is 700 fs.

3.2 Implementation of the EO monitor in CTF3

The implementation of the system in CALIFES is presented in figure 3.3. Considering the potential for radiation damage in the vicinity of the beam pipe, it

was decided to install the laser away from the accelerator behind shielding. The laser is housed in an optical laboratory located in a technical gallery, 20 metres away from the machine and so requires an optical transfer line. The detection system, including a spectrometer and a camera, is also installed in the laser laboratory. The laser laboratory houses the laser itself, an optical delay line for the fine adjustment of the laser and electron beam synchronization, and the laser pulse stretcher as shown in figure 3.3(b).

The laser beam is sent down to the accelerator hall using an in-air optical transport line which is described later in section 3.2.3.

As shown in figure 3.3(a), the system installed on the beam line is composed of two vacuum chambers. The first chamber, equipped with a mirror is used to inject the laser into the beam pipe. The second chamber houses a ZnTe crystal and an extraction mirror. The two vacuum chambers are both equipped with a motorized translation stage to precisely position the crystal and the mirrors inside the beam pipe. The blue mirror mounts in figure 3.3 are remote controlled via picomotors which are used to adjust the laser path. For monitoring and alignment, six pinhole cameras are installed at several locations in the optical system in order to check the size and position of the laser.

There is a half-wave plate before the first chamber, and another half-wave plate and a quarter-wave plate after the second chamber. The first half-wave plate is used to change the incident laser polarization and the second half-wave plate and the quarter-wave plate are used to compensate the residual birefringence induced by the EO crystal. The last two wave plates and a polarizer are mounted in motorized rotation stages. All the motors, 16 in total, can be remotely controlled. After emerging from the vacuum chamber, the laser is steered through the wave plates and polarizer, and is then coupled into an optical fibre, which brings it back to the laser room. The laser pulse is then measured by a home made spectrometer and a gated intensified CCD camera.

In addition, an OTR screen (200 μm aluminium coated silicon wafer) was installed in the second vacuum chamber. It provided a tool to measure the timing difference between the electron bunch and the laser pulse using a streak camera.

Additionally, two beam loss monitors have also be installed close to the two vacuum chambers to measure if the beam or beam halo are impinging on the mirrors and the crystal.

All these sub-systems are described in more details in the following sections.

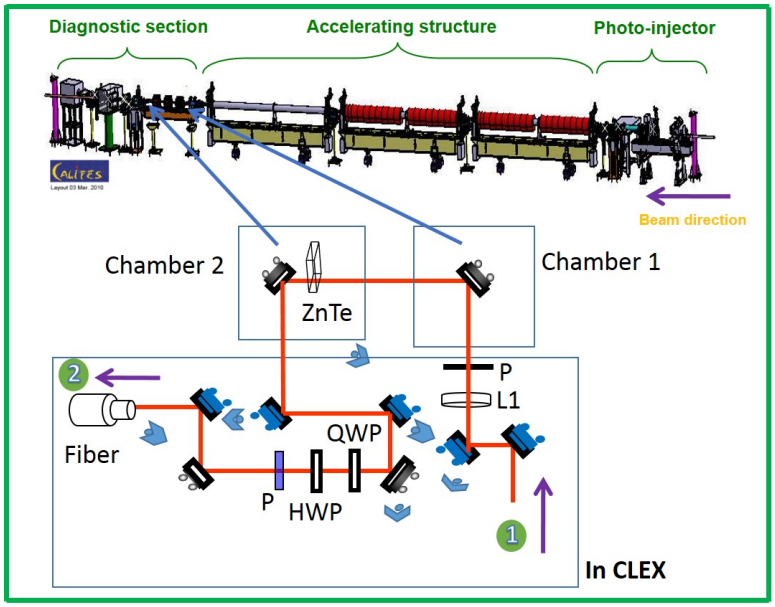

(a) In CLEX

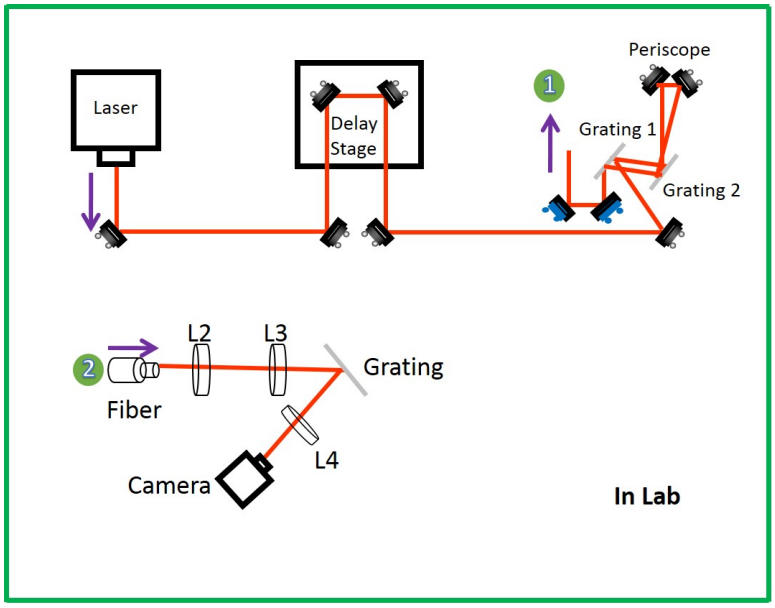

(b) In Lab.

FIGURE 3.3: EO monitor scheme: The laser pulse, coming from the laser head in the lab, passes through an optical delay stage and a pair of gratings, and then is sent to CLEX. The laser goes through lens L_1 and is injected into accelerator beam pipe in Chamber 1, and then modulated by the e-beam at the ZnTe crystal in Chamber 2. The laser then comes out of beam pipe and passes through a quarter-wave plate (QWP), a half-wave plate (HWP) and a polarizer (P), and is coupled into a fibre for transport back to the lab. A spectrometer, comprising lens L_2, L_3, a grating and L_4, provides the laser spectrum on a camera.

TABLE 3.2: Laser parameters

Center Wavelength	Ave. Output Power	Pulse Width	Linear Polarization	Beam Shape(TEM_{00})	Beam Divergence
1560 nm	>350 mW	<120 fs	>95% (horizontal)	$M^2 < 1.2$, $\phi = 3.5$ mm (FWHM)	<2 mrad
780 nm	>120 mW	<120 fs	>95% (horizontal)	$M^2 < 1.2$, $\phi = 0.7$ mm (FWHM)	<1 mrad

3.2.1 Laser system

The laser is a customized Erbium fibre laser from Toptica Photonics AG. It is composed of an oscillator, a pulse picker and an amplifier working at 1560 nm wavelength. The oscillator is configured to run at 74.963 MHz repetition rate (close to the standard 80 MHz version originally designed by the company), which is compatible with the 40th sub-harmonic of the 3 GHz CALIFES master clock. In order to extract more energy from the amplifier, a pulse picker has been added after the oscillator to pick up every second pulse, bringing the repetition rate down to 37.5 MHz. The laser pulses are then compressed using a pair of prisms just before the Second Harmonic Generation (SHG) unit, which finally generates 780 nm laser pulses. A mirror can be inserted in front of the SHG unit to select the output wavelength (1550 nm or 780 nm) is to be used. The main characteristics of the laser beam are displayed in table 3.2.

With the pulse picker, the output pulse energy at 780 nm is 3.6 nJ. The pulse picker is a commercial EO amplitude modulator manufactured by Jenoptik. It can achieve 800:1 extinction ratio at 790 nm and its half wave voltage is 4 V. A RF amplifier, providing 28 dB gain with 0-11.7 GHz bandwidth (Model 5868, manufactured by Picosecond), is used to provide the required voltage to drive the modulator. In normal conditions the amplifier provides a signal of -5 to 3 V at 37.5 MHz to the laser pulse picker.

In order to synchronize the laser pulse to the electron beam of CALIFES, a low jitter laser synchronization system, which comes from Toptica, is essential. A photo-diode inside the laser head measures the 75 MHz repetition rate from the laser oscillator, and this signal is input to the synchronization box. The signal is then amplified and compared with a 74.963 MHz signal derived from the 40th sub-harmonic of 3 GHz CALIFES RF system. The phase difference between these two signals is connected to the input of a Proportional Integral Differential

(PID) regulator, which provides a feedback loop minimizing this phase difference. The PID regulator generates two output signals which control a piezo motor and a motorised translation stage in the laser head. The translation stage becomes only active if the required adjustment is not in the range of piezo motor. The motor only correct the requiring offset if it is not capable of getting any phase lock.

3.2.2 Delay line and stretcher in the lab

In the laser room, an optical delay line and a laser pulse stretcher have been implemented directly after the laser head. The optical delay line is based on 2 mirrors mounted on a translation stage (Thorlabs: NRT150/M). It has a 2 μm minimum repeatable incremental movement and 150 mm travelling range, which can provide 13 fs step increment and 1 ns scanning range.

The laser pulse must also be chirped to pulse duration longer than the bunch length. The chirp can be achieved either by a certain length of SF11 glass for 1.4 ps bunch or by a pair of gratings for 6 ps bunch, as shown in figure 3.4.

The set-up using SF11 glass, as shown in figure 3.4(a), is installed at the exit of the optical delay stage. SF11 glass can achieve almost linear chirp around 780 nm wavelength with high refractive index (n=1.76583 at 780nm) and good transparent (anti-reflect coating on both ends). Its refractive index can be calculated by equation 3.6[74] with wavelength micrometers:

$$n = \sqrt{1 + \frac{a_1\lambda^2}{\lambda^2 - b_1} + \frac{a_2\lambda^2}{\lambda^2 - b_2} + \frac{a_3\lambda^2}{\lambda^2 - b_3}}, \tag{3.6}$$

where $a_1 = 1.73759695$, $a_2 = 0.313747346$, $a_3 = 1.89878101$, $b_1 = 0.013188707\ \mu m^2$, $b_2 = 0.0623068142\ \mu m^2$, and $b_3 = 155.23629\ \mu m^2$.

The laser passes through two 150 mm long rods of SF11 glass. To chirp the laser pulse to around 2 ps, it must pass once in the the first rod and twice in the second section so that the total path length for chirping is 450 mm. A Gaussian profile laser pulse can be chirped from 124 fs to 2 ps. Figure 3.5 shows the modeled laser pulse chirp, based on the measured laser pulse spectrum. The blue curve, green curve, red curve and black curve show the initial pulse temporal profile, the pulse temporal profiles after passing through a 150 mm SF11 rod once, twice and three times respectively. The magenta curves are the Gaussian fittings for each profile. This calculation shows the laser pulse can be chirped from 124 fs to

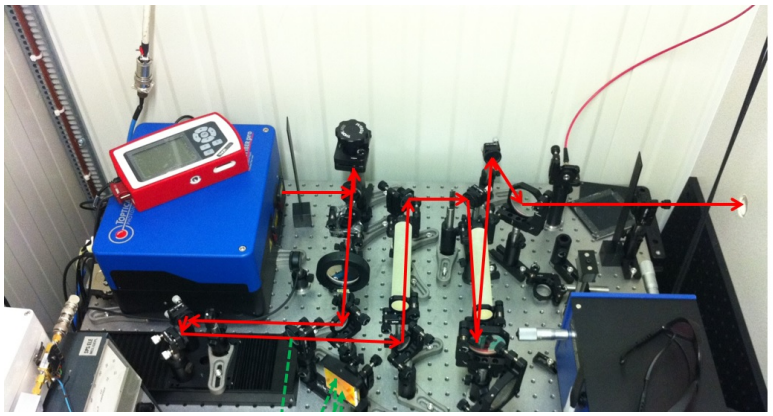

(a) SF11 glass stretcher

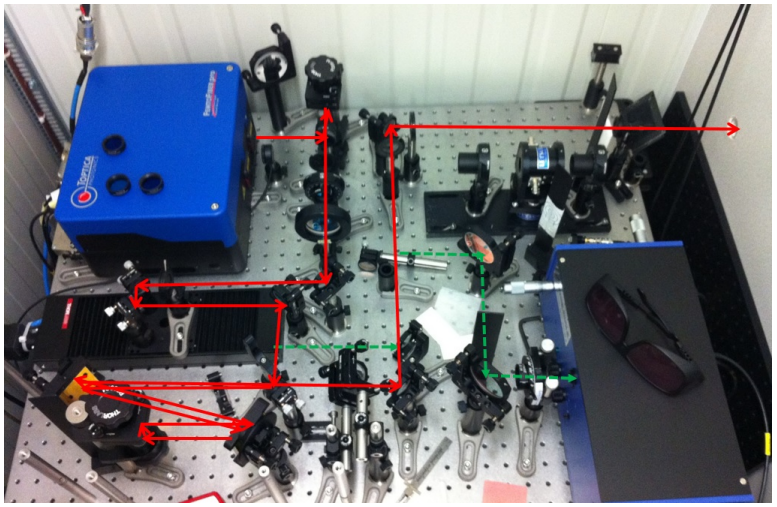

(b) A pair of gratings stretcher

FIGURE 3.4: Two types of the laser pulse stretcher. (a)SF11 glass stretcher: Each glass rod has 150 mm length. Laser pulse passes through the first rod once and the second rod twice. (b) A pair of gratings stretcher: Laser pulse goes through the two gratings. Then it is lifted up by a periscope and reflected back. The back laser pulse goes through the two gratings once more.

0.6 ps, 1.2 ps and 1.9 ps after passing the SF11 rod once, twice and three times respectively.

Compared with the method of SF11 glass chirping, the gratings are able to chirp the laser pulse up to 16 ps but they introduce more losses. The layout of the grating pair stretcher is shown in figure 3.4(b). The laser pulse traverses the pair of gratings, is then lifted up in vertical space by a periscope, and comes back through the grating pair again. Then it passes over the mirror before the first grating and goes to CALIFES.

A diagram of the two grating stretcher is shown in the figure 3.6. The laser is incident on grating 1 and is diffracted to grating 2. As the two gratings are parallel

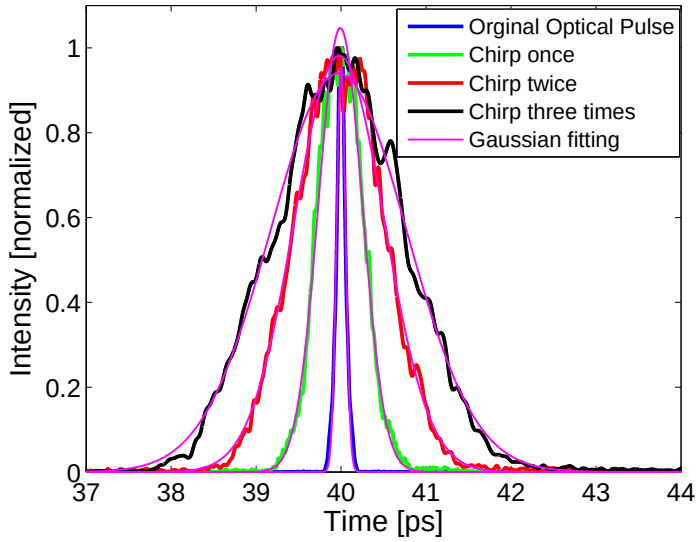

FIGURE 3.5: Modeled laser pulse chirp based on measured laser spectrum: blue curve is the initial pulse temporal profile. Green curve, red curve and black curve show the pulse temporal profiles after passing through a 150 mm SF11 rod once, twice and three times respectively. The magenta curves are the Gaussian fittings for each profile.

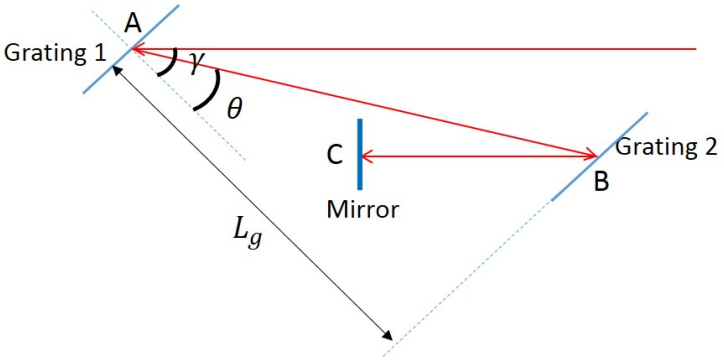

FIGURE 3.6: Scheme for the two gratings stretcher: Laser pulse has incident angle γ, diffracted angle θ on the first grating, and L_g is the perpendicular distance between the two gratings. A, B and C are the beam positions on the grating 1, grating 2 and the mirror respectively.

to each other, the diffracted laser pulse after the second grating is parallel to the incident light of the first grating. A mirror is set after grating 2 and perpendicular to the laser path. So the laser will go back through its coming path. In the set up, the two gratings are laser compression gratings from Spectrogon AB with 1200 grooves/mm, 50 mm by 50 mm size. The gratings have 77% efficiency at 780 nm wavelength for the polarization of the incident laser which is perpendicular to the grating grooves, and at 55° incident angle. The efficiency is defined as the amount of the incident power that is diffracted into the first order. A periscope was then set at the mirror position to raise the laser pulse by 3 mm, and then

the incident laser and the output chirped laser can be separated. In the scheme, the angle γ and θ are the incident angle and diffracted angle of the first grating, and L_g is the perpendicular distance between the two gratings. The path P from A, by B, to C can be expressed by:

$$P = \frac{L_g}{\cos\theta}\left[1 + \cos\left(\theta - \gamma\right)\right], \tag{3.7}$$

$$\sin\theta + \sin\gamma = \frac{2\pi c}{\omega d}, \tag{3.8}$$

where the ω is the laser angular frequency, c is light velocity and d is the slits spacing. Combining the above equation 3.7 and the grating equation 3.8 for the first diffraction order, the phase advance Φ after single passing through the stretcher for each frequency components can be calculated and shown in Equation 3.9:

$$\Phi = \frac{\omega L_g}{c}\left[\cos\gamma + \frac{1}{\sqrt{1-\left(\frac{2\pi c}{\omega d} - \sin\gamma\right)^2}} + \sin\gamma\frac{\frac{2\pi c}{\omega d} - \sin\gamma}{\sqrt{1-\left(\frac{2\pi c}{\omega d} - \sin\gamma\right)^2}}\right]. \tag{3.9}$$

The equation 3.9 shows the phase of the stretcher is only related to the incident angle γ and light angular frequency ω as the slits spacing d is a constant. In order to simplify the equation, the diffraction angular θ is induced into this equation, and it can be rewritten as:

$$\Phi = \frac{\omega L_g}{c}\left(\cos\gamma + \frac{1}{\cos\theta} + \sin\gamma\tan\theta\right). \tag{3.10}$$

As the phase can be expressed in a Taylor expansion at a central frequency in Equation 3.11, its group delay $\frac{d\Phi}{d\omega}$, and group velocity dispersion $\frac{d^2\Phi}{d\omega^2}$ which induces a linear frequency chirp, can be calculated and shown as:

$$\Phi(\omega) = \Phi(\omega_0) + \frac{d\Phi}{d\omega}|_{\omega=\omega_0}(\omega-\omega_0) + \frac{1}{2}\frac{d^2\Phi}{d\omega^2}|_{\omega=\omega_0}(\omega-\omega_0)^2 + \cdots, \tag{3.11}$$

$$\frac{d\Phi}{d\omega} = \frac{L_g}{c}\left(\cos\gamma + \frac{1}{\cos\theta} + \sin\gamma\tan\theta\right) + \frac{\omega L_g}{c}\cdot\frac{\sin\theta+\sin\gamma}{\cos^3\theta}\cdot\frac{-2\pi c}{\omega^2 d}, \tag{3.12}$$

$$\frac{d^2\Phi}{d\omega^2} = \frac{4\pi^2 c L_g}{d^2\omega^3}\frac{1}{\cos^3\theta}\left[1 + \frac{6\pi c}{\omega d}\cdot\frac{\sin\theta}{\cos^2\theta}\right]. \tag{3.13}$$

Based on the above equations, a calculation result of the two-grating stretcher is shown in figure 3.7(a). In the calculation, a 138 fs laser pulse is incident on the first grating with 55° incident angle, and the distance L_g between the two gratings is 20 cm. The calculation shows the stretcher can chirp the laser pulse to 13.2 ps. Figures 3.7(c) and 3.7(d) show the auto-correlator measurements of initial and chirped laser duration respectively. The Gaussian fitting for the auto-correlator results implies the original laser duration is 138 ± 5 fs and chirped pulse is 13.1 ± 0.1 ps. The results are FWHM and have already timed a Gaussian factor of 0.707. This factor transfers the intensity autocorrelation width of a pulse to the intensity width for a Gaussian profile. The spectra of these two pulses are shown in 3.7(b), and they are as expected.

3.2.3 Optical transfer line and OTR transfer line

An optical line, a schematic of which is shown in figure 3.8, has been designed to transport the laser probe from the laser room to the vacuum chamber which houses the EO crystal in the beam pipe. The optical line is composed of four lenses ($f_1 = f_4 = 515.3$ mm, $f_2 = f_3 = 5153$ mm, $\phi = 50.8$ mm) with 780 nm AR coatings and seven high reflection (over 99.5%) mirrors. The detailed parameters of this laser transfer line can be seen in the table 3.3.

The laser transfer line was evaluated using the ABCD method of Gaussian pulse propagation with the parameters and settings in table 3.3. The laser pulse has a 1.2 mm diameter at 780 nm and a divergence less than 1 mrad. It is first collimated by lens L1 in the laser lab, and is transferred into CLEX. Lens L2 and L3 are located in the accelerator hall, and propagate the laser to the EO monitor stage before the first vacuum chamber. The last lens, L4, is used to focus the laser on to the EO crystal. The calculation shows the beam size at the crystal position is 1.4 mm. However, in the installation, the lens L4 at 567.7 mm before the crystal is not practical. The lens L4 to the crystal is approximately 30 cm longer than the design, which leads to the beam size on the crystal is around 2 mm and diverging.

For measuring the relative arrived time between the laser and e-bunch, an OTR transfer line is designed and built to bring this light back to the camera lab. As depicted in figure 3.9, the optical line is composed of only two lenses ($f_1 = 1000$

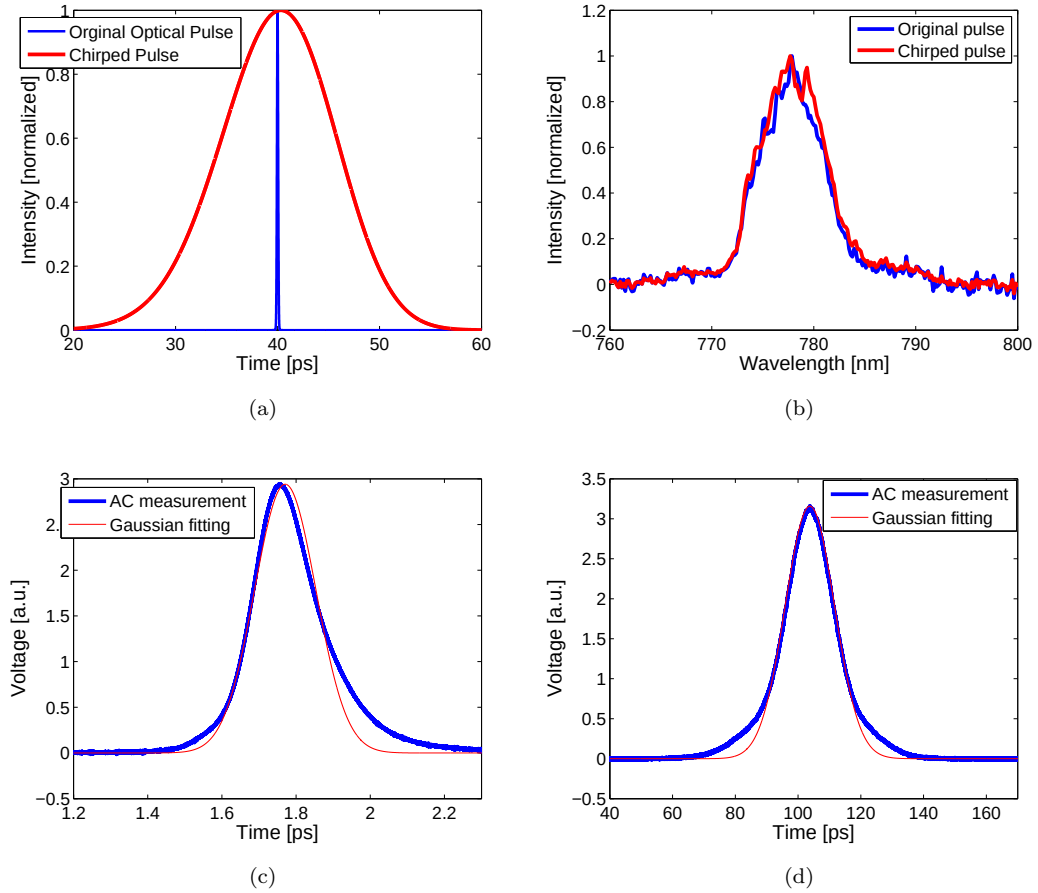

FIGURE 3.7: Laser pulse duration and spectrum: (a) Grating stretcher calculation: original 138 fs laser pulse is chirped to 13.2 ps by the grating stretcher; (b) Spectrum measurement of the original and the chirped pulse; (c) Autocorrelator measurement for the original pulse (without applying the Gaussian factor 0.707); (d) Autocorrelator measurement for the chirped pulse (without applying the Gaussian factor 0.707).

mm, $f_2 = 75$ mm, $\phi = 50.8$ mm) with broadband coatings from 650 nm to 1050 nm and seven high quality mirrors. The detailed parameters of this transfer line can be seen in the table 3.4.

The electron beam size is focused to 0.11 mm by 0.05 mm at the EO crystal

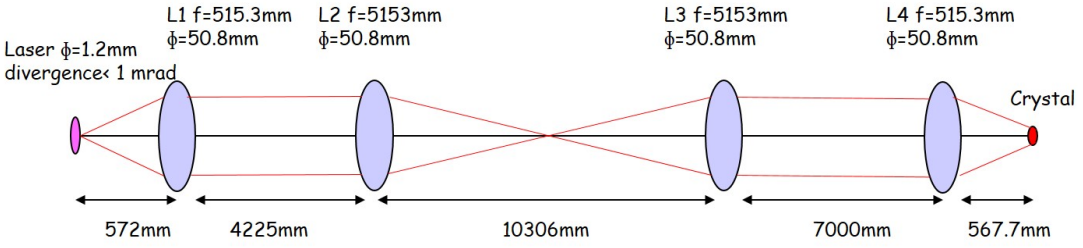

FIGURE 3.8: Laser transfer line

TABLE 3.3: Parameters for the laser transfer line

Component	Laser head	L1	L2	L3	L4	crystal
Aperture (dia.)	1.2 mm	50.8 mm	50.8 mm	50.8 mm	50.8 mm	10 mm
Focal length	None	515.3 mm	5153 mm	5153 mm	515.3 mm	None
Distance to last component	0	572 mm	4225 mm	10306 mm	7000 mm	567.7mm
Position	laser lab	laser lab	CLEX wall	CLEX ceil-ing	CLEX EO stage 1	CLEX CAL-IFES

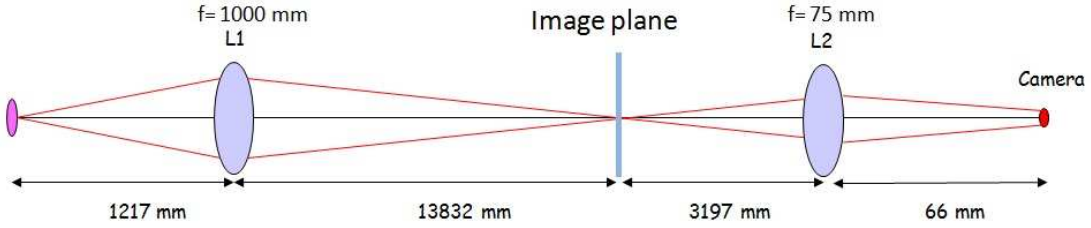

FIGURE 3.9: OTR and laser optical line

position and the OTR photons are generated with a divergence angle of 0.16 degree by a 185 MeV beam energy. The OTR photons are collected by the lens L1 with 1000 mm focal length after 1.2 m and imaged to a plane which is 13.8 m after lens L1. The second lens L2, which is located in the streak camera lab, finally focuses the OTR photons on the streak camera. The purpose of this transfer line is to provide arriving time information for laser and OTR photons rather than an image of them. Considering the good sensitivity of the streak camera, the transfer line can be built only by two lens at a price of low image quality.

3.2.4 Description of the optical system in CALIFES

The main components of the EOSD bunch profile monitor were installed in the accelerator hall, close to the beam line, as shown in figure 3.10. The laser was located in laser lab which is not exposed to radiation.

As shown in figure 3.10(a), the laser beam, coming from the ceiling, is then injected into the beam line in the first vacuum chamber which is equipped with a

TABLE 3.4: Parameters for the OTR transfer line

Component	OTR screen	L1	L2	streak camera
Aperture (dia.)	0.1 mm (beam size)	50.8 mm	50.8 mm	None
Focal length	None	1000 mm	75 mm	None
Distance to last component	0	1217 mm	17029 mm	66 mm
Position	CLEX CALIFES	CLEX ceiling	Streak camera lab	Streak camera lab

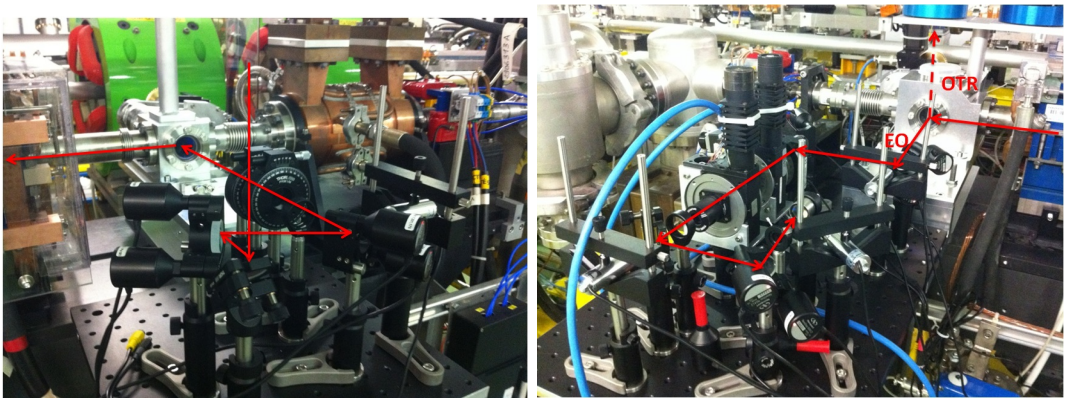

(a) Stage 1 (b) Stage 2

FIGURE 3.10: Two stages of the bunch profile monitor: (a) Stage 1: Laser comes from ceiling and is reflected by two mirrors. A half-wave plate and a polarizer after the mirrors in order to induce proper polarized laser into the vacuum chamber; (b) Stage 2: Laser comes out of a vacuum chamber, and passes through a half-wave plate, a quarter-wave plate and a polarizer. Then it is reflected by two mirrors, and is finally coupled into a fibre.

silver mirror mounted on a retractable arm. A half-wave plate and a polarizer, located right before the vacuum chamber view port, are used to adjust the polarization of the incident laser beam to be horizontal. As shown in figure 3.10(b), the laser probe is then steered to a second vacuum chamber downstream, which holds an EO crystal and an extraction mirror. Both of the crystal and the mirror are mounted on the same retractable arm. The crystal and the extraction mirror sit in the second vacuum chamber at 1.6 m downstream of the insertion mirror.

As the laser coming out of the second chamber, it passes through a quarter-wave

plate, a half-wave plate and a polarizer. After the polarizer, the polarization encoded bunch profile is transformed into a laser intensity profile. This profile is then optically coupled via a multi-mode fibre (0.22 NA, 50 μm core) back to the laser laboratory. The detection system is composed of a home made spectrometer and a gated, intensified CCD camera (PCO dicam pro).

In total, ten actuators on five mirrors and six finger cameras have been installed around the insertion and extraction vacuum chambers in order to remotely steer and monitor the laser from a control room.

3.2.5 Two vacuum chambers

The two chambers are both made of aluminium, designed and manufactured by CERN, and are shown in figure 3.11(a) and 3.11(b). All the view ports are anti-reflection coated fused silica view ports from MDC Vacuum Products Sarl. A detailed view of the crystal housing in the second chamber is shown in figure 3.11(c). The chamber is designed to provide a mechanical mount for 1-4 mm thick ZnTe crystal along with an extraction mirror.

The second vacuum chamber is also equipped with an OTR screen made by a 200 μm thick aluminium coated silicon wafer. It is used to monitor the time overlap between the electron beam and the laser probe on the streak camera. As the electrons pass through the screen, they emit OTR photons which are then sent via a second optical line to the laser laboratory, where the streak camera sits. At the same time, the laser photons are reflected by the OTR screen following the same path as the OTR photons so that the laser and OTR photons can both be measured simultaneously by the streak camera. The delay between the electrons and the laser could be controlled either by a phase shifter installed on the RF signal for locking the laser oscillator, or by the optical delay stage with fine scanning over a range of 1 ns.

3.2.6 Spectrometer design

A home-made spectrometer is used to decode the bunch profile information from its spectrum. Due to a linear chirp on the laser pulse, the bunch profile temporal information is linearly correspond to its spectra profile. The scheme of the home-made spectrometer is shown in the figure 3.12. The laser comes out of a fibre collimator (Thorlabs F220FC780, f=11.7 mm, diameter 11 mm). As spatial resolution is $\Delta l = \frac{1.22\lambda f}{D}$, where the D is the aperture of the optical elements and

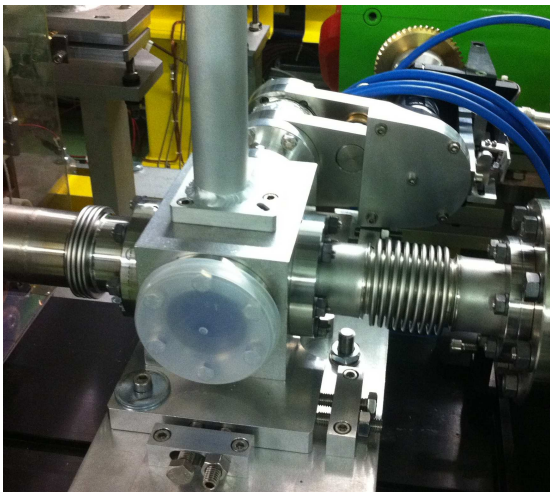

(a) Photo of chamber 1

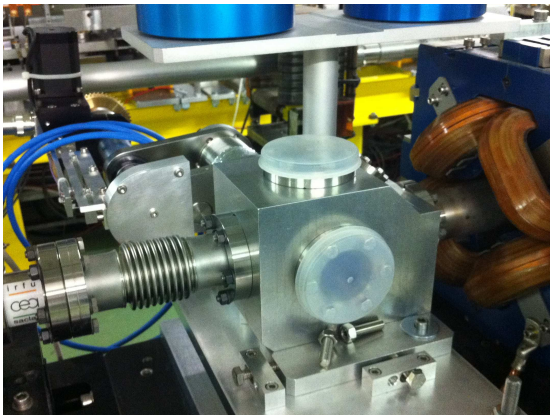

(b) Photo of chamber 2

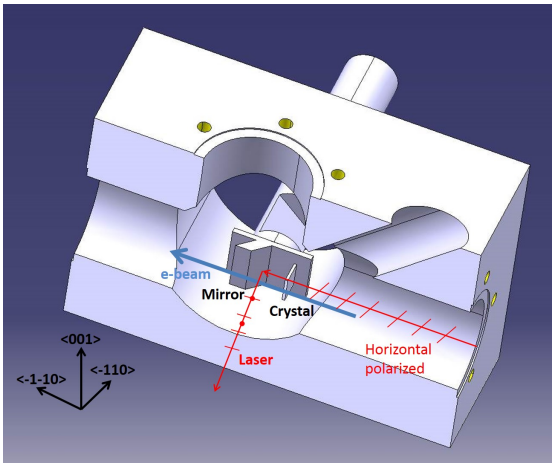

(c) Scheme of the chamber 2

FIGURE 3.11: Photos and design scheme of the two chambers: (a) Chamber 1 is used for injecting the laser pulses into accelerator beam pipe. An injection mirror is mounted inside this chamber on a retractable arm; (b) Photo of chamber 2; (c) Chamber 2 includes an EO crystal and a mirror. They are mounted on a retractable arm. The mirror steers the laser out of the beam pipe. The laser pulse is horizontal polarised. Crystal $\bar{1}10$-axis is horizontal.

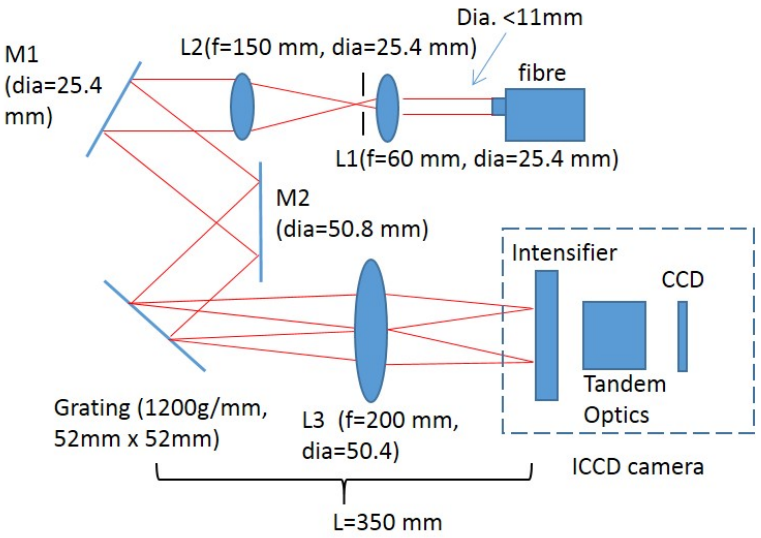

FIGURE 3.12: Spectrometer scheme: Laser pulse comes out of a fibre collimator, and its beam size is expanded by lens L_1, L_2. After mirror M_1, M_2, the laser is diffracted by the grating and focused on the image intensifier of a CCD camera by lens L_3.

f is focal length, a better spatial resolution can be obtained by expending the beam transverse size to fill the apertures of optical elements. Therefore the laser beam size is expended to more than double by two 1-inch lens with 60 mm (L_1) and 150 mm (L_2) focal length respectively. The spatial resolution limited by the diffraction is 6.9 μm.

There is a slit at the focal point between the two lens. The original purpose of the slit is to improve the resolution of the spectrometer. However, considering the 50 μm multi-mode fibre core size, any disturbance to the fibre itself will induce position displacement of frequency components of the laser pulse at the focal point. Therefore, the slit may lead to missing frequencies in the measurement. This error can be reduced by averaging measurement results. In this thesis, the measured bunch profile are 50 shots averaged if no specific indication. The multi-mode fibre also induces noise in the measurement due to the interference of the different frequency components of the laser pulse. This noise can be reduced by smoothing algorithms as described in [70]. This error can also be reduced by implementing a single-mode fibre which has an approximately 8 μm core size, but at the price of lower coupling efficiency and laser position tolerance.

After two mirrors, the collimated beam is reflected and dispersed by a grating with 1200 graves per mm and 52 mm by 52 mm size (Holographic grating from Richardson Gratings, efficiency >70% at 800 nm). Finally the different reflective angles, which show the different frequencies, are focused at their correspond

TABLE 3.5: Spectrum calibration

Lamp line (nm)	758.74	760.15	768.52	769.45	785.48	805.95
Pixel number	235	266	448	468	824	1280

positions on the image intensifier of a ICCD camera by a 2-inch lens with 200 mm focal length. There are tandem optics inside the ICCD camera between the image intensifier and the CCD, which provides an image magnification factor of 1/2.17. The CCD has 1280 by 1024 pixels with a 6.72 μm pixel size which is similar to the system spatial resolution.

Based on the grating equation 3.14:

$$\beta = \arcsin\left(m\lambda/d - \sin\alpha\right), \tag{3.14}$$

where m is the diffraction order, λ is wavelength, d is groove spacing of the grating, and α and β are incident and exit angle respectively. The linear dispersion can be calculated by a product of the angular dispersion $\frac{d\beta}{d\lambda}$ and the effective focal length f of the L_3 lens. Equation 3.15 shows the reciprocal linear dispersion P:

$$P = 1/\left(\frac{d\beta}{d\lambda}\cdot f\right) = \frac{d\cos\beta}{mf}. \tag{3.15}$$

The diffraction angle β is designed for 45° in our spectrometer, which corresponded to a 13° incident angle, and the focal length of L_3 is 200 mm. Therefore, based on this equation, for wavelength at 780 nm, the dispersion of the spectrometer on the ICCD intensifier we can expect is 2.93 nm/mm. Considering the internal image magnification factor 1/2.17 and the pixel size is 6.72 μm, the dispersion on the CCD is 6.36 nm/mm, which is 0.043 nm/pixel.

In order to calibrate our home-made spectrometer, a calibration lamp (ORIEL 6031 from NEWPORT) is used as a stable light source. Since the spectrum of the light source is known, a measured spectrum for this light source can be used to calibrate the spectrometer, as shown in figure 3.13.

Measured by the home-made spectrometer, the mapping between the lamp peak positions and their correspond pixel positions is shown in table 3.5. Since there is distortion on the border of the CCD image, the central data of the image is more reliable. Only the central part (40 lines) of the calibration data is used.

As a result of linear fitting, the wavelength can be expressed in nanometres as: Wavelength $= 0.045 \times \text{Pixel} + 748.215$. The fitting result indicates the spectrometer has a dispersion of 0.045 nm/pixel with 0.3% standard error, which is slightly

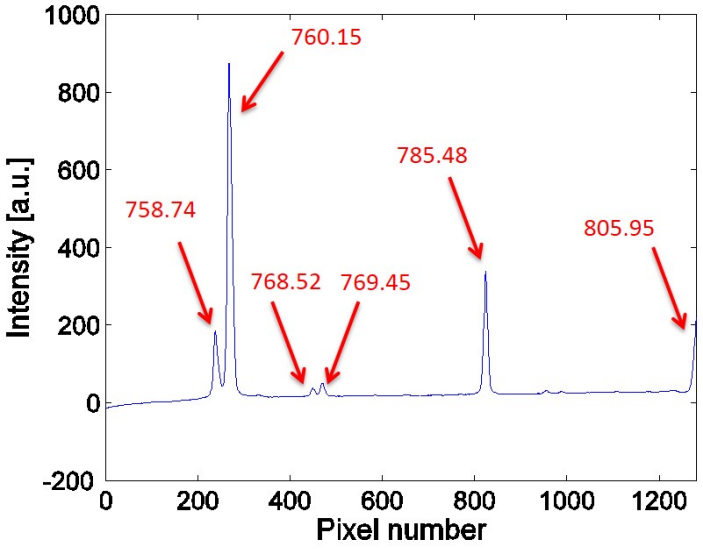

FIGURE 3.13: Spectrum profile of the calibration lamp

broader than the expected dispersion 0.043 nm/pixel, since the measured result includes all the effects leading to reducing the final resolution. In order to get the resolution of the spectrum, the peak at 785.48 nm in figure 3.13 is selected. Most of the spectrum lines emitted from the Kr lamp have a width of less than 0.001 nm. A Gaussian fitting on the 785.48 nm peak shows it has a FWHM width of 10 pixels, which implies 0.45 nm resolution.

3.2.7 Gated ICCD camera

The camera for recording the EOSD measurement data is a gated intensified CCD camera (DICAM Pro), manufactured by PCO. Imaging.

The principle of the ICCD camera is that an object is firstly imaged on a photo-cathode which emits electrons when illuminated. Then these generated electrons pass through a Micro Channel Plate (MCP) and each electron excites multi-electrons under a circumstance of high voltage on the MCP. As a consequent, the electric signal is amplified. At the end, these electrons hit a phosphor screen which emits more photons. As a result, the incident light is intensified.

A 25 mm GaAs MCP photo-cathode is selected for 780 nm wavelength. As shown in Table 3.1, a 9.39 pJ EOSD signal pulse energy is assumed to enter the camera. Considering the pulse will cover half of the 1280 pixels, the energy can be approximately converted to 7.4×10^4 photons. Considering 50% energy loss before entering the ICCD camera and 25% quantum efficiency (QE), only

9246 electrons can be obtained before the amplifier in average. The broader the laser pulse the fewer the electrons on the camera amplifier. Therefore the camera intensifier is necessary and the ICCD camera is sensitive enough for the signal.

3.2.8 Laser-Electron Synchronization

The running of CALIFES is based on several trigger and synchronization signals: a 50 Hz mains synch, 0.83 Hz general start, 250 MHz counters and a timing unit, as shown in figure 3.14. The 0.83 Hz is synchronized to the 50 Hz mains. A 0.83 Hz signal for the CALIFES laser pulse picker and for streak camera trigger is generated by the 0.83 Hz general start signal and a counter signal. The same streak camera trigger signal is also used for trigging our EOSD system.

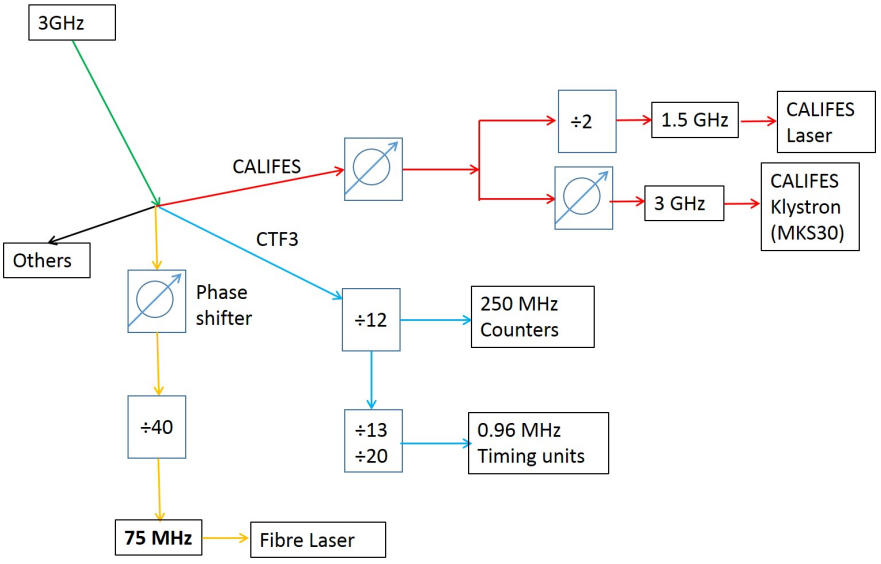

FIGURE 3.14: RF timing for CTF3: 3 GHz master clock is mainly split to CALIFES application, CTF3 timing units and the fibre laser for EO bunch profile monitor.

From measurements and testing, the streak camera trigger was seem to be well synchronized to the bunches. After synchronizing our laser to the clock, the laser clock was found to beat with the trigger signal on oscilloscope as shown in figure 3.15(a).

The yellow curve is the trigger signal for streak camera with 0.83 Hz. The light blue curve is the 75 MHz laser RF signal. The oscilloscope is running at persistent mode. So it recorded the 8 states between these two signals. Five states of them are common and the other three intermittent.

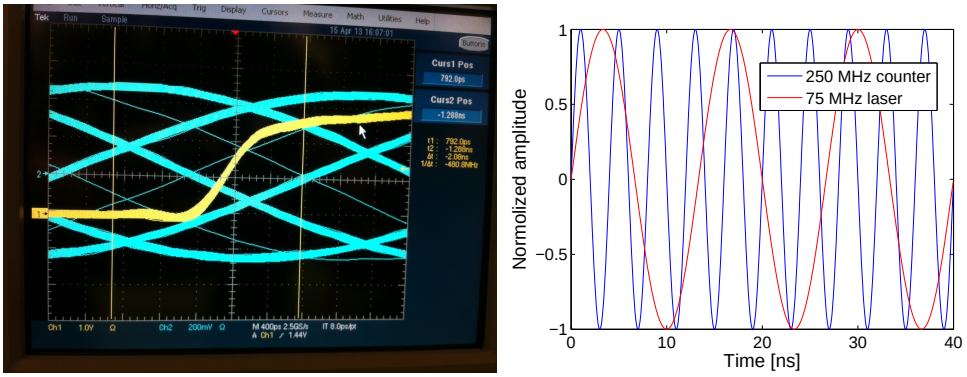

(a) (b)

FIGURE 3.15: Measurement and calculation of 75 MHz laser clock and 250 MHz counter: (a) Streak camera trigger and Laser RF on oscilloscope (400ps/ grid): 8 states of 10 between these two signals are recorded; (b) Calculation for 250 MHz counter RF signal and 75 MHz laser signal: a complete period includes 10 pulses of the counter.

The reason for this beating was that the streak camera trigger is generated by a 250 MHz counter which is the 12th sub-harmonic of the master clock. Our laser system is synchronized to a 75 MHz clock which is the 40th sub-harmonic of the master clock. These two sub-harmonic signals are not integer multiples of each other. Figure 3.15(b) shows these two signals. It shows a complete period of these two signals includes 10 pulses of the counter. Since the 0.83 Hz trigger is generated by the 250 MHz counter, there are ten possible states between the laser clock and the trigger.

To solve the beating problem, we changed the timing unit of the CTF3 system. In the beginning, the timing signal of CTF3 was generated from either the 250 MHz counter or a 19.6 MHz (3 GHz divided by 12 and 13) timing unit. After our change, the timing unit became 0.96 MHz (3 GHz divided by 12, 13 and 20). Based on this timing unit, we can still obtain a 19.6 MHz timing signal for other utilities. And the streak camera trigger is generated by this 0.96 timing signal. Therefore the laser clock is now a harmonic of the timing unit.

For CTF3, the 3 GHz master clock generates a 250 MHz counter and a 0.96 MHz timing unit. Most of the other trigger or timing signals are based on these two counters. For CALIFES, 3 GHz drives the gun and three accelerating structures. A 1.5 GHz signal for CALIFES laser oscillator is derived from this 3 GHz RF. Details are shown in figure 3.16. For EOSD laser synchronization, the 3 GHz generates a 74.9 MHz for the EOSD laser oscillator locking. The 75 MHz laser RF signal is the 40th sub-harmonic of 3 GHz. The 0.83 Hz streak camera trigger

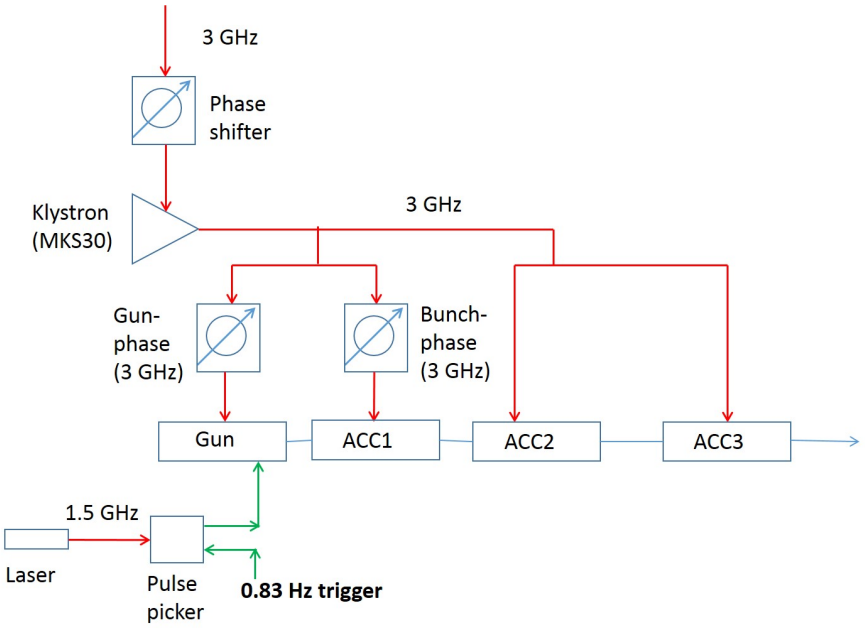

FIGURE 3.16: Phase shifters for CALIFES: The 3 GHz phase shifter before the klystron controls RF phase of the entire CALFIES beam line. Gun: photo-cathode gun. ACC: accelerator cavity.

is generated by the 0.83 Hz general start as a trigger and 0.96 MHz (the 3120th sub-harmonic of 3 GHz) as a counter.

The CALIFES gun and three accelerating structures are driven by 3 GHz. The CALIFES laser is running at 1.5 GHz. But after the pulse picker, the photo inject laser is running at 0.83 Hz (can be up to 5 Hz).

The EOSD bunch profile monitor requires the laser pulse and the electron bunch to pass through the crystal simultaneously. The synchronization between the laser and the electron pulses must be handled with a very good precision, at least of the order of the bunch length. The layout of the timing and synchronization system developed for EOSD is presented in figure 3.17.

A 74.963 MHz RF signal, derived from the main 3 GHz (40th subharmonic) RF system, is provided to lock the repetition rate of the laser oscillator to. A rough ($\sim$100 ps) synchronization is provided by shifting the phase of this RF signal. The precise timing overlap between the e-beam and the laser pulse is then performed using an optical delay line with the ability of 13 fs step increment and 1 ns scanning range. A 0.83 Hz low jitter signal triggers streak camera and the ICCD camera. The ICCD camera can be gated within a 3 ns minimum exposure time.

CALIFES is running with 0.8 Hz-5 Hz repetition rate, in either a single bunch mode or a multi-bunch mode with a pulse train composed of up to 226 bunches.

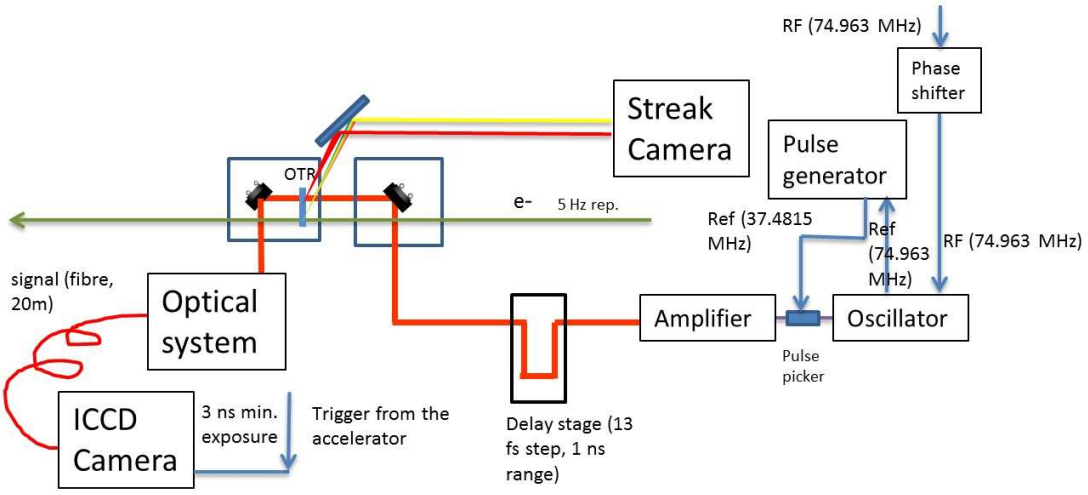

FIGURE 3.17: Timing and synchronization scheme

The experimental tuning of the overlap between the electron bunches and the laser pulses is performed using the high reflectivity OTR screen mentioned previously. OTR photons induced by the particles and laser photons reflected by the OTR screen are sent to a streak camera via a 20 m long optical line. Streak camera thus monitors the arrival time of both laser photons and OTR photons within a few picosecond accuracy.

3.3 Preliminary beam measurements

The timing overlap between the photons and the electrons has been measured preliminary. Figure 3.18 shows both the electron bunch and the laser pulse measured by the streak camera (Hamamatsu femtosecond streak camera C6138). The smaller spot on the pictures corresponds to the laser pulse and the bigger one is the e-bunch. Since it is only used to test the synchronization, the bunch is not compressed, and the laser pulse here is chirped to 3 ps. From these images one can extract the longitudinal profile of both the electron bunch (left peak) and the laser pulse (right peak) as visible on figure 3.18(d). To achieve the laser-bunch synchronization, the optical delay line of the laser was changed in order to shift its arrival time earlier or later than the e-bunch, as shown respectively in figure 3.18(a) and figure 3.18(c). The figure 3.18(b) corresponds to overlapping conditions, which implies the electrons and the laser photons arriving on the OTR screen at the same time. In this condition a maximum peak to peak jitter of 1.2 ps between the two beams was measured over ten consecutive images.

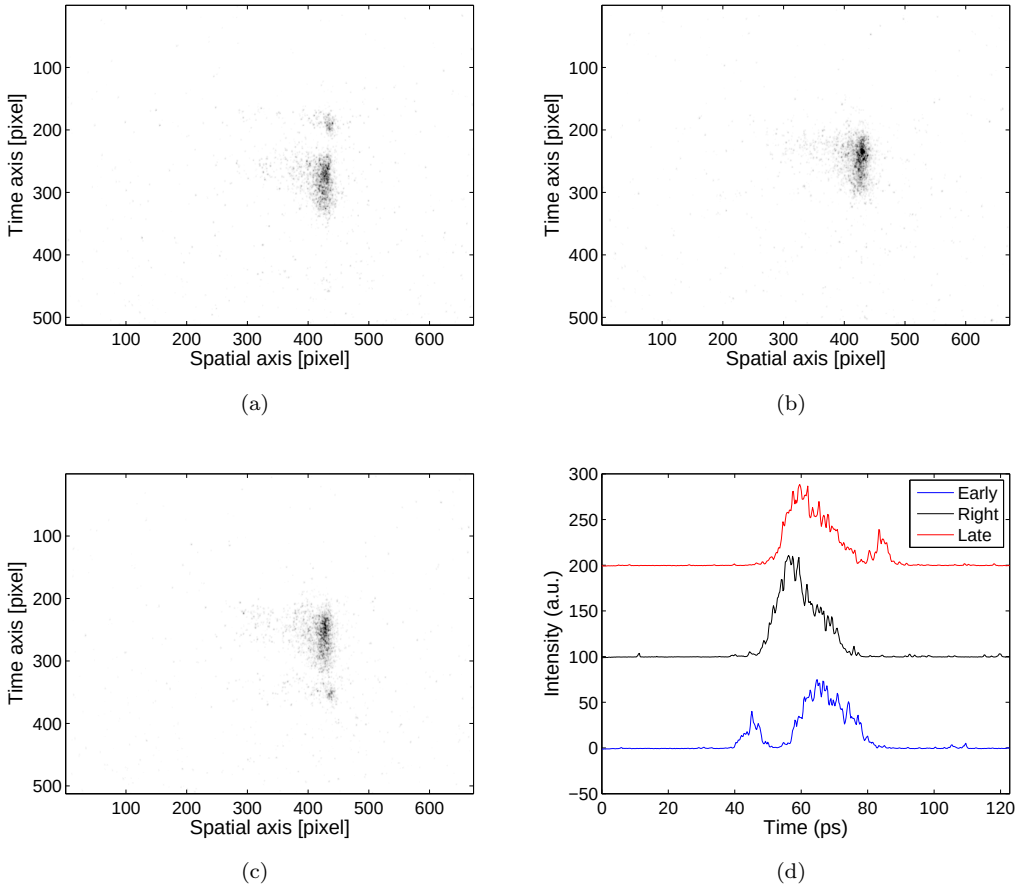

FIGURE 3.18: Timing overlap between E-bunch and laser pulse, measured by the streak camera: (a) Laser on the top; (b) Laser and e-bunch overlap; (c) Laser on the bottom; (d) Profiles.

The CALIFES bunch length is designed to be 1.4 ps long. However, its bunch phase shifter has only 80 degree range and cannot work in bunch compression mode properly at the time of the experiment reported here. Therefore the bunch length could not be compressed to shorter than 6 ps.

In order to check the principle of the EOSD system, a photo multiplier tube (PMT) and an oscilloscope were used. This method works even in the case that the signal to noise ratio is too low for the ICCD camera. Once the bunch and the laser pulse are overlapped in arrival time, the OTR screen in the accelerator can be swapped to EO crystal. A high sensitivity PMT was put in front of the spectrometer. On the oscilloscope, the beam induced EO polarization modulation can be seen and is shown in figure 3.19. In this figure, the oscilloscope was triggered by the low jitter timing signal derived from the RF of the accelerator. The laser pulses are visible as the peaks, which shows one laser pulse, at 87 ns, with a much larger intensity. In the present situation of 0.2 nC bunch charge and

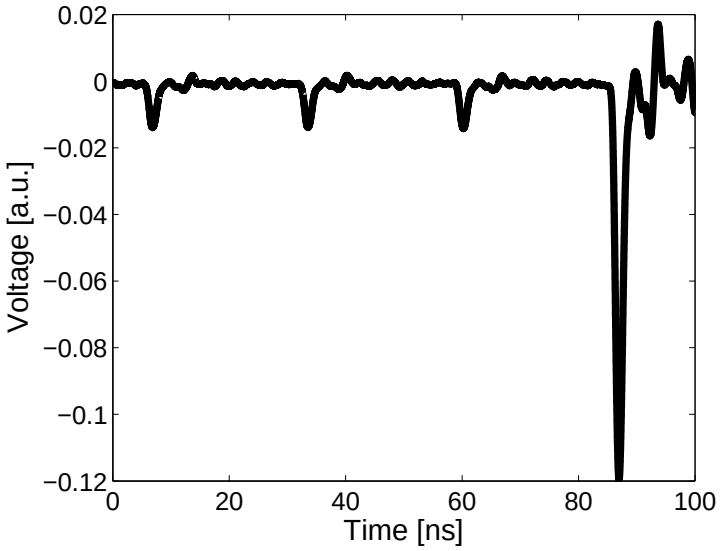

FIGURE 3.19: First EO signal measures by a photomultiplier

7.4 ps bunch length, the EO signal is 6 times larger than the background laser probe without any optimization of the monitor.

Chapter 4

Measurement results from EOSD bunch profile monitor

This chapter presents an analysis of the results from the EOSD bunch profile monitor on CALIFES, including timing calibration, bunch charge dependence, and comparison with streak camera measurements. Finally, the absolute Coulomb field strength are measured. Three methods to retrieve the Coulomb field strength are provided, including a single shot method. At the end of this chapter, the effect of a small half-wave plate offset angle on the bunch length measurement is studied.

4.1 Timing Calibrations by laser spectrum

The bunch profile information is encoded in the probe laser spectrum due to the applied linear relationship. In order to measure the bunch length, a time-wavelength calibration is therefore needed. The time-wavelength relationship can be calibrated by two methods: delay the laser pulse a known amount using an optical delay stage with bunch arriving time fixed, or delay the bunch arrived time by changing CALIFES master RF phase, the scheme of which is shown in figure 3.14, with the laser arrived time fixed. However, care has to be taken on the calibration that the laser spectral profile does not distort the bunch profiles and so also their arriving times.

In the measurements, the EOSD system is set to crossed polarization and the bunches have charge of 0.3 nC. Figure 4.1 shows the measured bunch profiles with delaying the RF phase of the CALIFES master clock. In this way all relative

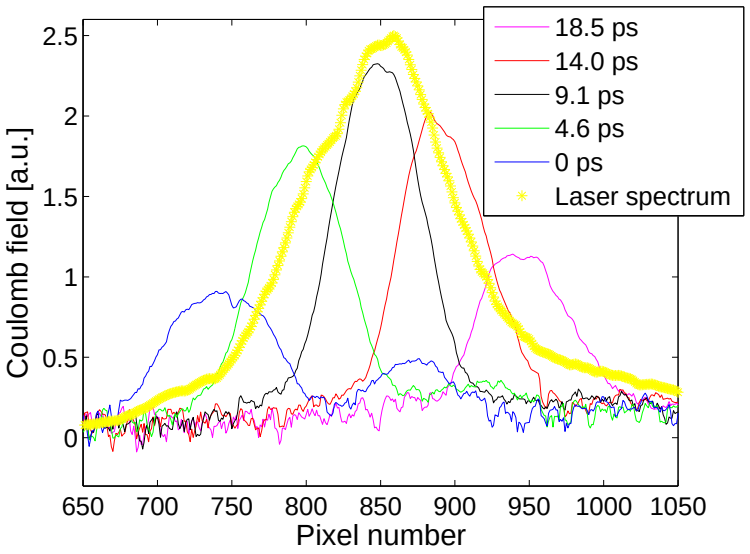

FIGURE 4.1: Bunch arrived time measurements made by delaying the CALIFES RF phase. From left to right, the bunch delay time are from 0 ps to 18.5 ps. The colour curves are the measurements. The yellow curve is the probe laser spectrum.

timing of CALIFES RF signals are kept the same, ensuring the bunch properties are kept the same and only the arrived time is changed. The CALIFES master clock is 3 GHz, therefore a 360° phase change means a 333 ps delay in time and the calibration factor is 0.925 ps per degree.

In figure 4.1, the yellow curve is the input laser spectrum, colour curves are the measured Coulomb fields of bunches with different arriving times. Each profile is 50 shots averaged, baseline subtracted, and has the square root taken (original sign is kept) which transforms intensity to Coulomb field.

The phase delay from 165° to 145° implies the time delay from 0 ps to 18.5 ps, and bunch positions can be found in Table 4.1. The measured bunch lengths vary from 70 pixels to 93 pixels and the bunches close to the edges of the laser spectrum are measured as longer than the ones in the middle. Since bunch profiles should be same under the same settings, this result doesn't show undistorted bunch profiles. As shown in equation 2.83, the EOSD signal is proportional to laser intensity, leading to the profiles on the slope of the laser spectrum being distorted. In particular, the signal on the waist is broadened more. The distortion on the measured profile implies that not only the bunch length but also the bunch arriving time are distorted by the laser spectrum.

To study the impact of this distortion, a calculation using input Gaussian profiles without laser spectrum calibration was performed, the results of which are shown

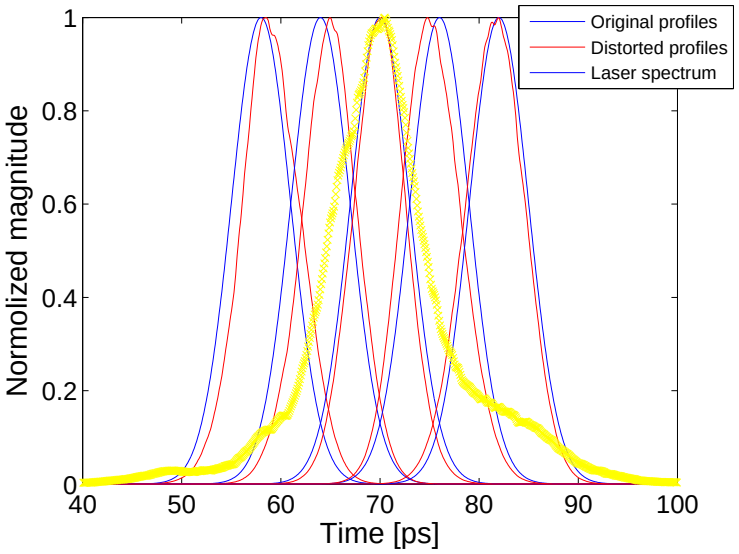

FIGURE 4.2: Calculation result for comparison of original Gaussian profiles and distorted profiles without laser spectrum normalization. Gaussian profiles (simulating original bunches) with 7 ps FWHM and different delay times are shown in blue. The distorted profiles (simulating the measured bunch profiles without laser spectrum calibration) are in red. Laser spectral intensity is shown in yellow.

in figure 4.2. 7 ps FWHM Gaussian bunch profiles are assumed as the blue curves and laser spectrum is shown in yellow. The red curves are the calculated distorted curves simulating the measured Coulomb field profiles. Their field magnitudes are normalized to unit 1. The FWHM of the red profiles are 7.0 ps, 6.5 ps, 6.3 ps, 7.0 ps and 7.1 ps respectively from left to right. Due to the laser spectrum, the measured bunch positions move towards to the center of spectrum comparing to the original bunch positions. The distortion of profiles depend on the slope of laser spectrum. At the center peak of the laser spectrum, the bunch amplitude at center of its profile is enhanced more than its side parts, which leads to a reduction of its bunch length. At the sides where there is a gentle slope of the laser spectrum, one side of the bunch profile is enhanced more than the other, which leads to a profile broadening. At the positions of laser spectrum between the above two, spanning the gentle slope and steep slope, the profiles are performed from broadening to compact.

The profiles can be retrieved by normalising the measured profiles to the laser spectrum, the results of which are shown in figure 4.3. From the figure, the retrieved profiles, in green, are in good agreement with the blue original profiles. All of the positions, lengths and amplitudes are retrieved faithfully.

Therefore, only the spectra intensity calibrated profiles can be used to calibrate

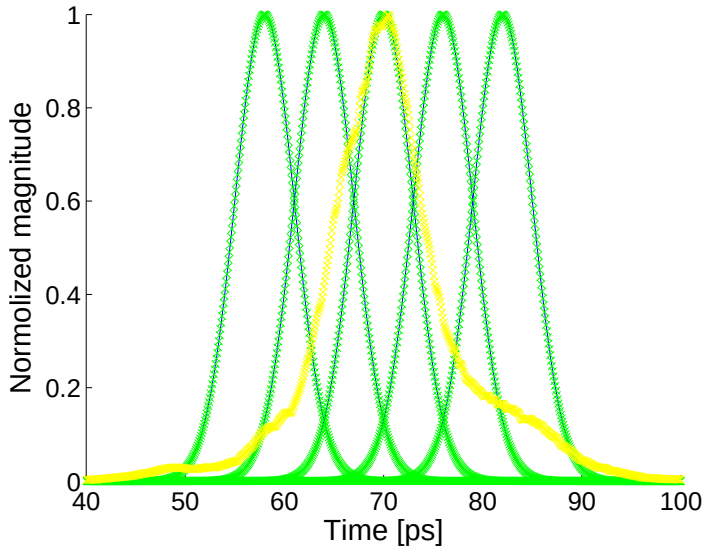

FIGURE 4.3: Calculation result for comparison of original Gaussian profiles and retrieved profiles with laser spectrum calibration. Gaussian profiles (simulating original bunches) with 7 ps FWHM and different delay times are shown in blue. The retrieved profiles are in green. The yellow curve is the laser spectrum.

the time. The laser intensity calibrated bunch profiles are shown in figure 4.4. Again, the yellow curve is the laser spectrum, and the measured profiles with

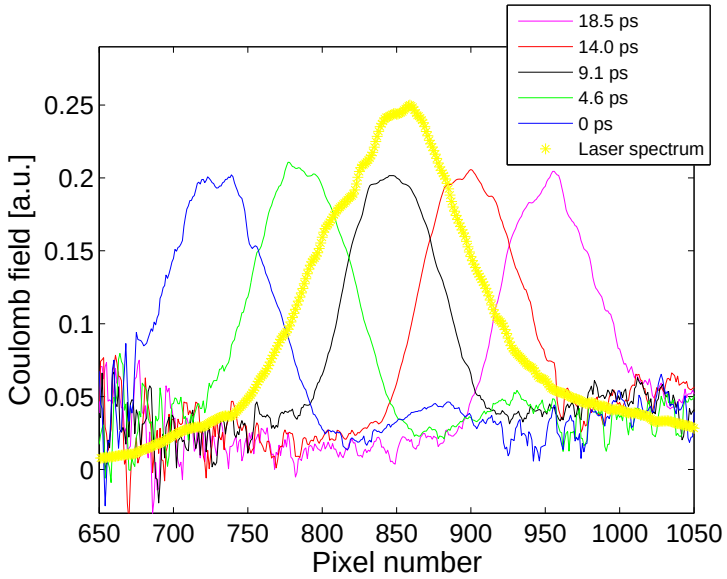

FIGURE 4.4: Bunch arriving time measurements by delaying CALIFES RF phase and calibrated by laser spectrum. From left to right, the bunch delay time are from 0 ps to 18.5 ps. The coloured curves are laser spectrum calibrated profiles, and the yellow curve is the probe laser spectrum

laser spectrum calibration are in colour. Their positions and lengths, obtained from their Gaussian fittings, are shown in table 4.1. The profile amplitudes are

TABLE 4.1: Positions and lengths for non-normalized and normalized bunch profiles with different delay time

Delay time(ps)	0	4.6	9.1	14.0	18.5
Non-normal. peak pixel	743	797	849	892	948
Non-normal. FWHM(pixel)	93	75	72	70	82
Normalized peak pixel	728	786	848	901	955
Normalized FWHM(pixel)	86	83	83	83	77

retrieved almost back to the same value. A ±2.4% amplitude fluctuation is in the 5% bunch charge fluctuation range. The temporal profiles FWHM at the extremes of delay are 86 pixels and 77 pixels, which are slightly different from the middle three at 83 pixels. Since these two profiles are located on the boarder of the laser spectrum, their signal to noise ratio here are worse than for the middle three, which leads to a distortion in the retrieval process.

In order to describe the impact of timing jitter and data averaging, the laser profile S_L and bunch intensity profile P_b are assumed to be ideal Gaussian functions: $S_L = A_L e^{-\frac{t^2}{2\sigma_L^2}}$ and $S_b = A_b e^{-\frac{(t-\mu_i)^2}{2\sigma_b^2}}$, where A_L, A_b are the amplitudes for laser profile and bunch profile respectively, σ_L, σ_b stand for their durations and $\sigma_L \gg \sigma_b$. μ_i is the timing offset on the electron bunch relative to laser pulse. If $\mu_i > 0$, the bunch arriving at the right slope of the laser spectrum. While $\mu_i < 0$ implies the bunch arriving at the left of the slope. To simplify the problem, the jitter timing μ_i is supposed to obey a normal distribution, and thus its probability is $P(\mu_i) = e^{-\frac{\mu_i^2}{2\sigma_j^2}}$, where σ_j is the jitter delay standard deviation. Therefore, the EOSD data profile can be written as $S(t) = S_L(t) \cdot S_b(t, \mu_i) \cdot P(\mu_i)$. For N-shot averaging of the EO signal:

$$\begin{aligned} S_{ave} &= \frac{1}{N}\sum_{i=1}^{N} S(t) \\ &= \frac{1}{N}\sum_{i=1}^{N} [S_L(t) \cdot S_b(t, \mu_i) \cdot P(\mu_i)] \\ &= \frac{A_b S_L(t)}{N}\sum_{i=1}^{N}\left[e^{-\frac{(t-\mu_i)^2}{2\sigma_b^2}} \cdot e^{-\frac{\mu_i^2}{2\sigma_j^2}}\right]. \end{aligned} \tag{4.1}$$

If the number of the data sample is big enough, which is $N \to \infty$, then $\frac{1}{N} \to \Delta\mu \to d\mu$. Thus,

$$
\begin{aligned}
S_{ave} &= A_b S_L(t) \int \left[e^{-\frac{(t-\mu)^2}{2\sigma_b^2}} \cdot e^{-\frac{\mu^2}{2\sigma_j^2}} \right] d\mu \\
&= A_b S_L(t) \cdot \left[e^{-\frac{t^2}{2\sigma_b^2}} * e^{-\frac{t^2}{2\sigma_j^2}} \right] \\
&= S_L(t) \cdot A_b e^{-\frac{t^2}{2\sigma^2}},
\end{aligned}
\tag{4.2}
$$

where the averaged bunch duration $\sigma = \sqrt{\sigma_j^2 + \sigma_b^2}$. The equation 4.2 implies that the distortion on the laser spectrum normalized profiles comes from the timing jitter σ_j and the non-identical nature of each bunch profile. The mean arrival time of the averaged profile has no dependence on the timing jitter if enough samples are collected.

The second method to calibrate the timing is by moving optical delay stage (with 2 μm resolution) to change the laser arrived time. The results without and with laser intensity calibration are shown in figure 4.5(a) and 4.5(b) respectively. 15 delay times, from 0 ps up to 19.53 ps, are recorded, and only five plots of them are shown here. All the data results are shown in figure 4.6. Shortening the laser optical path leads bunch profile moving to right side of the spectrum as shown. Therefore the head of bunch is on left side.

With the laser spectral intensity correction, the timing calibrated by CALFIES phase provides the calibration factor of 0.082 ± 0.003 ps/pixel, while the timing calibrated by optical delay stage provides factor of 0.082 ± 0.001 ps/pixel. The errors here are the standard errors from the time-position fittings. The calibration factor 0.082 ps/pixel with 1.2% error is selected for all of measurements in this thesis. For a 7 ps measured bunch length, the error from the calibration is 84 fs.

There is an interesting small peak at 875 pixel number (12.5 ps) after the main peak of the 0 s time delay profile in figure 4.1. It only appears in the tail of the 0 s time delay profile, because it is just at the position of laser spectrum peak. Otherwise, it is buried in noise and cannot be seen. The second peak cannot be a laser back reflection in crystal, since the crystal is 4 mm thickness and laser refractive index in ZnTe is 2.83 at 780 nm which will cause a 37.7 ps delay. Therefore the small peak should be either a part of the electron bunch, or something else tightly following the bunch Coulomb field. It will be discussed in the Chapter 4.5. The main peak is 4.76 times bigger than the following peak. Therefore, even with a drop in the laser peak power or bunch charge by a factor 4.76, the EO signal can still be measured.

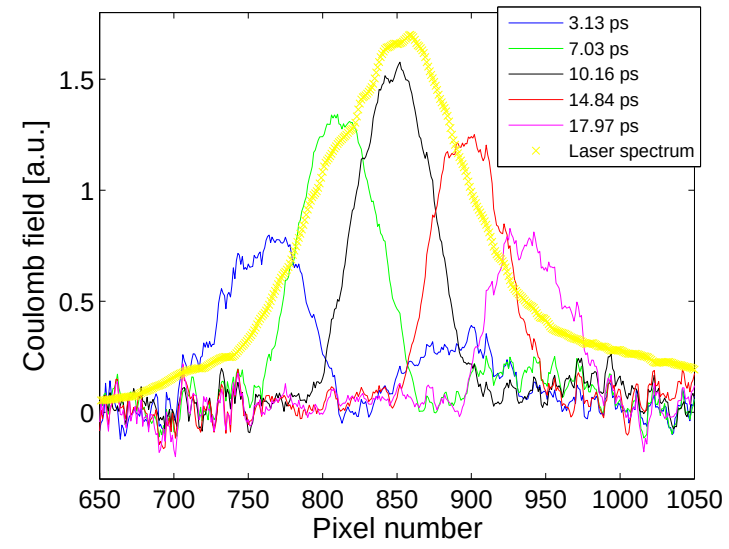

(a)

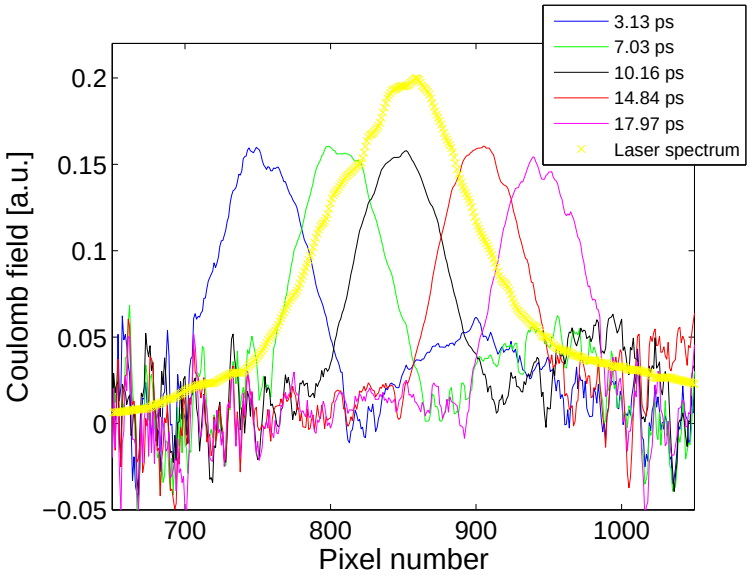

(b)

FIGURE 4.5: Bunch arriving time measurements by delaying translation stage on the laser line. Shortening the laser optical path leads bunch profile moving to right side of the spectrum. From left to right, the delay time are from 3.13 ps to 17.97 ps. The yellow curve is the probe laser spectral intensity. (a) Not normalized by laser spectral intensity; (b) Normalized by laser spectral intensity.

Figure 4.6 shows the comparison of the two calibration methods: time delay induced by translation stage and by CALIFES phase, and the results from with and without laser spectral intensity calibration. The bunch arrival times and lengths are labelled against their own calibrated time delay. Figure 4.6(a) shows the bunch arrival times with the delays. The calibration plots without the laser

spectrum normalization show the beams arriving later because of their calibration factors are 0.092 ± 0.004 ps/pixel and 0.087 ± 0.001 ps/pixel for the beam delay and the laser pulse delay respectively.

The measured bunch lengths are shown in figure 4.6(b). For the delay stage calibrated measurements, the two profiles at 18-19 ps delay time are sitting at the very edge of the laser spectrum, and can't be retrieved properly due to the very low signal to noise ratio. The data at 6 ps delay time has a big error and is not considered in this analysis. The measured bunch (FWHM) is 6.0 ± 0.1 ps with the laser intensity calibration. For the CALIFES phase delayed measurements, the bunch at 18 ps delay time cannot be retrieved properly as well. From 0 ps to 17 ps delay time, the calibrated lengths are 6.8 ± 0.1 ps. The data between 4 ps and 16 ps delay time shows the calibrated bunch lengths are longer than the uncalibrated ones. It implies the Gaussian profile of the laser spectrum squeezes the bunch profile towards its central peak, which means the non-normalized time scaling is smaller than the normalized one. Note that the two calibration methods were performed with different CALIFES operation condition, which leads to the different bunch lengths were measured. The CALIFES phase method provides 90 fs timing resolution and the translation stage provides 13 fs resolution. Since the translation stage is sitting 20 m before the measurement point, an alignment error may be induced in. The laser spot position on the EO crystal may change slightly when the translation stage changes.

Based on figure 4.6, the profiles in the delay time range from 0 to 16 ps can be well retrieved by laser spectrum. Therefore the effective measurement window is around 58 ps to 74 ps in duration.

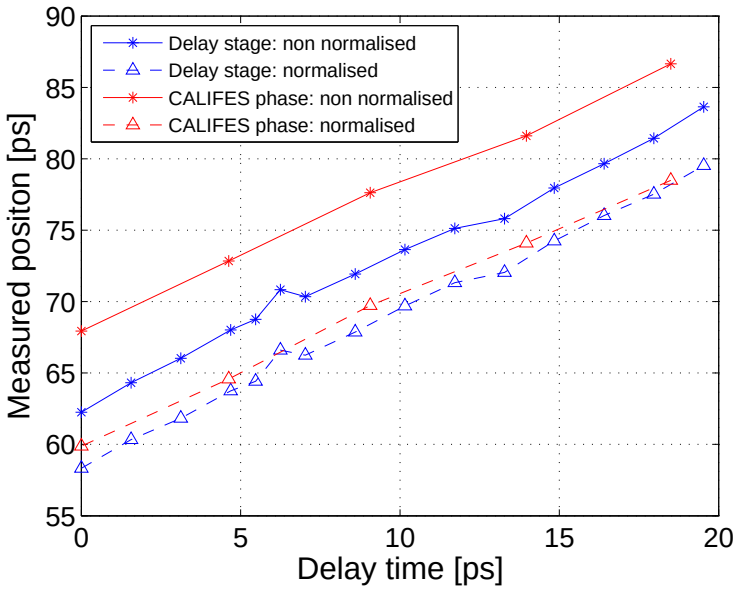

(a)

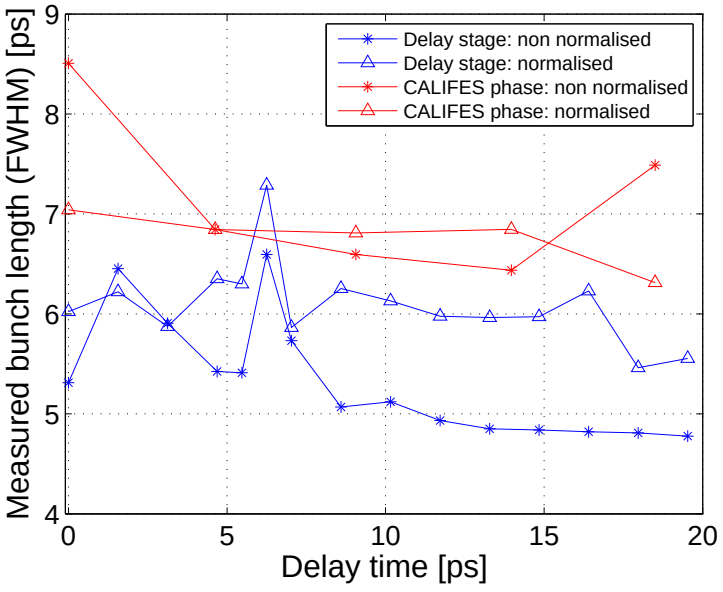

(b)

FIGURE 4.6: Comparison of the two temporal calibration methods. The blue and red curves show the results from delay stage method and from the CALIFES phase method respectively. The non-normalised and normalised results are shown by star mark and triangle mark respectively. (a) Measured bunch arriving time with and without laser spectrum calibration (b) Measured bunch lengths with and without laser spectrum calibration.

4.2 Bunch profile measurement with bunch charges

Bunch charge plays an important role on Coulomb field strength. The bunch charge on CALIFES is measured by a wall current bunch charge monitor just after its photo gun. Here, measured bunch profiles with three bunch charges of 0.17 nC, 0.32 nC and 0.71 nC are shown in figure 4.7.

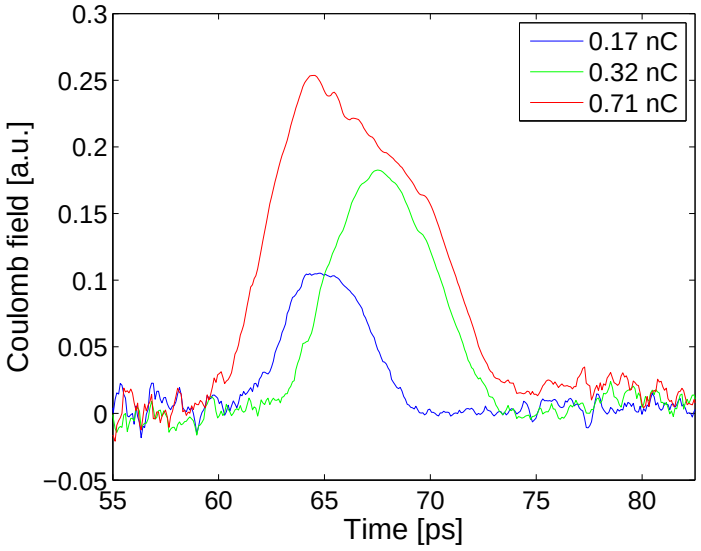

FIGURE 4.7: Bunch profile measurements with three bunch charges: 0.17 nC, 0.32 nC and 0.71 nC (from low to high)

All the three profiles were averaged over 50 shots and processed with the same method as described in the previous sub-section. The amplitude of the three profiles are relative to each other, although their field values are not calibrated to absolute values. The arrival times have more than 1 ps difference among these three because the CALIFES RF phase was changed during the three measurements. To study the relation between bunch charge and measured EOSD value, regardless of its profile, the profiles are integrated over time. Note that based on equation 2.4, bunch Coulomb field is related to bunch longitudinal charge density: $E_{Coul}(t) = E_{e0}(t) * \rho(t)$. If the Coulomb field is integrated over the pulse duration on both sides of the equation and apply a rewritten, then the integration of Coulomb field is proportional to bunch total charge Q: $\int E_{Coul}(t)dt = \int E_{e0}(t)\,dt \cdot \int \rho(t)dt \equiv \frac{Q}{e_0} \cdot \int E_{e0}(t)\,dt$[1], where e_0 is the charge of one electron. The integration result is independent of longitudinal bunch duration. Based on the above equation, $\int E_{Coul}(t)dt/Q \equiv \int E_{e0}(t)\,dt/e_0 \equiv Constant$ are expected. Since lack of the field strength calibration, the relative values from these three bunch profile measurements are discussed here. The measured three

[1] $\int (f(t) * g(t))dt = \int f(t)dt \cdot \int g(t)dt$.

profiles are integrated over time and normalised by their bunch charge. If the result for the 0.17 nC bunch is considered as V_{e0} with 4% random error calculated from 50 shots, then the results for the 0.32 nC bunch and 0.71 nC bunch are $1.02V_{e0}$ with 4% error, and $0.93V_{e0}$ with 2% error respectively. The results here show the linear dependence between the $\int E_{Coul}(t)dt$ term and bunch charge. Therefore once the Coulomb field strength and the beam position are known, the bunch charge information may be retrieved from the bunch profile measurement. The methods to retrieve Coulomb field strength are discussed in section 4.5.

The reason for the slightly lower value on 0.71 nC may because of bad transmission for high charge bunch on CALIFES which is designed for bunch charge no more than 0.6 nC. The bunch charge monitor is installed just after the photo injector of CALIFES, and the EO bunch profile monitor is installed 10 meters after. Part of the bunch maybe lost on the way between photo gun and the EO crystal. For example, space charge pushes the bunch longer, however only the core part of the bunch can be accelerated effectively, which leads to part of the charge being lost. Another possible reason is the bunch with 0.71 nC charge has a long tail. Since the charge in the tail is low so that the tail signal is buried in the noise, the measured data cannot show the whole charge information. With bunch charge increasing, space charge plays a role on profile broadening. For the three measurements from low charge to high, the measured FWHM of profiles are 5.3 ± 0.1 ps, 6.4 ± 0.1 ps and 9.0 ± 0.1 ps respectively.

4.3 Comparison with streak camera measurements

For cross checking the EO bunch length measurements are compared with streak camera measurements under four CALIFES RF phase settings.

The streak camera measurements are based on the OTR transfer line of the EOSD system as shown in figure 3.17. This OTR line is designed for checking the synchronization of laser photons and the bunch induced OTR photons by streak camera, which is not optimized for bunch length measurement. Since there is a low signal to noise ratio (SNR) on the streak camera measurements, when working on its 50 ps sweeping window, no bandwidth filter are used on the OTR photons line and the entrance slit were widened to 2 mm in order to gain more photons, at the price of lower timing resolution. Therefore the streak camera was not working on its best resolution condition.

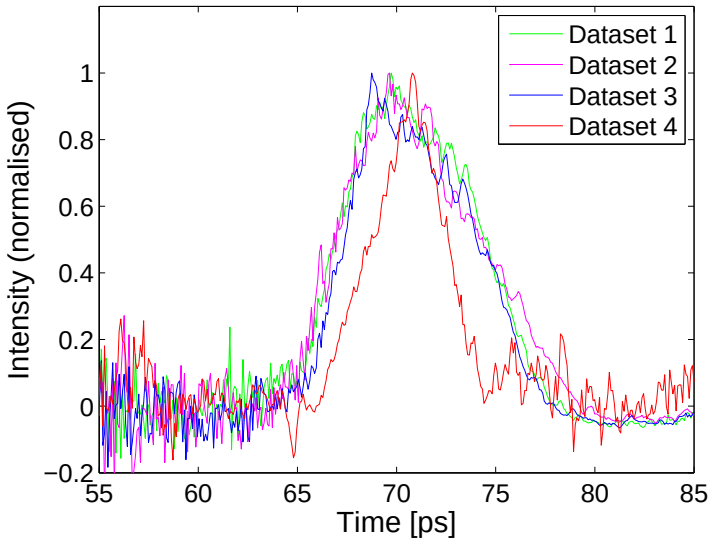

(a)

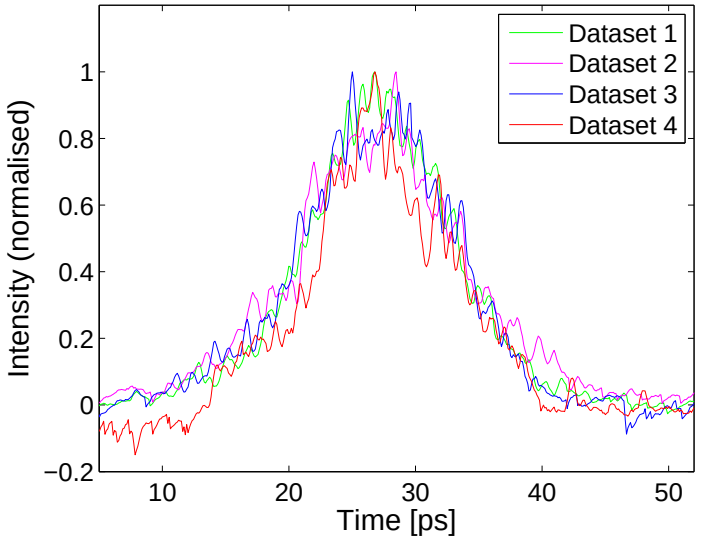

(b)

FIGURE 4.8: EOSD and streak camera measurements comparison under the 4 CALIFES RF phase settings: (a) EOSD measurements; (b) Streak camera measurements.

During the EOSD measurments, the half-wave plate was set to +5° in order to improve signal to noise ratio. This half-wave plate offset induces a factor of 1.13 between the measured bunch length and the original bunch length, since the EOSD measures both the linear Coulomb field term and its quadratic term. The factor number comes from numerical calculation, and this effect on the bunch length will be discussed in subsection 4.6. To get the bunch information, the measured signals are background and baseline subtracted, and their intensities are normalised by the laser spectrum. Each plot in figure 4.8(a) is the average over 50 shots and the plots are averaged by 20 shots in figure 4.8(b). All plots are also 5 point smoothed and centered based on Gaussian fits. For the 0.35 nC bunch charge and a single shot measurement, the signal to noise ratio of EO measurement is 54, which is better than streak camera's signal to noise ratio of 42. In figure 4.8(a), the noise level on the earlier shoulder of the profiles is higher than the later shoulder, which is induced by the laser spectrum normalization. The timing jitter shown from the measurements using the EOSD system is less than 1 ps, due to the laser synchronization, which is much smaller than the internal jitter of the streak camera (approximately 30 ps).

From dataset 1 to dataset 4, the calibrated EO measured bunch lengths are 10.2 ± 0.2 ps, 10.4 ± 0.2 ps, 9.3 ± 0.2 and 5.4 ± 0.2 ps FWHM. The estimated error here includes $\pm 0.1°$ half-wave plate angle error and a random error. The slit size plays an important role on the resolution of the streak camera. The calibrated streak camera measured bunch lengths by 2 mm slit size are 8.5 ± 0.5 ps, 10.2 ± 0.5 ps, 9.0 ± 0.5 ps and 6.9 ± 0.5 ps FWHM for the four sets of data respectively [17]. For the dataset 4, 5.4 ps measured by EO monitor and 6.9 ps measured by streak camera. This big difference may be because the streak camera is already at its resolution limit under this operation condition. Under the setting of dataset 4, the bunches have lower intensity and shorter bunch length which are shown in both measurement results.

4.4 Measurement with half-wave plate angles

As shown in equation 2.76, for the cross polarization setup the measured signal is composed of the sum of three terms: a background term (I_1) which is proportional to laser intensity, a linear term (I_2) which is proportional to Coulomb field, and a quadratic term (I_3) which is proportional to the Coulomb field square (intensity). If the setup is an ideal crossed polarization, the result only follows the quadratic term. However, if the setup does not work in an ideal condition, background leakage by rotation of the $\lambda/2$ wave plate for instance, the result should contain all the three terms. In this section, a background is leaked in the EOSD measurement by rotation of $\lambda/2$ wave plate. This allows the absolute value of the Coulomb field to be determined, and also for the polarity of the field to be observed. While Coulomb field alone will be uni-polar, wakefields following the bunch will potentially have the opposite polarity to the Coulomb field. All the measurements are taken in the condition of 0.3 nC bunch charge, 200 MeV beam energy and observed at 2 mm away from the bunches.

In order to extract the absolute value of a Coulomb field, the key is to remove the quadratic term or distinguish the linear term and quadratic term, since the background term can be removed easily by background subtraction. Also based on equation 2.76, for a setting of $\lambda/2$ wave plate angle ϕ, $\lambda/4$ wave plate angle $\alpha = 0$ and EO crystal angle $\theta = \pi/4$, the measured signal, composed of the three terms, are shown as:

$$\begin{aligned} I(\phi) &= I_1(\phi) + I_2(\phi) + I_3(\phi), \\ I_1(\phi) &= I_{laser} \cdot \sin^2(2\phi), \\ I_2(\phi) &= -I_{laser} \cdot A_2(\tau) \cdot \sin(4\phi), \\ I_3(\phi) &= I_{laser} \cdot A_3(\tau) \cdot 2\cos^2(2\phi), \end{aligned} \tag{4.3}$$

where $I_{laser} = \frac{\epsilon_0 c}{2} |E_{opt}(\omega)|^2$, and:

$$\begin{aligned} A_2(\tau) &= \frac{z\omega}{cn}\sqrt{\frac{\pi}{\beta}}\left[E^{eff}_{Coul}(\tau + t_0) * \cos\left(\frac{\tau^2}{4\beta} - \frac{\pi}{4}\right)\right], \\ A_3(\tau) &= \left(\frac{z\omega}{cn}\right)^2 \frac{\pi}{2\beta}\left|E^{eff}_{Coul}(\tau + t_0) * e^{\left(\frac{i\tau^2}{4\beta} - \frac{i\pi}{4}\right)}\right|^2, \end{aligned} \tag{4.4}$$

where $A_2(\tau), A_3(\tau)$ are independent of $\lambda/2$ wave plate angle, being determined by the Coulomb field. An example of the signal behaviours where all three terms of equation 4.3 are present in the measurement is given in figure 4.9.

A laser pulse centred at 787 nm, with 130 fs FWHM initial duration chirped to 13.8 ps FWHM is defined here in order to simulate the real laser pulse in the calculation. The time duration for a Gaussian profile is described by its Full Width at Half Maximum (FWHM) in the following, except indicated specially. The Coulomb field is supposed to have a 6 ps duration and an ideal Gaussian longitudinal profile. The nonlinear crystal is 4 mm thickness ZnTe. Figure 4.9 shows the calculated and measured results based on these definitions with $\lambda/2$ wave plate set to $-3.7°$. The blue curve in 4.9(a) is the total output signal and the red curve shows the leaked background without Coulomb field applied, which is described by the background term I_1. Figure 4.9(b) shows the background subtracted result (green curve) which equals the sum of the linear (red curve) and the quadratic term (blue curve). In this condition, the linear term is negative and proportional to the Coulomb field. I_3 is proportional to the Coulomb field intensity and is always positive. Note that the second term I_2 can be positive if the $\lambda/2$ wave plate has a positive angle in this setup. Therefore, the central peak of the total signal comes from the peak of the quadratic term, and the two valleys beside it mainly come from the linear term. The quadratic term is narrower than the linear term since related to Coulomb field square. The blue curve in figure 4.9(c) shows the measured total profile, and red curve is the laser background at this $\lambda/2$ wave plate angle. Figure 4.9(d) shows background subtracted profile, and its intensity is normalized by laser spectrum in order to prevent distortion by the imperfect Gaussian profile of laser spectrum. Therefore its profile is independent of the intensity of the probe laser spectrum.

Comparing with the calculated results, a slightly asymmetric structure can be found in the measured signals, especially in the background removed signals. This asymmetry is induced by the phase matching in the crystal. The phase matching efficiency, between the THz pulse and the laser pulse, depends on wavelength as shown in equation 2.44. Without this effect, the signal is symmetric as shown in the inserted figure in figure 4.9(b).

Figure 4.10 shows the calculation (4.10(c)) and measurement (4.10(b)) results with $\lambda/2$ wave plate angle at $0°$, $\pm 1.2°$, $\pm 2.5°$ and $\pm 3.7°$. When a $\lambda/2$ wave plate is turned toward to $0°$ which is an ideal crossed polarization, the quadratic term grows and plays the main role, while the linear term becomes weaker. From zero $\lambda/2$ wave plate angle to positive angles, the linear term becomes positive and grows with the quadratic term. For the measured signals at inverse $\lambda/2$ wave plate angles, the absolute values of each term are equal to those at the respective original angles, but the total signals are different. As shown in the figure, the measured profiles fit the calculation very well. In the measurement,

the bunch was not perfectly centered at the peak of the laser pulse, as shown in figure 4.10(a). From negative angle to positive, the measured signals shift to longer wavelengths. Fortunately this effect can be removed by normalizing the signal using laser spectrum intensity, and mathematically shifting them back to their center. Since the complex profiles are not suitable for Gaussian fitting, the standard of center is not defined by their top peak, but defined by zero crossings after the main peak as shown in figure 4.10(b) at the 19 ps position. After the shifting, the absolute wavelength as the x-axis in the figures is meaningless, and is replaced by relative timing scale in ps.

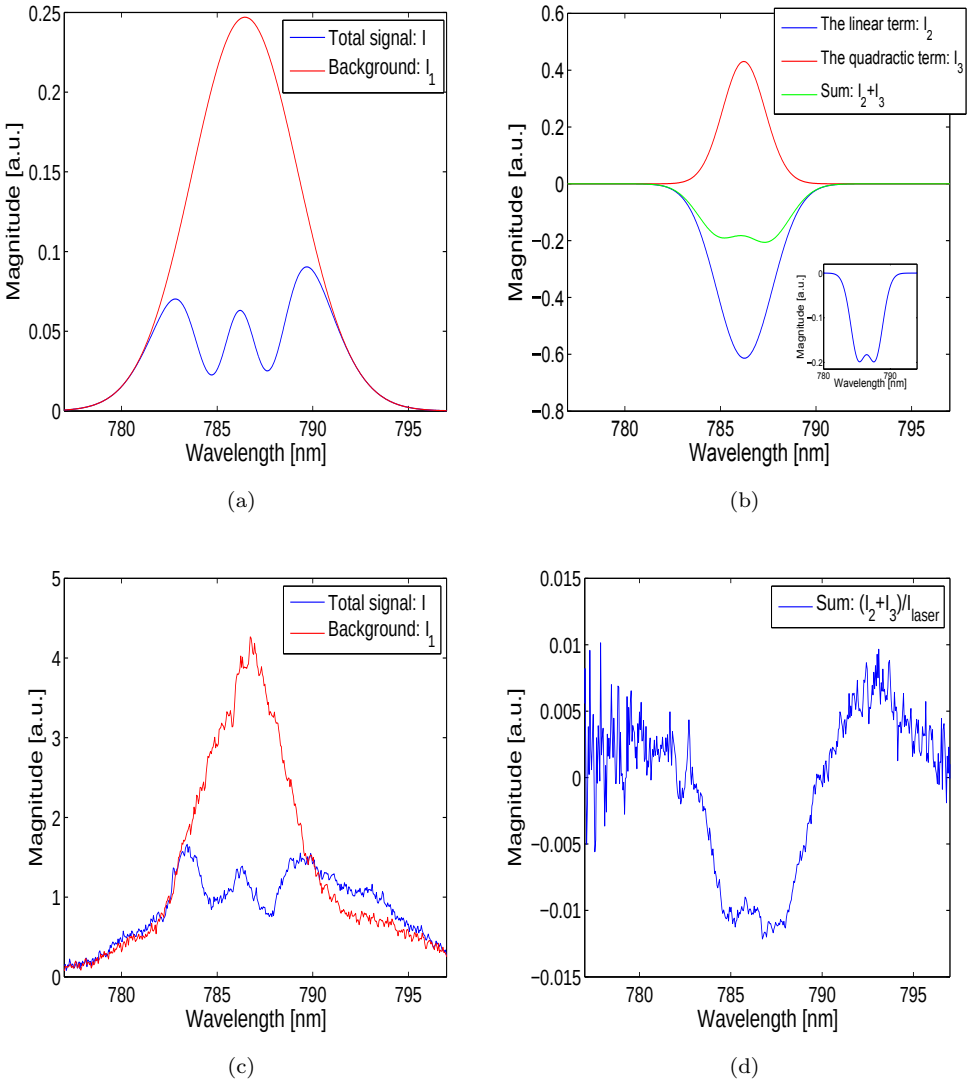

FIGURE 4.9: Calculated and measured results for $\lambda/2$ wave plate at $-3.7°$: (a) Calculated total signal and background; (b) Calculated background removed signal from the total signal. The background removed signal is the sum of the linear term and the quadratic term. The insert figure shows the background removed signal without phase mismatching effect; (c) Measured total signal and background; (d) Measured background removed signal from the total signal.

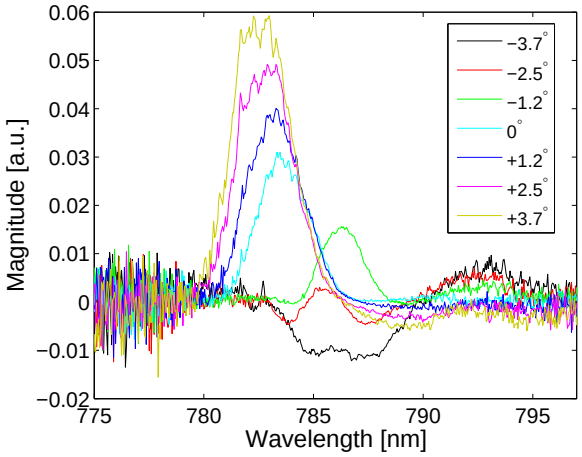

(a)

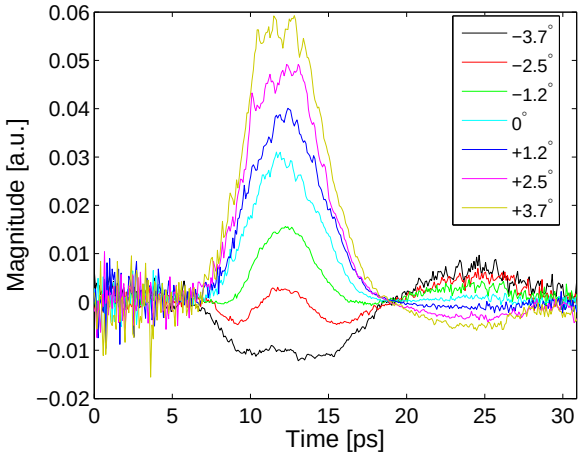

(b)

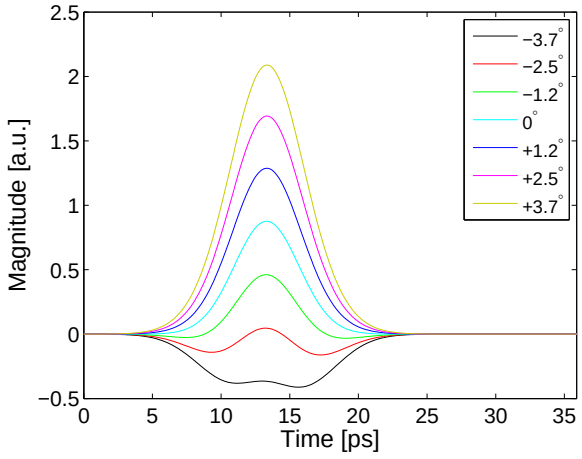

(c)

FIGURE 4.10: Calculated and measured results for $\lambda/2$ wave plate between $\pm 3.7°$: (a) Measured background removed and laser spectrum normalised signal; (b) Measured background removed and laser spectrum normalised signal (shifted); (c) Calculated background removed and laser spectrum normalised signal for 6 ps Gaussian bunch.

4.5 Absolute value of the Coulomb field

In order to extract the absolute values of A_2 and A_3 from equation 4.3, the laser intensity value is needed. In fact, any laser intensity measured on an ICCD camera is a relative value, and needs to be calibrated in order to determine the absolute electric field strength in V/m. The relationship between the relative intensity I_r and absolute intensity I_{abs} can be expressed by: $I_r = I_{abs} \cdot \kappa$, where the factor κ stands for the ICCD camera conversion efficiency. Since the ICCD camera responds linearly with light intensity, the calibration factor is the same for all measurements. Therefore, equation 4.3 can describe for both absolute intensity and relative intensity. Further more, once the measured signals are calibrated by relative input laser intensity, the results $I(\phi)/I_{laser}$ are independent of laser intensity. In the following, I demotes the measured uncalibrated intensity, unless specifically indicated otherwise.

A background signal $I_1(\phi = -22.8°)$, measured with $\lambda/2$ wave plate angle at $-22.8°$, is selected to calculate the full input laser intensity. Then the full laser intensity can be obtained by: $I_{laser} = I_1(\phi = 22.8°)/[\sin^2(2 \times 22.8°)]$. This intensity I_{laser} can be used to calibrate all other measured signals.

Coming back to equation 4.3, the measured and calculated maximum intensity of background $I_1^{max.}(\phi)$ are shown in figure 4.11 with $\lambda/2$ wave plate orientation between $\pm 3.7°$. The plots are calibrated by input laser intensity, and it can be expressed by: $I_1^{max.}(\phi)/I_{laser} = \sin^2(2\phi)$. The error bar shows standard error from 50 shots averaging at each data point. The standard error is defined as:

$$Std(x) = \left[\frac{1}{n(n-1)} \sum_{i=1}^{n} (x_i - \overline{x})^2 \right]^{1/2}, \tag{4.5}$$

where x_i is the analysis data with data sample number n and mean value $\overline{x}$.

From the measured data presented in figure 4.11, the uncertainties in $\lambda/2$ wave plate angles can be calculated. It shows the angles have $\pm 0.1°$ error consistent with specifications on the motor controlled rotation stage. The $0°$ $\lambda/2$ wave plate angle is defined by the $\lambda/2$ wave plate angle at the best extinction position. Since the laser intensity is buried in the noise at this condition, the $0°$ may have a systematic error. The $\pm 0.1°$ $\lambda/2$ wave plate angle error leads to 1.5% error in bunch length measurement, which implies 0.09 ps error for a 6 ps bunch. It also leads to 4% profile amplitude error in Coulomb field strength measurements, which implies 0.05 MV/m error for a 1.3 MV/m field.

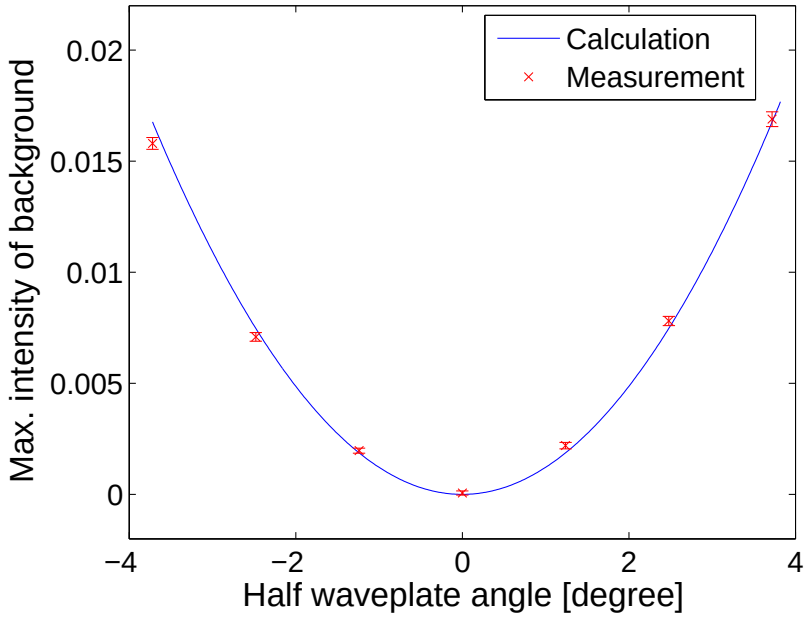

FIGURE 4.11: Calculation and measured maximum intensity of background with $\lambda/2$ wave plate orientation between $\pm 3.7°$

In order to extract its absolute value from measurements of A_2 and A_3, the Coulomb field can be obtained by:

$$\begin{aligned} E^a_{Coul}(\tau + t_0) &= E_{Coul}(\tau + t_0) * \cos\left(\frac{\tau^2}{4\beta} - \frac{\pi}{4}\right) \\ &= A_2 / \left(\frac{z\omega}{cn}\sqrt{\frac{\pi}{\beta}} \cdot \chi^2 \cdot \xi\right) \\ &\approx E_{Coul}(\tau + t_0), \end{aligned} \tag{4.6}$$

$$\begin{aligned} E^b_{Coul}(\tau + t_0) &= \left| E_{Coul}(\tau + t_0) * e^{\left(\frac{i\tau^2}{4\beta} - \frac{i\pi}{4}\right)} \right| \\ &= \sqrt{A_3} / \left(\frac{z\omega}{cn}\sqrt{\frac{\pi}{2\beta}} \cdot \chi^{(2)} \cdot \xi\right) \\ &\approx \left| E_{Coul}(\tau + t_0) \right|, \end{aligned} \tag{4.7}$$

where ξ is the phase matching function, and $\chi^{(2)}$ is the second-order nonlinear optical susceptibility. They come from $E^{eff}_{Coul}(\tau + t_0) = E_{Coul}(\tau + t_0) \cdot \xi \cdot \chi^{(2)}$ as shown in equation 2.47. The retrieved signal $E^a_{Coul}(\tau + t_0)$ is a convolution of the absolute Coulomb field and a cosine term. For 6 ps long bunches within this measurement condition, $E^a_{Coul}(\tau + t_0)$ is a good approximation for the real Coulomb field. It is the same for $E^b_{Coul}(\tau + t_0)$, which is a good approximation for the Coulomb field's absolute value. The approximation of the convolutions in equation 4.6, 4.7 reducing to convolutions with a δ-function is described in

Section 2.4.4.

The follow considers three procedures to extract Coulomb field information from the measured data with varying wave plate angles.

4.5.1 Method by Least-squares fitting

Based on the equation 4.3, the background removed signal, which is the measured optical intensity in presence of an electron bunch minus the intensity without electron bunch, can be written as:

$$\begin{aligned} I_{23}(\phi) &\equiv I(\phi) - I_1(\phi) \\ &= I_{laser} \cdot \left[-A_2 \cdot \sin(4\phi) + A_3 \cdot 2\cos^2(2\phi) + A_{res} \right]. \end{aligned} \tag{4.8}$$

A_{res} is the residual background which can not be removed from $I(\phi)$, introducing a systematic error. The absolute value of A_2 and A_3 can be obtained by normalizing $I_{23}(\phi)$ using I_{laser}, then the intensity calibration factor ϵ is cancelled from the division and the resultant $A(\phi)$ is independent of the input laser intensity:

$$\begin{aligned} A(\phi) &= \frac{I_{23}(\phi)}{I_{laser}} \\ &= -A_2 \cdot \sin(4\phi) + A_3 \cdot 2\cos^2(2\phi) + A_{res} \\ &\approx -4A_2 \cdot \phi + 2A_3 + A_{res}, \end{aligned} \tag{4.9}$$

where it is assumed $\phi \ll 1$ ($\phi \approx 7 \times 10^{-2}$ rad in the examples that follow). For the small angle condition, the intensity linearly depends on $\lambda/2$ wave plate angle, and therefore a simple linear least-squares fitting can be applied, as shown in figure 4.12.

Figure 4.12 shows these measured peak values of the data in figure 4.10(b) at 12.65 ps (787 nm) as a function of the $\lambda/2$ wave plate angles, and a least squares fitting of the data. The error bars show standard error from 50 shots averaging at each data point. The fitting results are: $A_2 = (13.1 \pm 1.24) \times 10^{-2}$, $A_3 = (13.6 \pm 1.1) \times 10^{-3}$.

The retrieved Coulomb field strength from A_2 is 1.20 ± 0.20 MV/m, and from A_3 is 1.37 ± 0.10 MV/m. The uncertainty for A_2 and A_3 is calculated based on 95% confident interval (2σ range).

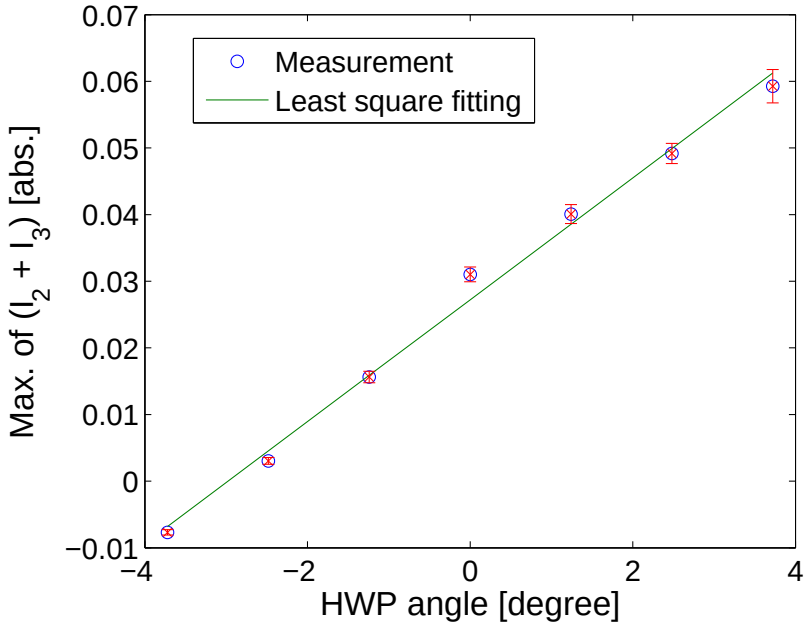

FIGURE 4.12: Linear least-squares fitting with $\lambda/2$ wave plate orientation between $\pm 3.7°$

Based on equation 4.9, the second term of Taylor series for $\sin(4\phi)$ and $\cos^2(2\phi)$ can also be applied, and obtain: $A(\phi) \approx -4A_2 \cdot \phi + 2A_3 + A_{res} - 8A_3\phi^2 + \frac{32}{3}A_2\phi^3$. The last two terms have a value of less than 5×10^{-4}, and can be neglected. The linear term of Taylor expansion of the trigonometric functions can be seen as a valid approximation at this THz strength level and half-wave plate angle range.

For each probe wavelength, corresponding to a particular time within the bunch, a least-square fitting to signal value can be applied and A_2, A_3, at that wavelength, can be obtained. This allows a temporal profile to be evaluated. Taking the data shown in figure 4.10(b), and performing least-square evaluation for A_2 and A_3 as a function of wavelength, the Coulomb field value at each wavelength is obtained and the retrieved Coulomb field profile is shown in figure 4.13. The blue curves in the figures are the retrieved Coulomb field from the linear term A_2 and the quadratic term A_3 at each wavelength. The red curves and green curves are the upper bound and lower bound in each figure respectively. The bounds are determined by the fitting results for A_2 and A_3, based on 95% confidence interval which are within 2σ range. The Coulomb field value calculated from A_3 is slightly higher than it from A_2. This is attributed to the resident background A_{res} can not be removed and contributes as shown in equation 4.9.

The least-squares fitting method uses the whole seven data sets from $-3.7°$ to $+3.7°$ to calculate the Coulomb field. It gives the best result which fits all data.

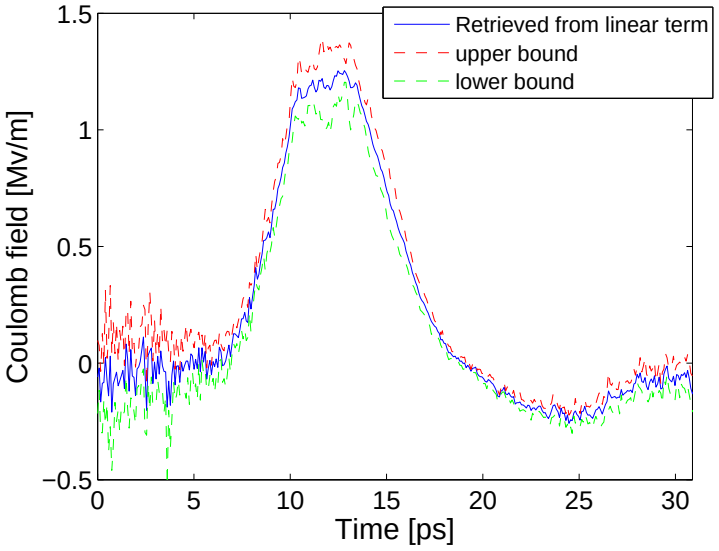

(a)

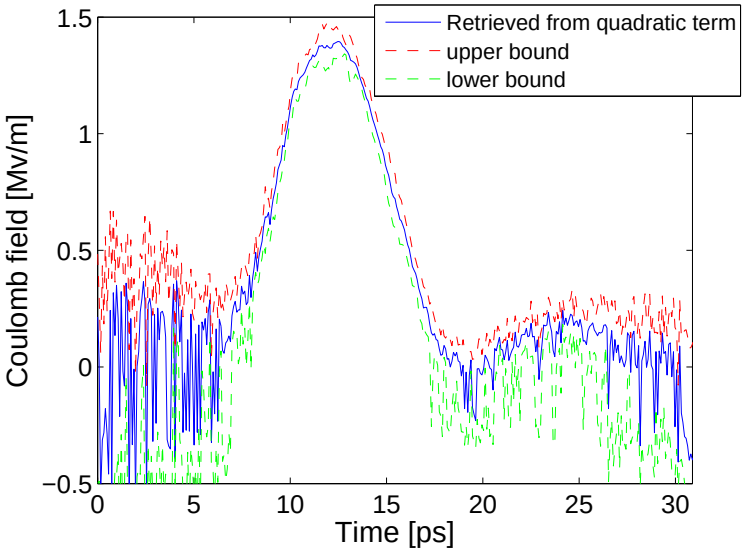

(b)

FIGURE 4.13: Retrieved Coulomb field from the linear term and quadratic term (in blue), the 95% confidence intervals determined bounds are shown in red (upper) and green (lower): (a) Retrieved Coulomb field from the linear term; (b) Retrieved Coulomb field from the quadratic term;

From 20 ps to 30 ps, there is a small bump following the main peak in figure 4.13(b). This bump can be easily mistaken as a bunch structure in the tail within one electron bunch in the crossed polarization detection. However, this bump comes from the negative part of the retrieved Coulomb field in figure 4.13(a), since the cross polarization detection measures the Coulomb field square. In this measurement condition, the Coulomb field should always be positive. Therefore, the measured negative part may be the wakefield of the bunch. The bunch wakefield is known to be observable through EO techniques, and has been experimental measured[9][40][29].

4.5.2 Method by two-shot measurement

The previous method of retrieving the absolute Coulomb field requires many data points at different wave plate angles, something which may not always be possible or desirable to do. Here an evaluation of the Coulomb field from a single pair of observations is discussed. This method can obtain the Coulomb field from a two-shot measurement with $\lambda/2$ wave plate at symmetry angles, or a single-shot measurement that the probe is split into two and measures at two different half-wave plate settings. Equation 4.3 shows that for angles of $\lambda/2$ wave plate at $\pm\phi$ the background and quadratic terms are the same but the linear terms are opposite numbers:

$$I_{23}(\phi) = I_{laser} \times \left[-A_2 \cdot \sin(4\phi) + A_3 \cdot 2\cos^2(2\phi) + A_{res}\right],$$
$$I_{23}(-\phi) = I_{laser} \times \left[A_2 \cdot \sin(4\phi) + A_3 \cdot 2\cos^2(2\phi) + A'_{res}\right].$$

Therefore, with the definition of equation 4.8, the linear and quadratic term can be extracted by:

$$A_2 = \left[\frac{I_{23}(-\phi) - I_{23}(\phi)}{I_{laser}} + (A'_{res} - A_{res})\right] \cdot \frac{1}{2\sin(4\phi)}, \tag{4.10}$$

$$A_3 = \left[\frac{I_{23}(-\phi) + I_{23}(\phi)}{I_{laser}} + (A'_{res} + A_{res})\right] \cdot \frac{1}{4\cos^2(2\phi)}. \tag{4.11}$$

Applying this method to the measured data with pairs of $\lambda/2$ wave plate angles at $\pm 3.7°$, $\pm 2.5°$ and $\pm 1.24°$, the Coulomb field can be retrieved in the same way of equation 4.6 and 4.7. Results of such an evaluation are shown in figure 4.14. Note the signal intensities are all calibrated by full laser intensity. The retrieved maximum values of Coulomb field from the linear term are 1.36 ± 0.26 MV/m, 1.30 ± 0.16 MV/m and 1.28 ± 0.15 MV/m for the three angle pairs, and the retrieved maximum values from the quadratic terms are 1.39 ± 0.12 MV/m, 1.38 ± 0.12 MV/m and 1.32 ± 0.13 MV/m.

This method assumes that the $\lambda/2$ wave plate angles are set sufficiently close to $\pm\phi$ that the linear term or the quadratic term can be cancelled completely. The error estimate in the above stated field strengths includes a potential $0.1°$ $\lambda/2$ wave plate angle error. For the background uncertainty, the difference and sum of the residual A_{res} and A'_{res} are included in A_2 and A_3 respectively. In addition,

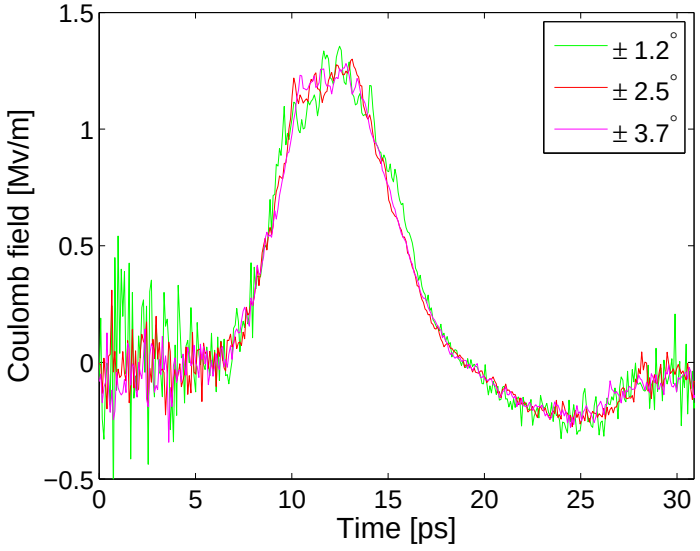

(a)

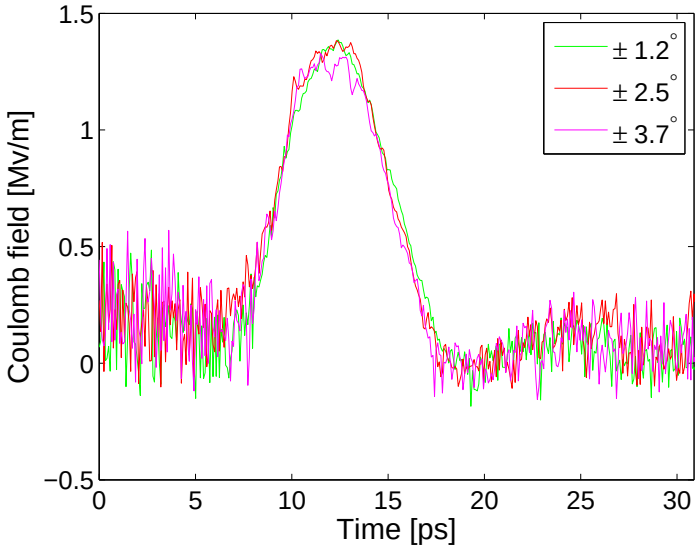

(b)

FIGURE 4.14: Retrieved Coulomb field from the linear and quadratic terms of signal with $\lambda/2$ wave plate at $\pm 1.2°$, $\pm 2.5°$ and $\pm 3.7°$ pairs: (a) Retrieved Coulomb field from the linear term; (b) Retrieved Coulomb field from the quadratic term.

the electron bunches are drifting with time, and they are encoded with different wavelength segment. The $\lambda/2$ wave plate in this measurement is designed for 780 nm only. Therefore, for the encoding with wavelengths other than 780 nm, a potential $\lambda/2$ wave plate angle error is induced.

4.5.3 Method by single shot measurement with one calibration

The Coulomb field can be obtained from a single shot measurement with $\lambda/2$ wave plate at arbitrary positions, but requires a separate one-time calibration to be carried out. With the similar definition as shown in the method two, for an ideal crossed polarization measurement, only the quadratic term is measured. The background removed EO signal $I_{23}(\phi)$ and the crossed polarization signal $I(\phi = 0)$ can be expressed as

$$\begin{aligned} I_{23}(\phi) &= I_{laser} \times \left[-A_2 \cdot \sin(4\phi) + A_3 \cdot 2\cos^2(2\phi)\right], \\ I(\phi = 0) &= 2A_3 \cdot I_{laser}. \end{aligned}$$

Therefore, once the crossed polarization signal $I(\phi = 0)$ is obtained, the magnitude of the quadratic term $I_3(\phi)$ at arbitrary $\lambda/2$ wave plate angle can be retrieved. Then the linear term A_2 can be extracted by:

$$A_2 = -\frac{I_{23}(\phi) - I(\phi = 0) \cdot \cos^2(2\phi)}{I_{laser}} \cdot \frac{1}{\sin(4\phi)}. \tag{4.12}$$

For the quadratic coefficient A_3, it can be obtained by $A_3 = \frac{I(\phi=0)}{2I_{laser}}$. Applying this method to the measured data with $\lambda/2$ wave plate angles at $\pm 3.7°$, $\pm 2.5°$ and $\pm 1.2°$ respectively, the retrieved results are shown in figure 4.15.

The profiles from three positive half-wave plate angles match each other very well. So does the profiles from negative angles. However differences appear at the peak between the two groups. The retrieved Coulomb field from the three negative angles are approximately 1.3 MV/m, while those from the three positive angles are approximately 1.5 MV/m. In order to compare with the two-shot retrieval of the previous section, the retrieved Coulomb field profile from a positive angle and the one from its opposite angle are averaged. The results are shown in figure 4.16. The averaged peak Coulomb fields are 1.35, 1.30 and 1.28 MV/m, and their profiles and peak values are consistent with the results from the method by two-shot measurement.

The difference in the profiles of the retrieved fields are related to the sign of $\lambda/2$ wave plate angles. For the three terms constituted measured signal, the background term and quadratic term are both independent of the sign of $\lambda/2$

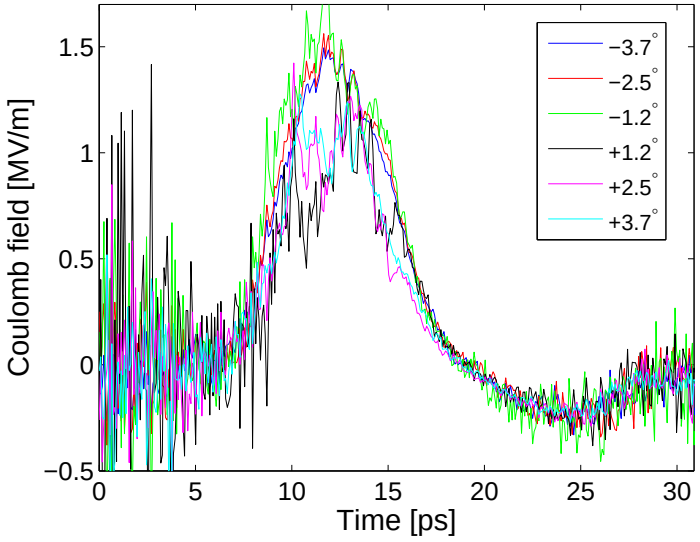

(a)

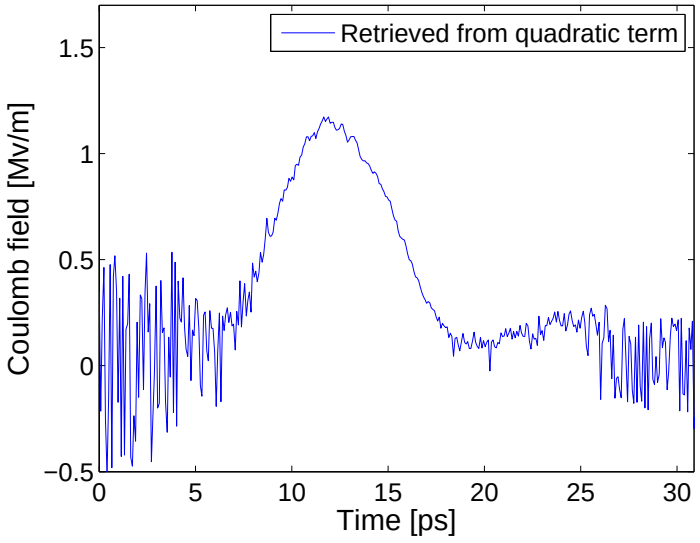

(b)

FIGURE 4.15: Retrieved Coulomb field from: (a) the linear terms of the signal with $\lambda/2$ wave plate at $\pm 1.2°$, $\pm 2.5°$ and $\pm 3.7°$; (b) the quadratic term

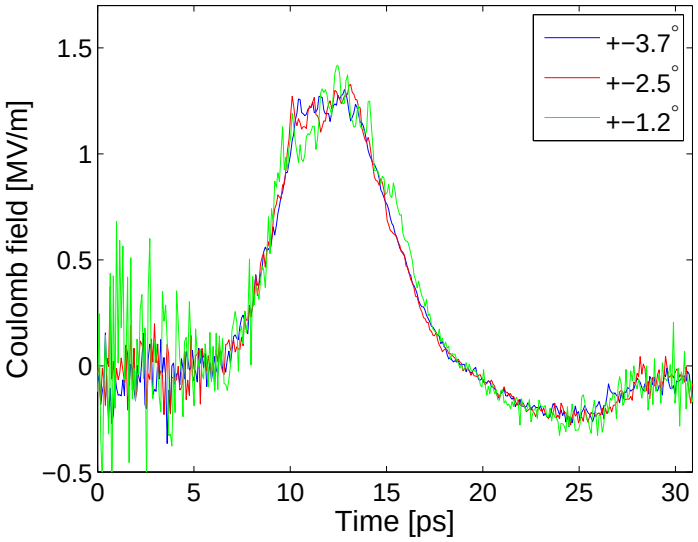

FIGURE 4.16: Averaged Coulomb field profiles from the retrieved Coulomb fields at the opposite half-wave plate angles: ±1.2°, ±2.5° and ±3.7°.

wave plate angle. Therefore, there are two possible reasons: the first being that the data of the quadratic term, which is the $I(\phi = 0)$ term, includes the linear term as well. Then when doing the subtraction $I_{23}(\phi) - I(\phi = 0) \cdot \cos^2(2\phi)$, it removes the quadratic term but induces an extra linear term. This small induced linear term plays a role on the top position of the retrieved Coulomb field. Since the linear term is unknown, it cannot be compensated directly. However, this induced linear term is also dependent on the sign of $\lambda/2$ wave plate angles and it can be removed by averaging the signals from the positive and the negative $\lambda/2$ wave plate angles, which is the principle of the method by two-shot measurement. And also, a linear term can be presumed inside the quadratic term and least squared fitting can be used to find it out, which comes to the method by least-squares fitting; the second possible reason for systematic difference in retrieved field strength with wave plate angle sign is the quarter-wave plate is not at the ideally 0°, or alternatively at the optimised position for compensating the residual birefringence. Adding the quarter-wave plate angle in equation 4.3, we obtain

$$\begin{aligned} I_1 &= A_1 \cdot \sin^2 2(\alpha - \phi), \\ I_2 &= -A_2 \cdot \sin(2\alpha - 4\phi), \\ I_3 &= A_3 \cdot \left[\cos^2(2\phi) + \cos^2 2(\alpha - \phi)\right]. \end{aligned} \tag{4.13}$$

With the quarter wave plate angle added in, the value of a residual quadratic term is related to the sign of $\lambda/2$ wave plate angle, and it can play a role on the

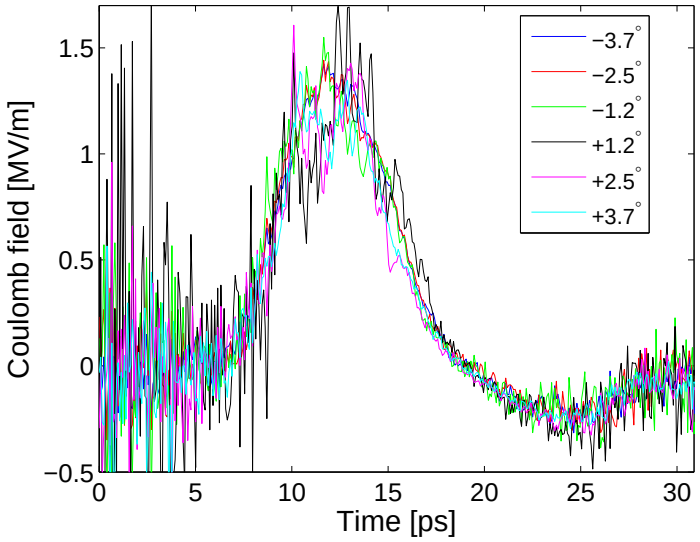

FIGURE 4.17: Retrieved Coulomb field from the linear terms of signal by inducing +0.5° quarter-wave plate offset angle

maximum value of the retrieved field. Applying the above equations into equation 4.12 and quarter-wave plate angle is +0.5°, the result displayed in figure 4.17 is obtained.

The positive and negative data sets agree on their magnitude but not on their profile shape. The retrieved Coulomb field from the three negative angles are from 1.45 MV/m to 1.55 MV/m, while those from the three positive angles are from 1.5 MV/m to 1.8 MV/m (Max. peak). However, the Coulomb field retrieved from crossed polarization detection $I(\phi = 0)$ is 1.17 MV/m. The linear term residing in the quadratic term may be the reason for the disagreement on the profile top between the signals from the positive and negative $\lambda/2$ wave plate angles. The error resident in the three terms of $I(\phi)$ can not be compensated by each other and is added not only in the Coulomb field value, but also in the profile shape.

As a conclusion, an intentional offset half-wave plate introduces all three of the background term, the linear term and the quadratic term in the measured data. Three methods for retrieval of the absolute bunch Coulomb field have been described. The two-shot measurement provides a quick retrieval process to obtain Coulomb field strength. However, the measurement accuracy is sensitive to systematic error in half-wave plate angle. The least-squared fitting method has the ability to reduce this systematic error. The single shot method is not recommended under these measurement conditions. In the condition of the above measurements, the Coulomb field retrieved from the quadratic term at small half-wave plate angle provides lowest uncertainty. The retrieval method from

the linear term has the capability to show the bipolar profile. A retrieved peak field strength of 1.3 MV/m is obtained and is consistent with the known bunch charge and inferred temporal profile. The analysis techniques and the measured signal-noise characterises may be of use in evaluations potential for EO based beam-profile monitors.

4.6 The impact of small half-wave plate angle on the bunch length measurement

In order to obtain higher signal to noise ratio, sometimes the EO measurements are performed in a near-crossed polarization configuration. In this arrangement, the second polarizer is set to a few degrees off from the ideal crossed state. However this leads to a signal that is a combination of the linear and quadratic terms and it may introduce systematic error in the measurement accuracy. To study this affect on signal intensity and bunch length calculation, a 6 ps bunch is in the calculation, and the results are shown in figure 4.18

The peak values of the linear and quadratic terms with $\lambda/2$ wave plate angles are shown in the figure 4.18(a). The factor for the linear term 0.131 and for the quadratic term 0.0136 are obtained in the previous section 4.5 Method by least-squares fitting. At $\lambda/2$ wave plate angle of $+3°$, the magnitude of the linear term and the quadratic term are equal to each other. At $\pi/8$ half-wave plate angle, the linear term achieves maximum value, and both linear term and quadratic term are zero when half-wave plate angle at $\pi/4$. Comparing to the linear term, the quadratic term only varies within the range of 0 to 0.025, which also depends on the Coulomb field value. A ratio value of the linear term (absolute value) over quadratic term is shown in figure 4.18(b). In the plot, at $1°$, the linear term has a value of 34% of the quadratic term. Therefore, even for a small $\lambda/2$ wave plate offset angle, both the quadratic term and linear term have to be considered. Ignoring any term may lead to an inaccurate measurement on the Coulomb field value.

The accuracy of measured bunch length also depends on the half-wave plate angle, and the relation is shown in figure 4.18(c). At half-wave plate $\phi = 0$, the linear term disappears and the measured signal is the quadratic term only. Therefore, it is reasonable to assume that the measured signal is proportional to the Coulomb field squared. Then the bunch length can be obtained by taking a square root of the measured signal, as shown in the red line at $\phi = 0$. As half-wave plate angle

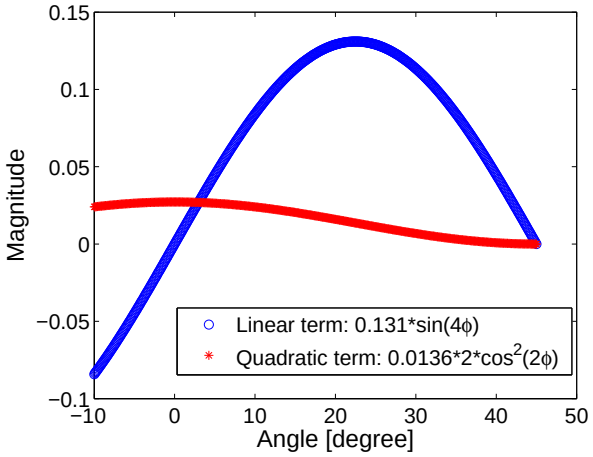

(a)

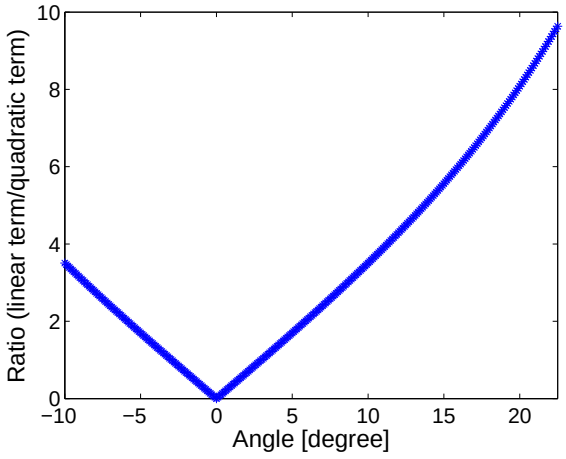

(b)

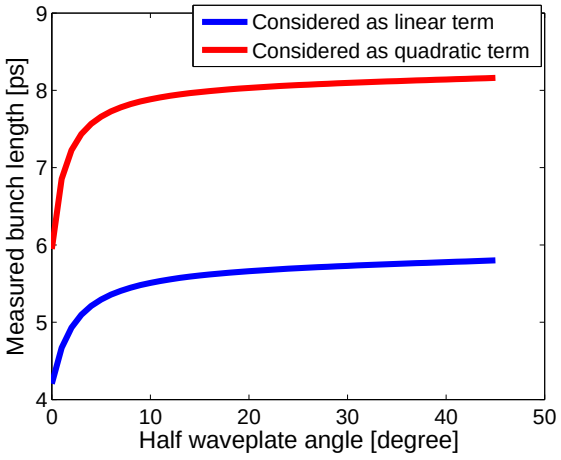

(c)

FIGURE 4.18: Measured signal intensity and bunch length with half-wave plate angles. A 6 ps bunch is supposed in the calculation. (a) Value of the linear and quadratic term; (b) Peak value ratio: Absolute value of the linear term/quadratic term; (c) Measured signal is considered as the linear term (in blue) or considered as the quadratic term (in red).

increases, the linear term starts playing a more significant role, which leads to a broadening on the measured signal. More than 1 ps broadening appears at ϕ over 1.8° if still taking a square root of the signal. In this situation, the measured signal can be considered as proportional to the Coulomb field only and the bunch length can be directly obtained from the signal itself. However, the both above methods are lacking accuracy. The impact of a small half-wave plate angle can not be ignored, but it can be managed by applying a perfect crossed polarization detection, which means zero half-wave plate angle and zero quarter-wave plate angle. Alternatively it can be managed by separating the linear and quadratic terms by the methods discussed in section 4.5.1, 4.5.2 and 4.5.3.

Chapter 5

Phase matching in sideband generation

5.1 Introduction and purpose

A new method, spectral upconversion, for bunch profile diagnostic was reported by Jamison et al in 2010 [13] and Tilborg et al in 2011 [50]. In that work, EO induced spectral broadening of a quasi-monochromatic probe was observed. The novel way to encode THz information into a narrow band laser pulse may have an application in bunch profile measurement with a simplicity of scheme. The underlying physics of the EO interaction is the same as the EOSD that is the subject of this thesis. The sum and difference frequency generation $\omega_{opt} \pm \omega_{THz}$ through the second-order nonlinear optical susceptibility $\chi^{(2)}$ in frequency mixing mechanism, is confirmed in his paper. Comparing to the spectral upconversion method, the EO Spectral Decoding method also relies on the upconverted frequencies, but with the additional effects of interferes with the broadband input probe. Studying the spectral upconversion allows detection issues that apply to EOSD to be examined in a clearer way.

For the upconversion method, only the intensity of THz spectrum is measured. It has a potential application in accelerator beam stabilisation measurement, where the explicit time profile is not required. Based on this method, a simple continuous wave laser can be used for beam diagnostic, which may reduce the laser cost, and simplify the diagnostic system.

In spectral upconversion, the diagnostic information is encoded in the induced sidebands. It is essential to detect the complete non-distorted sidebands. The

propagation direction of the generated sidebands is an important factor that affects the way of detection. For example, it may cause a failure on fibre coupling with an unexpected beam incident angle. The experiment in this chapter discusses the effect of input THz angle on the sidebands' emitting angle. The results can be used to improve the stability and resolution of EOSD system.

5.2 Principle and calculations

5.2.1 Principle and formulas

To describe the upconversion process, which includes sum-frequency and difference-frequency generation, a lossless non-linear optical medium is supposed here. As has been done in Chapter 2 for a broadband optical wave in a collinear geometry, the wave can be defined as:

$$\begin{aligned}\mathbf{E}(\mathbf{r},t) &= \int \widetilde{\mathbf{E}}(\mathbf{r},\omega)\, e^{-i\omega t} d\omega \\ &= \int \widetilde{\mathbf{A}}(\mathbf{r},\omega)\, e^{i\mathbf{k}(\omega)\cdot\mathbf{r}} e^{-i\omega t} d\omega,\end{aligned} \tag{5.1}$$

where $\mathbf{E}(\mathbf{r},t)$ is defined in time domain and varies rapidly in time. $\widetilde{\mathbf{E}}(\mathbf{r},\omega)$ is defined in frequency domain. $\widetilde{\mathbf{A}}(\mathbf{r},\omega)$ is wave amplitude, $\mathbf{k}(\omega)$ is wave vector and $|k| = \frac{n(\omega)\omega}{c}$, which is related to reflect index n and frequency ω. This equation describes a non-monochromatic wave travelling along the direction $\mathbf{r}$. It can stand for a laser beam, a THz beam, a sum-frequency, or difference-frequency beam. The sum frequency generation process is taken for an example here. The wave vector $\mathbf{k}(\omega)$, field $\mathbf{E}$ and direction $\mathbf{r}$ are vectors.

As discussed in Chapter 2, the generated source term is related to the geometry of crystal and incident beams. Without losing generality, we studied the source term in a principal axis, and it can be presented by the laser electric field at frequency ω and THz field at frequency Ω:

$$\begin{aligned}\widetilde{\mathbf{P}}_3(\mathbf{r},\omega) &= 2\epsilon_0\chi^{(2)}(\omega;\Omega,\omega-\Omega)\widetilde{\mathbf{E}}_1(\mathbf{r},\Omega)\,\widetilde{\mathbf{E}}_2(\mathbf{r},\omega-\Omega) \\ &= 2\epsilon_0\chi^{(2)}(\omega;\Omega,\omega-\Omega)\widetilde{\mathbf{A}}_1(\mathbf{r},\Omega)\,\widetilde{\mathbf{A}}_2(\mathbf{r},\omega-\Omega)\, e^{i(\mathbf{k}_1+\mathbf{k}_2)\cdot\mathbf{r}}.\end{aligned} \tag{5.2}$$

Putting the source term $\widetilde{\mathbf{P}}_3(\mathbf{r},\omega)$ into the wave equation, The generated electric field $\widetilde{\mathbf{E}}_3'(\mathbf{r},\omega)$ can be obtained. Here the case of a finite transverse profile beam is

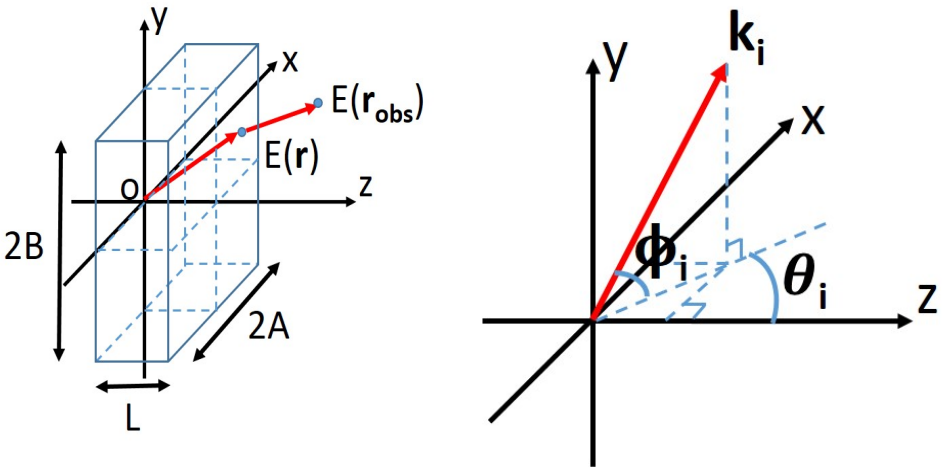

(a) Crystal (b) Wave vector

FIGURE 5.1: scheme of crystal and wave vector position and frame: (a) The rectangular crystal is in the range of $z \in [0, L]$, $x \in [-A, A]$ and $y \in [-B, B]$. $|\mathbf{r}_{obs}|$ is the distance between origin O to observation point; (b) Vector k has an angle of ϕ to x-z plane and an angle of θ between its projection on x-z plane and z axis.

considered, with a non-collinear propagation geometry. Including the contributions of each point in the non-linear crystal and also the propagation from crystal to an observation point as shown in figure 5.1, the detected electric field at the observation point is the integration of $\widetilde{\mathbf{E}}_3'(\mathbf{r}, \omega)$ over the entire crystal, shown as:

$$\begin{aligned} \widetilde{\mathbf{E}}_3(\mathbf{r}_{obs}, \omega) &= \int\int\int e^{i\Phi_3} \widetilde{\mathbf{E}}_3'(\mathbf{r}, \omega)\, d\mathbf{r} \\ &= \int\int\int e^{i(\mathbf{r}_{obs}-\mathbf{r})\cdot\mathbf{k}_3} \widetilde{\mathbf{E}}_3'(\mathbf{r}, \omega)\, d\mathbf{r}. \end{aligned} \tag{5.3}$$

Extending $\widetilde{\mathbf{E}}_3'(\mathbf{r}, \omega)$ in equation 5.3, we can get a general result:

$$\widetilde{\mathbf{A}}_3(\mathbf{r}_{obs}, \omega) = \widetilde{B}(\omega)\chi^{(2)}(\omega; \Omega, \omega - \Omega) \int\int\int \widetilde{\mathbf{A}}_1(\mathbf{r}, \Omega)\, \widetilde{\mathbf{A}}_2(\mathbf{r}, \omega - \Omega)\, e^{i\Delta\mathbf{k}\cdot\mathbf{r}} d\mathbf{r}, \tag{5.4}$$

where $\widetilde{B}(\omega) = i\omega^2/[2c^2 k_3(\omega)]$, and

$$\Delta\mathbf{k}(\omega; \Omega, \omega - \Omega) = \mathbf{k}_3(\omega) - \mathbf{k}_1(\Omega) - \mathbf{k}_2(\omega - \Omega). \tag{5.5}$$

Therefore, based on the geometry in figure 5.1(b), wave vector $\mathbf{k}$ has an angle of ϕ to x-z plane and an angle of θ between its projection on x-z plane and z axis:

$$\Delta k_x(\phi, \theta) = |\mathbf{k}_3| \cos\phi_3 \sin\theta_3 - |\mathbf{k}_2| \cos\phi_2 \sin\theta_2 - |\mathbf{k}_1| \cos\phi_1 \sin\theta_1, \tag{5.6}$$

$$\Delta k_y(\phi,\theta) = |\mathbf{k}_3|\sin\phi_3 - |\mathbf{k}_2|\sin\phi_2 - |\mathbf{k}_1|\sin\phi_1, \tag{5.7}$$

$$\Delta k_z(\phi,\theta) = |\mathbf{k}_3|\cos\phi_3\cos\theta_3 - |\mathbf{k}_2|\cos\phi_2\cos\theta_2 - |\mathbf{k}_1|\cos\phi_1\cos\theta_1. \tag{5.8}$$

The incident beams are assumed to have Gaussian transverse profiles. The propagation is assumed to be sufficiently close to collinear, and transverse size large, propagation distance sufficiently small, that the beams do not appreciably walk-off transversely. Therefore the wave amplitudes are independent of z axis. Then the equation 5.4 can be rewritten in a rectangular coordinate system as:

$$\begin{aligned}\widetilde{A}_3(\omega,\phi,\theta) =& \widetilde{B}(\omega)\chi^{(2)}(\omega;\Omega,\omega-\Omega)\\ &\cdot\int_0^L e^{i\Delta k_z z}dz\int_{-\infty}^{+\infty}\int_{-\infty}^{+\infty}\widetilde{A}_1(\Omega,x,y)\,\widetilde{A}_2(\omega-\Omega,x,y)\,e^{i(\Delta k_x x+\Delta k_y y)}dxdy.\end{aligned} \tag{5.9}$$

The Gaussian transverse profiles can be defined as:

$$\widetilde{A}_i(x,y,z=0,\omega_i) = \widetilde{A}_i(\omega_i)\,e^{-\frac{y^2}{b_{y_i}^2}-\frac{x^2}{b_{x_i}^2}}, \tag{5.10}$$

where $i = 1,2$ indicates the two incident beams Ω and $\omega-\Omega$ respectively, and b_y, b_z defines the Gaussian width in their dimension. Put equation 5.10 into 5.9, then we can get:

$$\begin{aligned}\widetilde{A}_3(\omega,\phi,\theta) =& \widetilde{B}(\omega)\chi^{(2)}(\omega;\Omega,\omega-\Omega)\widetilde{A}_1(\Omega)\,A_2(\omega-\Omega)\\ &\cdot\int_0^L e^{i\Delta k_z z}\cdot dz\int_{-\infty}^{+\infty}dy\cdot e^{-\frac{y^2}{b_y^2}+i\Delta k_y y}\int_{-\infty}^{+\infty}dx\cdot e^{-\frac{x^2}{b_x^2}+i\Delta k_x x},\end{aligned} \tag{5.11}$$

where we define:

$$\begin{aligned}\frac{1}{b_x^2} &= \frac{1}{b_{x_1}^2}+\frac{1}{b_{x_2}^2},\\ \frac{1}{b_y^2} &= \frac{1}{b_{y_1}^2}+\frac{1}{b_{y_2}^2}.\end{aligned} \tag{5.12}$$

In equation 5.11, the intergrations can be calculated separately:

$$\int_0^L e^{i\Delta k_z z}dz = \frac{e^{i\Delta k_z L}-1}{i\Delta k_z}, \tag{5.13}$$

and

$$\begin{aligned}\int_{-\infty}^{+\infty} dx e^{-\frac{x^2}{b_x^2}+i\Delta k_x x} &= e^{\left(\frac{ib_x}{2}\Delta k_x\right)^2}\cdot b_x \cdot \int_{-\infty}^{+\infty} e^{-\left(\frac{x}{b_x}-\frac{ib_x}{2}\Delta k_x\right)^2} d\left(\frac{x}{b_x}-\frac{ib_x}{2}\Delta k_x\right) \\ &= e^{\left(\frac{ib_x}{2}\Delta k_x\right)^2}\cdot b_x \cdot \sqrt{\pi}.\end{aligned} \tag{5.14}$$

A similar result can be obtained for y component. Putting the integration results 5.13 and 5.14 into 5.11, then the final result for the generated field at the observation point is:

$$\begin{aligned}\widetilde{A}_3(\omega,\phi,\theta) =& \widetilde{B}(\omega)\chi^{(2)}(\omega;\Omega,\omega-\Omega)\widetilde{A}_1(\Omega)\,\widetilde{A}_2(\omega-\Omega) \\ &\cdot \frac{e^{i\Delta k_z L}-1}{i\Delta k_z}\cdot \pi b_x b_y e^{-\left(\frac{b_x}{2}\Delta k_x\right)^2} e^{-\left(\frac{b_y}{2}\Delta k_y\right)^2}.\end{aligned} \tag{5.15}$$

To consider the contributions of all of THz wave frequency components, the $\widetilde{A}_3(\omega,\phi,\theta)$ needs to be integrated over the entire THz spectrum Ω. The generation efficiency of new frequency is related to the phase matching efficiency of each incident beam frequency. This phase matching efficiency is described by the phase matching term in equation 5.15, and has a form of:

$$\widetilde{\xi}(\omega,\phi,\theta) = \frac{e^{i\Delta k_z L}-1}{i\Delta k_z}\cdot \pi b_x b_y e^{-\left(\frac{b_x}{2}\Delta k_x\right)^2} e^{-\left(\frac{b_y}{2}\Delta k_y\right)^2}. \tag{5.16}$$

As $\left|\frac{e^{i\Delta k_z L}-1}{i\Delta k_z}\right|^2 = L^2\mathrm{Sinc}^2(\Delta k_z L/2)$ is known, equation 5.16 indicates that the intensity of the new generated wave is modulated not only by the Sinc^2 function in the propagation direction z, but also by the transverse profiles in the x-y plane, by the relative propagation angles of the incident beams, and by the observation angle. The beam transverse profiles restrict the phase matching process further. With increasing the beam size b_i, the bandwidth of phase matching function will become narrower, and the phase matched or nearly matched area shrinks which implies the emitting angle of the generated upconversion signal goes down.

Turning to our frequency upconversion experiment, a quasi-monochromatic laser, tens of picosecond duration, and a THz pulse are incident into a ZnTe crystal. Due to the sum-frequency and difference-frequency generation, the output light will generate sidebands at the central laser frequency in its spectrum, which is shown in [13] and here in the schematic diagram 5.2. The spectrum is expected following the $\chi^{(2)}$ interaction of monochromatic probe at frequency ω_0 with THz

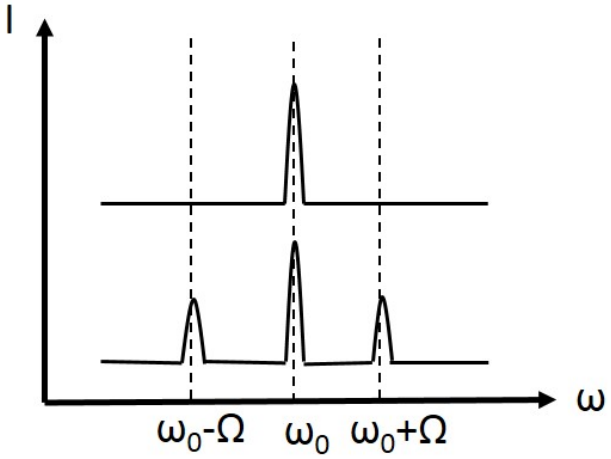

FIGURE 5.2: Schematic diagram of sidebands generation. Upper: input monochromatic probe at frequency ω_0. Bottom: generated sidebands at $\omega_0+\Omega$ and $\omega_0-\Omega$ with input THz frequency Ω through $\chi^{(2)}$ interaction.

wave at frequency Ω. For EOSD, the output spectrum is a summation over all possible input frequencies $\{\omega_0\}$ and THz frequency $\{\Omega\}$.

To describe the equation 5.5 in details based on the geometry in figure 5.1, a frame can be chosen that the THz beam and laser beam only propagate in the x-z plane. In the experiment, the laser beam propagates along the z-axis with $\phi_1 = 0$ and $\theta_1 = 0$. The THz beam propagates in the x-z plane with $\phi_2 = 0$ and $\theta_2 = \theta$. The generated signal is observed in x-z plane so that $\phi_3 = 0$. To simplify the notation, $\theta_3 \equiv \phi$ is defined here. In order to show clearly the phase matching process in this specific case, the notation is changed to that $\mathbf{k}_{sum} = \mathbf{k}_3$, $\mathbf{k}_{THz} = \mathbf{k}_1$, $\mathbf{k}_{opt} = \mathbf{k}_2$, and $\omega_{opt} = \omega - \Omega$. Therefore for the sum-frequency generation, the phase matching process is:

$$\Delta k_x^+ = |\mathbf{k}_{sum}(\omega_{opt}+\Omega)|\sin\phi - |\mathbf{k}_{THz}(\Omega)|\sin\theta, \tag{5.17}$$

$$\Delta k_y^+ = 0, \tag{5.18}$$

$$\Delta k_z^+ = |\mathbf{k}_{sum}(\omega_{opt}+\Omega)|\cos\phi - |\mathbf{k}_{THz}(\Omega)|\cos\theta - |\mathbf{k}_{opt}(\omega_{opt})|. \tag{5.19}$$

Similar, the phase matching process of the difference-frequency generation is:

$$\Delta k_x^- = -|\mathbf{k}_{diff}(\omega_{opt}-\Omega)|\sin\phi - |\mathbf{k}_{THz}(\Omega)|\sin\theta, \tag{5.20}$$

$$\Delta k_y^- = 0, \tag{5.21}$$

$$\Delta k_z^- = -|\mathbf{k}_{diff}(\omega_{opt}-\Omega)|\cos\phi - |\mathbf{k}_{THz}(\Omega)|\cos\theta + |\mathbf{k}_{opt}(\omega_{opt})|, \tag{5.22}$$

where, the Ω is the THz frequency, and $k = \frac{n(\omega)\omega}{c}$. The ZnTe refractive index for 800 nm and for THz beam can be found in equation 3.2 and 3.4.

5.3 Experiment

5.3.1 Setup description

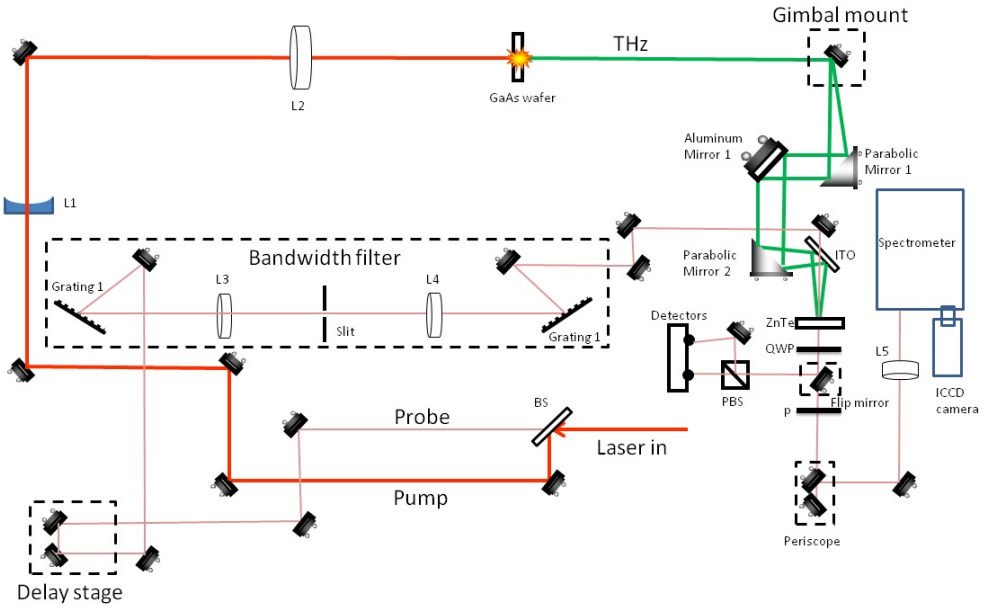

FIGURE 5.3: Scheme of setup: a broadband laser is splitted into probe beam and pump beam. The probe beam passes through a delay stage and a bandwidth filter, becoming a narrow band laser beam. The pump beam is expended and focused on a GaAs wafer to generate THz wave. The THz wave modulates the probe beam in a 4 mm ZnTe crystal and can be detected either by a balance detection or by a spectrometer with ICCD camera.

In order to study the angular distribution of the emitted optical wave in spectral upconversion based on the phase matching process, a setup, shown in figure 5.3, is built up. In the figure, the laser comes from a 1 kHz titanium sapphire laser system ($\lambda_0 = 800$ nm). The laser beam is splitted to pump and probe beams by a beam splitter, and 90% of laser energy towards the pump arm. In the pump beam line, THz is generated by a GaAs wafer, and passes through two parabolic mirrors setting for angle tuning measurement. The probe beam passes through a bandwidth filter, mainly composed by two gratings and two focus lens, and the output probe has a 0.5 nm narrow bandwidth. The probe beam and THz beam are combined in the crystal by a dichroic mirror. The detection system can be switched between balance detection for THz time domain scanning and crossed

polarization detection for emission angle distribution measurement. Since the THz beam, laser beam and generated signal beam should remain in a same plane, a 90 degree periscope in the detection part can transfer the horizontal varying of the THz beam into vertical varying in spectrometer as shown in the figure 5.4. A 200 mm spherical lens (L_5 in figure 5.3) focuses the beam into the entrance pupil of a spectrometer. A vertical slit sits on the frequency spectral plane of lens L_5 and this lens converts the signal emission angle into spatial position. The slit also removes the horizontal spectrum in order to improve the resolution of the spectrometer. An ICCD camera on the exit pupil of the spectrometer images this spatial position on the entrance pupil. The purpose of the arrangement is to measure the upconverted spectrum and its angular dependence, as a function of the incident THz wave angle. Therefore it is essential to quantify and measure the non-collinear angle between the incidences. The setting of two parabolic mirrors as shown in figure 5.5 can achieve this purpose.

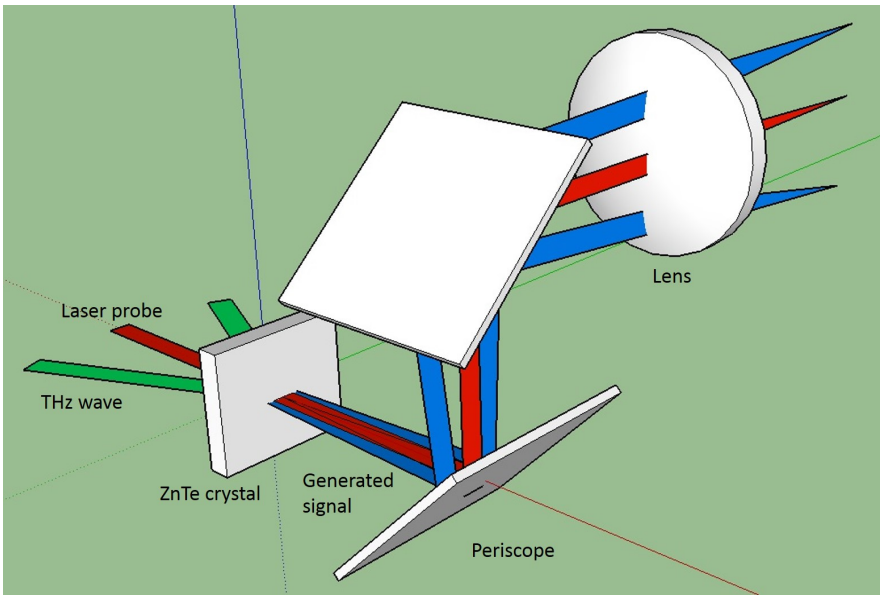

FIGURE 5.4: Horizontal angular variation is converted to vertical position variation at the spectrometer entrance slit.

A THz beam incidents on a mirror with a gimbal mount, collected by two parabolic mirrors, and finally focused in a 4 mm ZnTe crystal. The mirror sitting in the gimbal mount can be tuned around its centre axis, and the THz beam is focus on the centre of this mirror. The centre point of this mirror is also the focal point of the parabolic mirror 1. In figure 5.5, the green and red lines show THz beam after the gimbal mounted mirror with two different incident angles. All the beams between the two parabolic mirrors are parallel. The parabolic mirror 2 focuses all the parallel beams in ZnTe crystal. Since the two parabolic mirrors have the equal 152.4 mm reflected focal length, the image magnification is 1 and

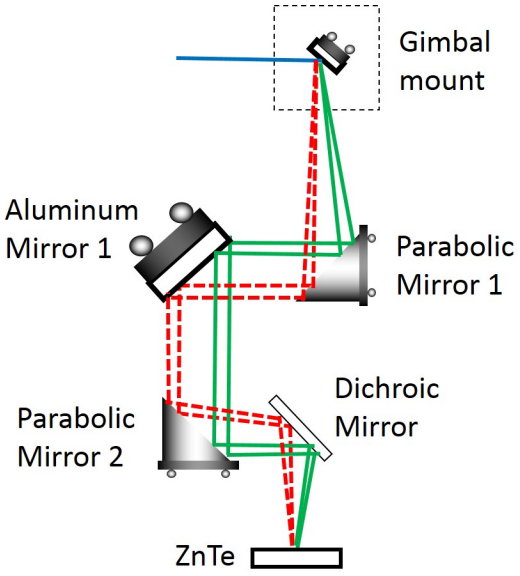

FIGURE 5.5: Setting of the two parabolic mirrors: green beam and red beam are with different mirror tuning angles

the THz tuning angle on ZnTe crystal can be read out from the gimbal mount with an accuracy of 0.1°. Care has to be taken that if the mirror on gimbal mount rotates angle θ, the output THz wave will rotate 2θ. Due to this setting, the focal spot in ZnTe crystal is an image of the focal spot on the mirror on gimbal mount with the same size. Therefore, the focal point in ZnTe stays stable and is independent with the incident angle. For optical path, comparing to the red beam, the short travelling distance of the green beam outside the two parabolic mirrors can be compensated by travelling longer distance between this two mirrors. As a consequence, both focusing position and arriving time of THz beam on ZnTe crystal will not change with the incident angle tuning.

The THz focal spot size on the gimble mirror, which is the same size as on the ZnTe crystal, can be calculated by the complex beam parameter of Gaussian beam. Its value at the position just before lens L_1 can be expressed by following:

$$\frac{1}{q_{in}(z)} = \frac{1}{R(z)} - i\frac{\lambda}{\pi w^2(z)}, \tag{5.23}$$

where z is the position on the beam propagation direction, R is the curvature radius of wave front, and w is beam waist. The scheme of laser beam expending and focusing by lens L_1, L_2, and THz generation by a GaAs wafer are shown in the whole system scheme 5.3. Since the collimated optical beam normal incidents on lens L1 with a beam size 10 mm, the curvature radius R is infinity and the q_{in} is only related to optical wavelength ($\lambda = 800$ nm) and beam size ($w_0 = 10$ mm). After propagating, the beam complex parameter on GaAs wafer can be

calculated by 'ABCD' law [75]:

$$\begin{pmatrix} A & B \\ C & D \end{pmatrix} = \begin{pmatrix} 1 & d_2 \\ 0 & 1 \end{pmatrix} \begin{pmatrix} 1 & 0 \\ -\frac{1}{f_2} & 1 \end{pmatrix} \begin{pmatrix} 1 & d_1 \\ 0 & 1 \end{pmatrix} \begin{pmatrix} 1 & 0 \\ -\frac{1}{f_1} & 1 \end{pmatrix}, \tag{5.24}$$

where the $d_1 = 127.5$ cm and $d_2 = 36.0$ cm are the distance from lens L_1 to L_2, and from L_2 to the wafer respectively. The focal lens of L_1 and L_2 are -30 mm and 600 mm and their diameters are 25.4 mm and 101.6 mm respectively. Then the complex beam parameter on the wafer position is:

$$q_{out} = \frac{Aq_{in} + B}{Cq_{in} + D}. \tag{5.25}$$

On the wafer surface, the generated THz continues to propagate along the optical wave direction, which implies having the same q value, but different wavelength. After the wafer, the propagation of generated THz wave to the gimbal mirror can be calculated by the 'ABCD' matrix again. Through the equation 5.23 with THz wavelength, the THz Gaussian beam waist at the gimbal mirror can be calculated. Figure 5.6 shows the calculation result that the THz focal size is linearly dependent with wavelength, and the range of wavelength is equivalent to THz range from 0.1 THz to 6 THz in the figure. For 1 THz beam (0.3 mm wavelength), the focal point size at the mirror is 0.5 mm.

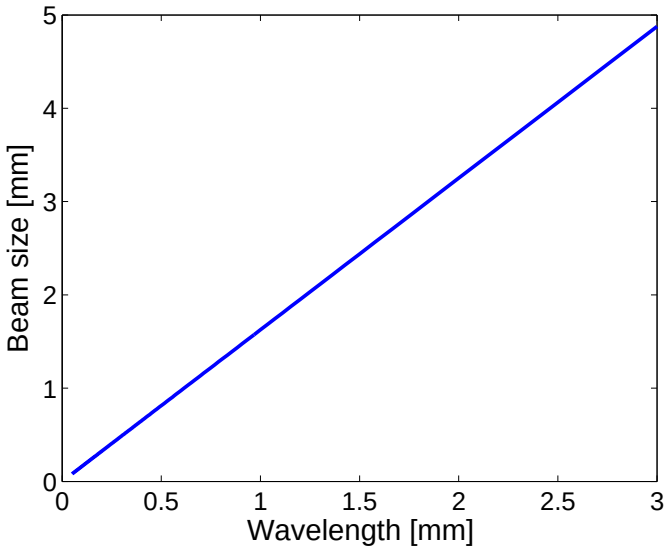

FIGURE 5.6: Calculation of THz beam size on the gimbal mirror with wavelength

To quantitatively study the emission angle with respect to the THz incident angle, the measured position on ICCD camera needs to be calibrated to the output angle

from the ZnTe crystal. Since the entrance of the spectrometer is imaged on the ICCD camera, the relation of beam position on the entrance to the emission angle can be calculated first, and an image magnification factor is considered to obtain the calibration on the camera CCD. The scheme of the beam propagation from the ZnTe crystal to spectrometer is shown in the figure 5.7, where the angle θ is the beam emission angle at ZnTe crystal and x is the distance of beam position to the centre of the spectrometer entrance. The entrance is set at the focal plane of the lens L_5 with focal length $f = 200$ mm, so that the collimated emission beam with angle θ will be focused at position x, with a relation that $x = \tan\theta \cdot f$.

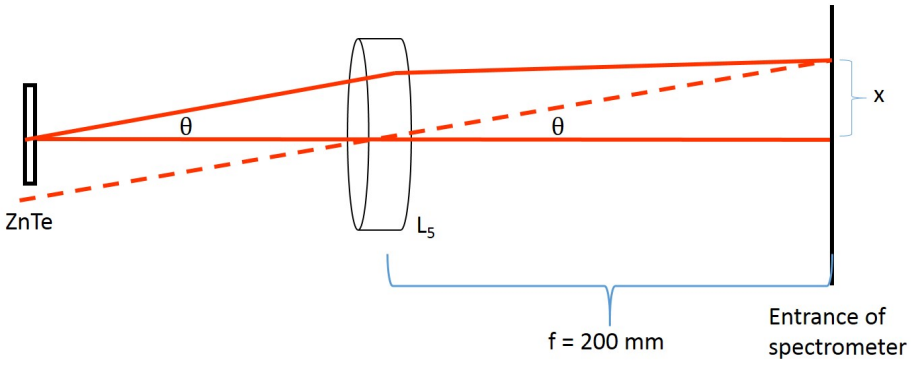

FIGURE 5.7: Effective lens arrangement used for calibrating the angle to displacement relationship in the upconversion detection

From the entrance to the camera CCD, an image magnification is included in the calculation that $x = \frac{d}{M}$, where $d = 3.45$ mm is the half of CCD vertical size (512 pixels), $M = 1.1/2.17$ is an image magnification through the spectrometer and ICCD camera, including the spectrometer magnification 1.1 and camera intensifier to CCD deflation factor 2.17. Therefore the emission angle can be calculated by the following equation:

$$\theta = \tan^{-1}\left(\frac{d}{Mf}\right). \tag{5.26}$$

As a calculation result, the angle calibration factor is 0.5651°/mm and 0.0038°/pixel. The 6.9 mm full size of CCD can cover 3.9° external angle. Since the angle considered here is in a small range, the relationship of angle θ and position d can be seen as approximately linear. Because of diffraction limit from lens L_5 in figure 5.3, the resolution R on the entrance of spectrometer can be calculated by $R \approx \frac{1.22f\lambda}{D} = 97.6\ \mu m$, where f is 200 mm focal length, λ is 800 nm optical beam wavelength, and D is 2 mm probe beam size. Therefore, on the CCD the smallest spot can be resolved is 50 μm, which is approximately 7 pixels (6.7 μm/ pixel).

5.3.2 Spectrometer calibration

Experimental data was acquired by a PCO pro ICCD camera after the monochromator (HORIBA JOBIN YVON, iHR550). The wavelength scaling of the spectrum depends on the camera alignment and needs to be calibrated for each new setup.

In the sidebands generation experiment, a narrow band probe laser comes out of a bandwidth filter. The method for calibration is that: a slit in the bandwidth filter can be moved to select different wavelength, and its position and the spectrum of the narrow band probe laser can be recorded by both a commercial USB spectrometer (OceanOptics Inc. USB4000) and PCO camera via iHR550. Based on the same slit position, the iHR550 spectrometer can be calibrated by the USB spectrometer.

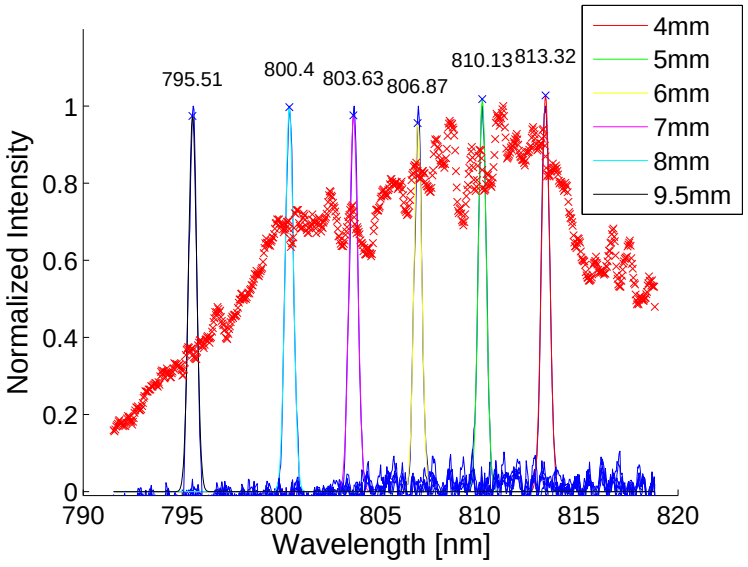

FIGURE 5.8: Spectrum of probe beam measured by a USB spectrometer: The Fourier plane slit position is from 4 mm to 9.5 mm. The red 'x' mark line is the full spectrum of probe beam without Fourier plane filter.

Figure 5.8 shows the spectrum of the narrow band probe measured by the USB spectrometer. The entrance slit size is 16 μm, and position is from 4 mm to 9.5 mm. The blue curves in the back are recorded spectrum, and the colour curves in the front are their Gaussian fittings. The red 'x' mark line is the full spectrum of probe beam without Fourier plane filter. The parameters are shown in the following table 5.1:

From this measurement on wavelength versus detector pixel number, a calibration factor of -1.76×10^{-2} nm/pixel with 0.4% standard error is obtained. The bandwidth of the narrow probe is 0.45 nm FWHM.

TABLE 5.1: Spectrum calibration

Fourier plane filter position(mm)	4	5	6	7	8	9.5
wavelength(nm)	813.32	810.13	806.87	803.63	800.4	795.51
Pixel	185	371	558	745	933	1208

5.4 Measurement Analysis

5.4.1 Sidebands imaging

In the emission angle measuring experiment, a 4 mm thick ZnTe crystal is used and an iris is used after the bandwidth filter to provide a certain transverse beam size for the probe beam. The measurement results are shown in figure 5.9.

The figure shows the generated sum and difference sidebands with different emission angle when the incident THz beam is not collinear with the probe beam. The images are background removed and 30 shots averaged. The result of figure 5.9(a) 5.9(b) 5.9(c) are obtained from a 2 mm size beam with 0 degree, 6 degree and 14 degree THz incident angle respectively. Figure 5.9(d) is obtained from a 4 mm beam size probe at 14 degree THz incident angle. The maximum emission angle difference between sum and difference frequency is around 0.08 degree (external angle) at 14 degree non-collinear angle.

Figure 5.10 shows the external angle chirp induced by the THz incident angles. The centre angles are obtained by Gaussian fitting for the profile at each THz frequency component. The angle chirp linearly depends on THz frequency in the first three images of figure 5.9. From the plots, it obviously shows that the 0 degree incident THz angle has an offset error, since its slope is not zero as expected from calculation. Between ± 0.1 THz range, the plot is invalid because the low intensity of THz frequency components lead to a poor signal to noise ratio. In order to describe angular offset induced by the phase matching, a standard of chirp rate, which is defined as the external angle per unit frequency after emitting out of crystal divided by the external incident angle before crystal front, is induced here. This chirp rate is related to the crystal refractive index, its frequency response and laser centre wavelength (corresponds to refractive index). The chirp rate measured for this 4 mm ZnTe with 800 nm probe laser is 2.7×10^{-3} THz^{-1}, which includes the correction of the offset error at incident angle. The chirp rate for GaP can be found in reference [76].

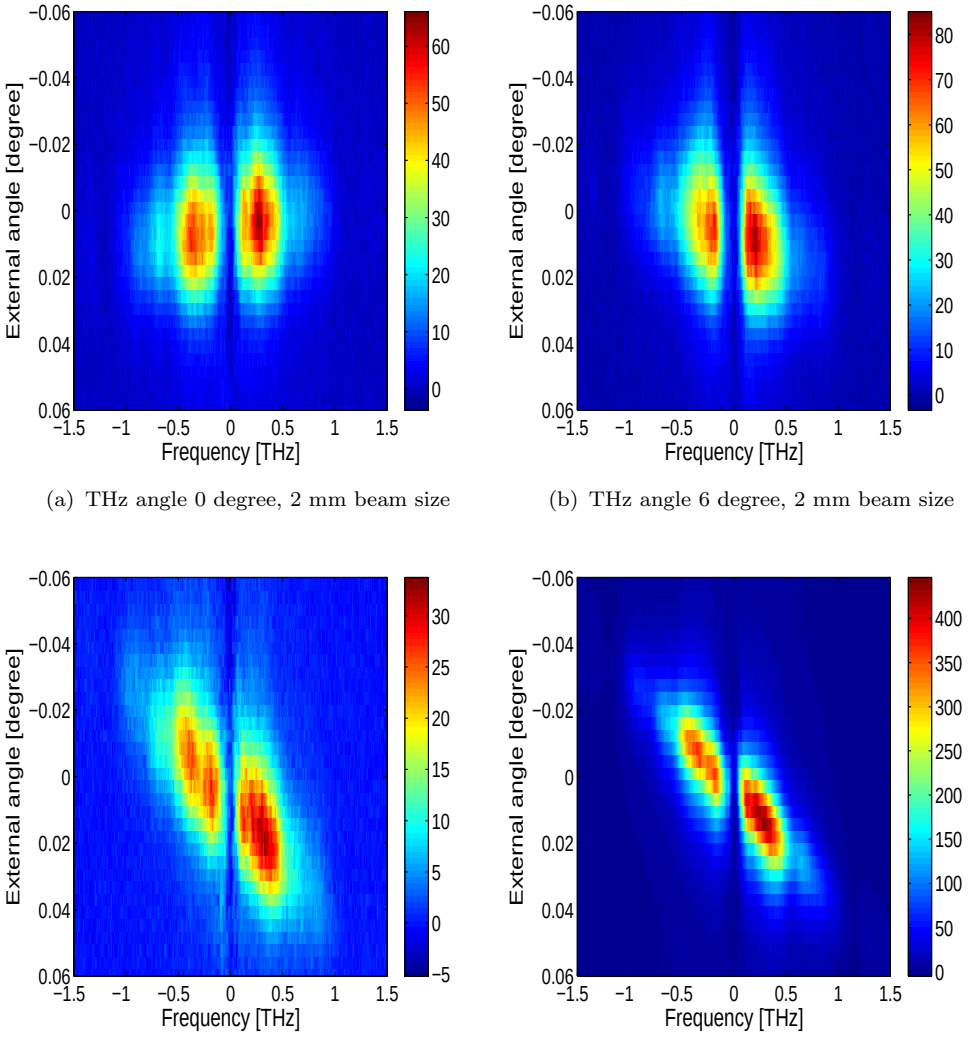

(a) THz angle 0 degree, 2 mm beam size

(b) THz angle 6 degree, 2 mm beam size

(c) THz angle 14 degree, 2 mm beam size

(d) THz angle 14 degree, 4 mm beam size

FIGURE 5.9: Angle-wavelength mapping of phase matching: the measured data includes THz bandwidth with a 4 mm thick ZnTe crystal. The THz external incident angle is 0°, 6°, 14°, and probe beam size is 2 mm or 4 mm

5.4.2 Calculation results

In figure 5.11, a phase matching scheme is shown. θ is the THz incident angle, according to laser propagation direction, while φ is signal emission angle.

In order to calculate upconversion signal's angular spread with a certain input THz angle as in the experiment, the input laser pulse is set at normal incidence on the crystal. Figure 5.12 shows the calculated spectrum as function of the observation angle, calculated based on equation 5.16, with several THz incident angles. The thickness of the crystal is 4 mm. The vertical axis shows external angle of the generated signal, and horizontal axis is wavelength. The figures show

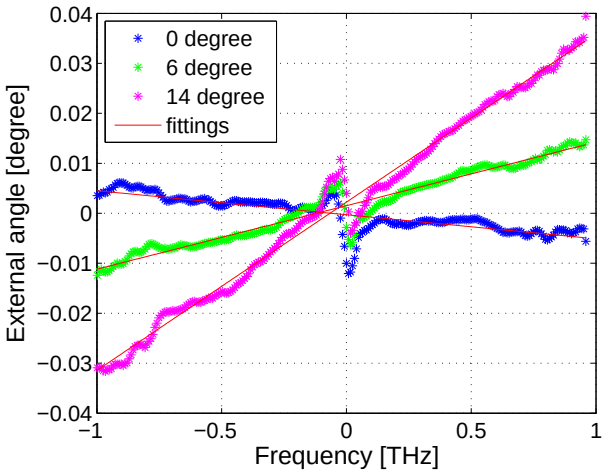

FIGURE 5.10: Induced external angle chirp by THz incident angles at 0°, 6° and 14°

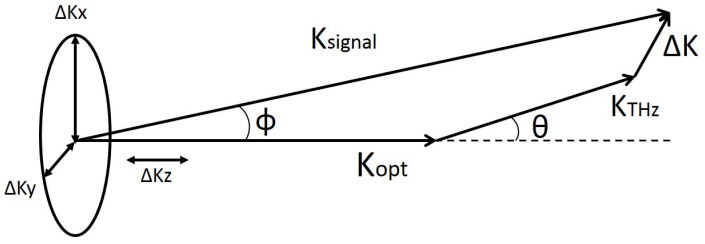

FIGURE 5.11: Scheme of phase matching: Vector K_{THz} has an angle θ to z axis and vector K_{signal} has an angle ϕ to z axis.

the magnitude square of phase matching efficiency, included THz field, $\widetilde{\xi}(\omega, \phi, \theta) \cdot \widetilde{E}_{THz}$. The centre wavelength is 800 nm (375 THz), shown as 0 THz in the figure. The THz and optical beams are refracted at the ZnTe crystal boundaries, and the figures show the angle outside crystal (external angle) in the figure. The internal angles θ_{int} are converted to external θ_{ext} by $\theta_{ext} = \sin^{-1}(n \sin(\theta_{int}))$, where n is refractive index in the crystal. With the THz incident angle increasing, the sum and different frequency signals are going toward to a larger emission angle. For 14° THz incident angle, the signal emission full angle is less than 0.1° external angle. The beam size effect can be seen by comparing the figure 5.12(c) with 5.12(d) as it is explained for the equation 5.16. The calculations agree with the measured results in figure 5.9. As will be shown, despite the angles being small they can give rise to measurable consequences in the EO crystal.

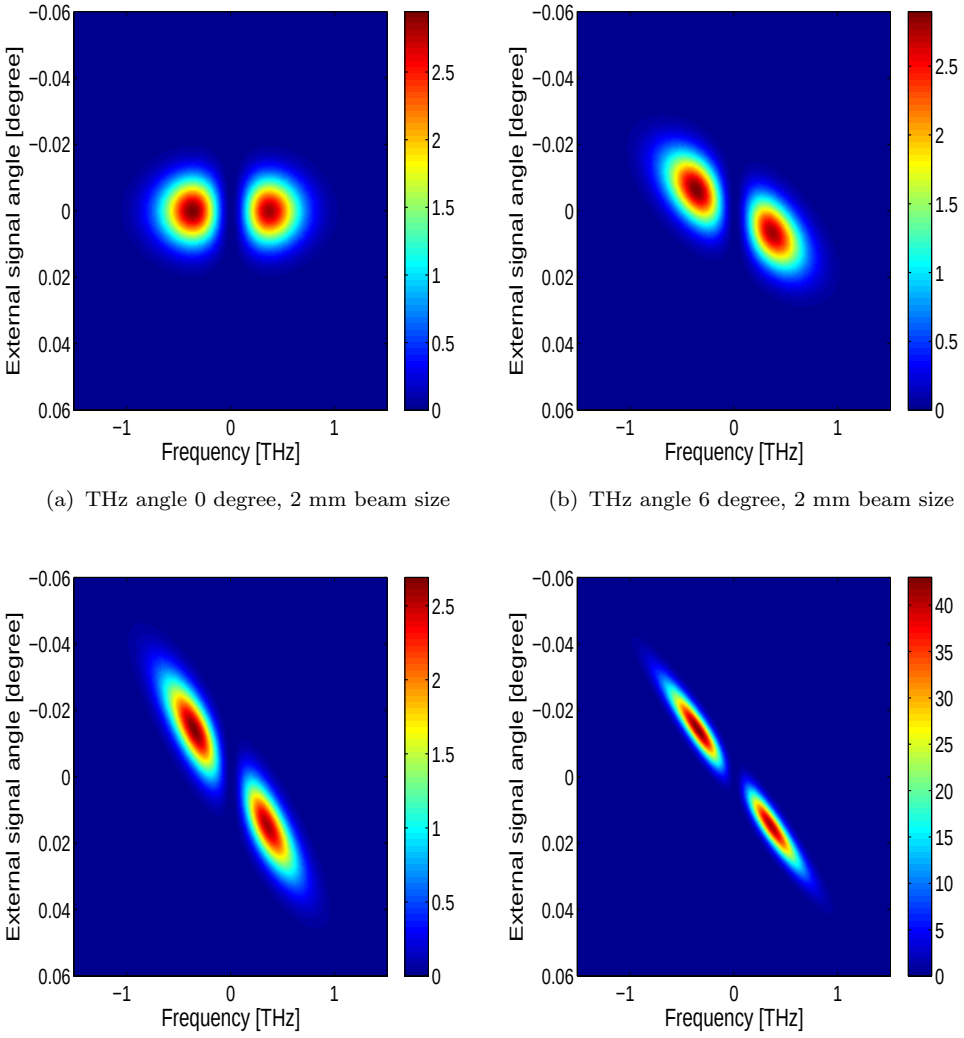

(a) THz angle 0 degree, 2 mm beam size

(b) THz angle 6 degree, 2 mm beam size

(c) THz angle 14 degree, 2 mm beam size

(d) THz angle 14 degree, 4 mm beam size

FIGURE 5.12: Intensity of upconversion signal with angular spread ϕ and wavelength Ω mapping by calculation. Three external THz angle θ situations with 2 mm beam size: (a) $\theta = 0$ degree, (b) $\theta = 6$ degree and (c) $\theta = 14$ degree. (d) shows the result at $\theta = 14$ degree with 4 mm probe beam size. Horizontal axis is wavelength and vertical axis is external emission angle.

5.5 Implications for EOSD

In the upconversion measurement, the quasi-monochromatic laser interacts with a THz wave. The EOSD measurement is a summation of all of these interactions at each probe frequency. This study on the induced sidebands emission angle chirp by non-collinear incident beams can be directly applied in EOSD detection. The frequency components of the measured EO signal on fibre coupling, therefore can be estimated.

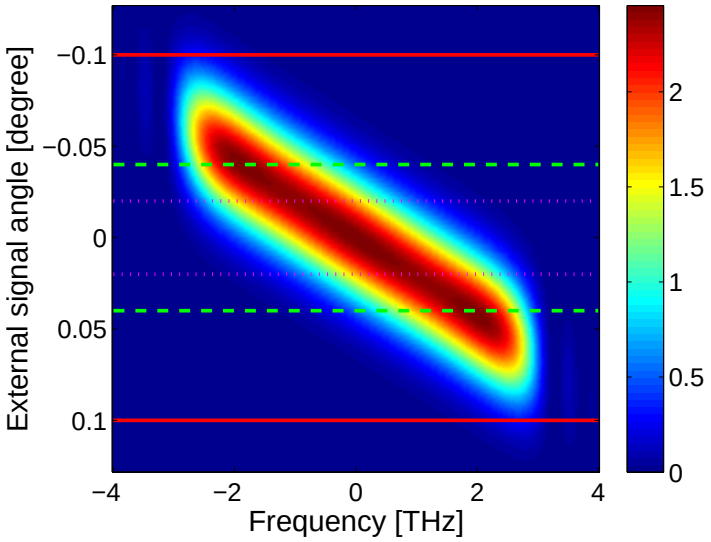

(a) Phase matching efficiency mapping

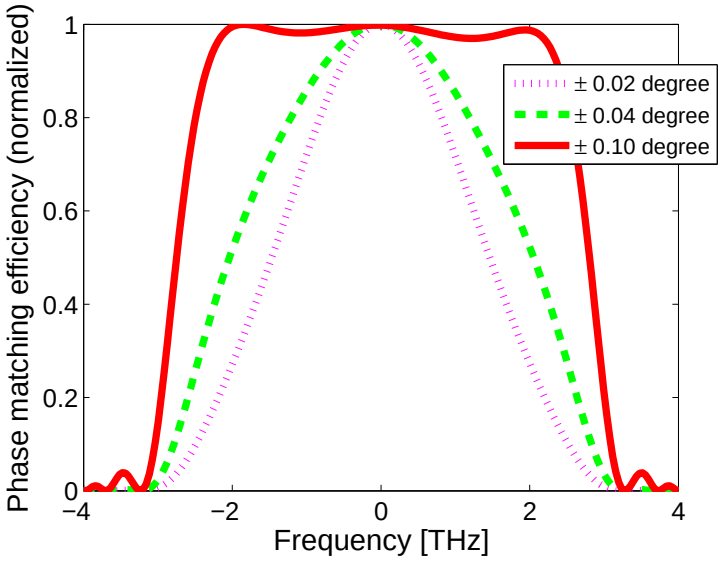

(b) Normalized spectrum of the phase matching efficiency

FIGURE 5.13: Bandwidth related to external angle acceptance: phase matching efficiency with 500 μm thick ZnTe, 500 μm incident beam size and 7 degree external THz incident angle. The dotted line, dashed line and straight line show the transmitting allowed emission angle between ±0.02, ±0.04, and ±0.1 degree respectively.

5.5.1 Fibre coupling calculation

The process of sidebands generation is shown in the above calculations and measurements. This process is a combination of THz frequency replica and phase matching process. And the results depend on the THz spectrum. For a general description on phase matching which is independent of THz source, only

the phase matching efficiency term in equation 5.16 is shown in figure 5.13. For practical purpose, a 500 μm ZnTe with 500 μm incident beam size and 7 degree THz angle are applied in the calculation. A thin crystal can provide a broader bandwidth response. Figure 5.13(a) shows the phase matching efficiency mapping with external emission angle and frequency. Three apertures are marked in the figure to show the restrictions on the acceptable angles. The dotted line, dashed line and straight line show the transmitted emission angles are between ± 0.02, ± 0.04, and ± 0.1 degree respectively. Their transmitted spectrum is shown in figure 5.13(b). In this case, the acceptable angles between ± 0.02, ± 0.04, and ± 0.1 degree show 2 THz, 4 THz and full 6 THz bandwidth (FWHM) respectively. Therefore an aperture in the optical transport system may limit the bandwidth of the measurements and leads to an broadening in bunch length measurement.

For a broad bandwidth probe, as used in EOSD system for example, the EO effect can be considered as the summation of each monochromatic component of the probe beam, which is a convolution of the probe spectrum and THz beam spectrum as shown in equation 2.59. Therefore the broad bandwidth probe leads to a spectrum broadening only in horizontal direction of figure 5.13(a), and the chirp rate keeps the same.

For a EO based bunch profile monitor, any misalignment between an optical probe and an e-bunch may induce the angular chirp on the emitted signal. For the EOSD bunch profile monitor on CALIFES, the probe laser is coupled into a fibre for detection. The fibre tolerance for this angle spatial dispersion can be calculated. From ZnTe crystal to a fibre coupler, 3 meters distance is supposed, which is similar with the EOSD system in CTF3. A fibre coupler (Thorlabs' F810FC-780) is used here, with $NA = 0.25$, $f = 36.01$ mm. The coupler is connected to a multi-mode fibre with $NA = 0.22$ and 50 μm core. Calculated by ray tracing matrix based on these parameters, the angular tolerance for the fibre coupling is the emission offset angle of 0.04 degree relative to the central axis after the ZnTe crystal. With this tolerance, a 1 THz signal from 7 degree THz-probe misalignment can be coupled into a fibre and a 2 THz signal is just on its limit. The beam size focused on fibre pupil is 24 um for a 2 mm incident beam. In another word, in order to measure bunch length of longer-than-0.5 ps, the misalignment between the bunch and probe laser has to be controlled within 7 degrees to avoid losing any frequency component. For the bunch length less than 0.5 ps, its frequency components over 2 THz will not be transported into the detection system.

5.6 Conclusion

The non-collinear incident beam plays a role on the emission angle of EO signal through beam size included phase matching process. A chirp rate of 2.7×10^{-3} THz^{-1} is measured for 4 mm ZnTe at 800 nm wavelength. For EOSD bunch profile measurement application, a non-collinear incident beam, by misalignment, will induce an angular chirp on the generated EO signal. This chirp may limit the bandwidth on fibre coupling, furthermore limit the resolution of measured bunch profile. This angular chirp need to be considered in the measurement and need to be reduced until it is compatible with the required resolution, spatially for long transfer line system.

Chapter 6

Conclusions and future perspectives

An electro-optic bunch profile monitor for the CLIC test facility (CTF3) has been developed, and the fundamental capabilities and limits of the system are investigated as part of the CLIC diagnostic development. The principle of the monitor is based on the non-invasive electro-optic spectral decoding technique, which while is not generally capable of the highest time resolution for CLIC design. It shares a common physical basis with other electro-optic techniques, investigations include signal to noise ratio, and frequency detection. Therefore it has a generic application to all EO systems. The EOSD system satisfies moderate time resolution requirements of CLIC, while also informing the expected capability of other EO-based techniques.

This thesis summarises frequency analysis approach of electro-optic effect based on $\chi^{(2)}$ frequency mixing process. This approach starts from Maxwell's equations, and ends with a general solution of wave equation for two broadband incident electric fields. Comparing to the classical refractive index approach, the effect and behaviour of the new generated frequency are clearly shown. The result can be used to describe not only the EO sampling setup, but also for signal-shot techniques. The application examples for EO sampling, EO spectral decoding and spectral upconversion are given. Specific for EOSD system, the final equations for both crossed polarization setup and balance detection setup in frequency domain including EO crystal angle, half-wave plate angle and quarter-wave plate angle are given. The dependence of the crystal angle and probe beam polarization orientation on the detection signal is shown, which can be used to guide the crystal implementation for bunch profile measurements. By offset the half-wave

plate angle, the detection signal from a crossed polarization setup includes a probe background term, a linear proportional to Coulomb field term and a quadratic to Coulomb field term. The roles of these three terms are studied. Based on the frequency approach, the limitation of the EOSD system is derived and its dependence on the original probe duration and chirped duration is given.

EOSD detection signals are estimated based on numerical calculations for four fibre laser options. The calculation results help us to decide a best scheme for measuring CALFIES bunch profile and show a 2.7 nJ probe beam, with initial 120 fs pulse duration chirped to 3 ps and 1 mm ZnTe, can generate a 9 pJ detection signal for measuring a 1.4 ps duration electron bunch with 1.6 MV/m field strength. The entire scheme of the EOSD bunch profile for CALFIES is described and its laser system, stretchers, the optical transfer line, the OTR transfer line, the two vacuum chambers, home-made spectrometer, the detection ICCD camera and the laser synchronization are shown in details. The bunch profile monitor for CALIFES beam line is implemented and commissioned at CERN. Since the CALIFES can only provide several picosecond long bunch at the implementation time, the monitor system is modified to measure longer bunch than the one designed for. The probe laser is chirped to 13.8 ps from 130 fs and 4 mm ZnTe crystal is installed. The monitor has a resolution of sub-picosecond and suitable for bunch longer than 3.5 ps with effective window of 16 ps. The system can be used to measure the bunch with 0.17 nC charge, 6 ps duration, at 2 mm offset position, and single shot measurement shows a signal to noise ratio of 28. The system can be modified to a better resolution system by applying thinner crystal and shorter laser pulse chirp duration.

Since the directly measured EOSD data is related to the probe laser spectrum intensity, all the measured data should be normalized by the probe spectrum. A demonstration on the relationship between the measured bunch profile and bunch charge is studied. Bunch length measurements are compared with streak camera measurements by measuring e-bunch generated OTR photons. Although the streak camera was not optimised for bunch length measurement, the corrected streak camera measured bunch lengths are consistent with the EOSD measurements. A deliberate offset half-wave plate induces all three of the background term, the linear term and the quadratic term in the measured data. Three methods were introduced to retrieval bunch Coulomb field value. The two-shot measurement of the three provides a quick retrieval process to obtain Coulomb field strength, meanwhile the least squared fitting method overcomes the systematic error and provides a precise result. The retrieved value, 1.3 MV/m, agrees with calculation result. The Coulomb field profile retrieved from the linear term shows

the original polarity of the field and its negative part of the field may imply the bunch wakefield.

A frequency-dependent EO signal emission angular chirp induced by two non-collinear incident beams at EO crystal is studied. In order to show this effect clearly and simply, the calculation and experiment are based on a quasi-monochromatic laser probe at 800 nm and a THz wave. Due to the beam size and incident beam angle included phase matching approach, the generated EO signal is angular chirped by frequency and the chirp rate is 2.6×10^{-3} THz^{-1} for a 4 mm ZnTe crystal with probe beam at 800 nm wavelength. Although the experiment is based on a quasi-monochromatic probe beam, the conclusion can be extended for a broadband probe by summing the contributions of all frequency components. This study can guide us on some detection issue of an EOSD bunch profile monitor. Due to this frequency dependent offset, part of frequency components may be missing in the signal coupling for detection. A case is calculated that for the bunch profile monitor in this thesis, 7 degree misalignment on the incident angle between the laser probe and Coulomb field may cause the frequency over 2 THz losing, which leads to a 0.5 ps time limitation.

For achieving a resolution of 20 fs rms, the future work can be focused on improving EO measurement resolution. The resolution is currently limited by the bandwidth of EO detection materials. A new EO material with 50 THz bandwidth can easily push the resolution down to 20 fs level. Or it may be also possible that find a method to combine different EO crystals which cover different frequency range. The key issue is to retrieve phase information from all crystals and combine them.

For narrowband laser, the spectral upconversion method can shift bunch spectrum up to nearby laser frequency, which is a new way to measure the bunch profile information. Its phase retrieval methods has been mentioned in Chapter 1. For broadband laser, a distortion will appear in EOSD-type bunch profile monitor if the measured bunch length is very short and an oscillation can be seen in the measured signal. This oscillation seems related to the short bunch length as well [45]. It becomes a question if the short bunch profile can be restored from the distorted signal.

Bibliography

[1] M. Aicheler(ed.), P. Burrows(ed.), M. Draper(ed.), T. Garvey(ed.), P. Lebrun(ed.), K. Peach(ed.), N. Phinney(ed.), H. Schmickler(ed.), D. Schulte(ed.), and N. Toge(ed.). A multi-TeV linear collider based on CLIC technology: CLIC conceptual design report. Technical report, CERN, CERN-2012-007.

[2] 2015. URL `http://ctf3-tbts.web.cern.ch/ctf3-tbts/images/`.

[3] 2015. URL `https://edms.cern.ch/ui/#!master/navigator/document?D:1456520639:1456520639:subDocs`.

[4] H. Braun, R. Corsini, J.-P. Delahaye, A. De Roeck, S. Doebert, G. Geschonke, A. Grudiev, C. Hauviller, B. Jeanneret, E. Jensen, T. Lefevre, Y. Papaphilippou, G. Riddone, L. Rinol, W.-D. Schlatter, H. Schmickler, D. Schulte, I. Syratchev, M. Taborelli, F. Tecker (editor), R. Tomas, S. Weisz, and W. Wunsch. CLIC 2008 parameters. CLIC-note-764, CERN, Switzerland, October 2008.

[5] G. Berden, W. A. Gillespie, S. P. Jamison, E.-A. Knabbe, A. M. MacLeod, A. F. G. van der Meer, P. J. Phillips, H. Schlarb, B. Schmidt, P. Schmuser, and B. Steffen. Benchmarking of electro-optic monitors for femtosecond electron bunches. *Physical Review Letters*, 99(164801), October 2007. doi: 10.1103/PhysRevLett.99.164801.

[6] K. L. F. Bane, F.-J. Decker, Y. Ding, D. Dowell, P. Emma, J. Frisch, Z. Huang, R. Iverson, C. Limborg-Deprey, H. Loos, H.-D. Nuhn, D. Ratner, G. Stupakov, J. Turner, J. Welch, and J. Wu. Measurements and modeling of coherent synchrotron radiation and its impact on the linac coherent light source electron beam. *Physical Review Special Topics - Accelerators and Beams*, 12(030704), March 2009. doi: 10.1103/PhysRevSTAB.12.030704.

[7] S.P. Jamison, G. Berden, A.M. MacLeod, B. Steffen, P. J. Phillips, and W.A. Gillespie. Femtosecond resolution bunch profile measurements. In *Proceedings of EPAC 2006*, page 915, Edinburgh, Scotland, 2006.

[8] D. Oepts and G.M.H. Knippels. Direct measurement of the shape of short electron bunches. In *Proceedings of the FEL*, 1998.

[9] X. Yan, A. M. MacLeod, W. A. Gillespie, G. M. H. Knippels, D. Oepts, A. F. G. van der Meer, and W. Seidel. Subpicosecond electro-optic measurement of relativistic electron pulses. *Physical Review Letters*, 85:3404, 2000.

[10] I. Wilke, A. M. MacLeod, W. A. Gillespie, G. Berden, G. M. H. Knippels, and A. F. G. van der Meer. Single-shot electron-beam bunch length measurements. *Physical Review Letters*, 88:124801, 2002.

[11] A. Azima, S. Dusterer, H. Schlarb, J. Feldhaus, A. Cavalieri, D. Fritz, and K. Sengstock. Jitter measurement by spatial electro-optical sampling at the flash free electron laser. In *Proceedings of EPAC 2006*, page 71, Edinburgh, Scotland, 2006.

[12] G. Berden, S. P. Jamison, A. M. McLeod, W. A. Gillespie, B. Redlich, and A. F. G. van der Meer. Electro-optic technique with improved time resolution for real-time, nondestructive, single-shot measurements of femtosecond electron bunch profiles. *Physical Review Letters*, 93:114802, 2004.

[13] S. P. Jamison, G. Berden, P. J. Phillips, W. A. Gillespie, and A. M. MacLeod. Upconversion of a relativistic coulomb field terahertz pulse to the near infrared. *Applied Physics Letters*, 96:231114, 2010.

[14] Wilfrid Farabolini, Franck Peauger, Roberto Corsini, Davide Gamba, Alexej Grudiev, Muhammad Asif Khan, Stefano Mazzoni, Jose Luis Navarro Quirante, Rui Pan, Jack Raymond Towler, Niki Vitoratou, Kashif Yaqub, Christopher Borgmann, Jim Oegren, and Roger Ruber. Recent results from ctf3 two beam test stand. In *Proceedings of IPAC2014, Dresden, Germany*, 2014.

[15] J. Brossard, M. Desmons, B. Mercier, C. Prevost, and R. Roux. Construction of the probe beam photo-injector of ctf3. In *Proceedings of the EPAC 2006*, page 828, Edinburgh, Scotland, 2006.

[16] M.Divall Csatari, A.Andersson, B.Bolzon, E.Bravin, E.Chevallay, S.Dobert, A.Drozdy, V.Fedosseev, C. Hessler, T.Lefevre, S.Livesley, R.Losito, O. Mete, M.Petrarca, and A.N.Rabiller. Fast phase switching within the bunch train of the phin photo-injector at cern using fiber-optic modulators on the drive laser. *Nuclear Instruments and Methods in Physics Research*, A659:1–8, 2011.

[17] K. Honkavaara, Ph. Piot, S. Schreiber, and D. Sertore. Bunch length measurements at the tesla test facility using a streak camera. In *the 2001 Particle Accelerator Conference*, 2001.

[18] Yukio Shibata, Kimihiro Ishi, Toshiharu Takahashi, Toshinobu Kanai, Fumitaka Arai, Shin ichi Kimura, Toshiaki Ohsaka, Mikihiko Ikezawa, Yasuhiro Kondo, Ryukou Kato, Shigekazu Urasawa, Toshiharu Nakazato, Satoshi Niwano, Masahiro Yoshioka, and Masayuki Oyamada. Coherent transition radiation in the far-infrared region. *Physical Review E*, 49(1), January 1994.

[19] Chitrlada Settakorn. Generation and use of coherent transition radiation from short electron bunches. Technical report, Stanford Linear Accelerator Center and Stanford University, Stanford, CA 94309, 2001.

[20] B. Feng, M. Oyamada, F. Hinode, S. Sato, Y. Kondo, Y. Shibata, and M. Ikezawa. Electron bunch shape measurement using coherent diffraction radiation. *Nuclear Instruments and Methods in Physics Research A*, 475: 492–497, 2001.

[21] M. Castellano, V. A. Verzilov, L. Catani, A. Cianchi, G. Orlandi, and M. Geitz. Measurements of coherent diffraction radiation and its application for bunch length diagnostics in particle accelerators. *Physical Review E*, 63 (056501), 2001. doi: 10.1103/PhysRevE.63.056501.

[22] Dao Xiang and Yuantao Ding. Longitudinal-to-transverse mapping for femtosecond electron bunch length measurement. *Physical Review Special Topics - Accelerators and Beams*, 13(094001), September 2010. doi: 10.1103/PhysRevSTAB.13.094001.

[23] Wilfrid Farabolini, Claire Simon, Franck Peauger, Aline Curtoni, Daniel Bogard, Patrick Girardot, Marta Csatari, Nathalie Lebas, Massimo Petrarca, Eric Chevallay, Roger Ruber, Andrea Palaia, and Volker Ziemann. Ctf3 probe beam linac commissioning and operations. In *Proceedings of Linear Accelerator Conference LINAC2010*, page 46, Tsukuba, Japan, 2010.

[24] Y. Ding, C. Behrens, P. Emma, J. Frisch, Z. Huang, H. Loos, P. Krejcik, and M-H. Wang. Femtosecond x-ray pulse temporal characterization in free-electron lasers using a transverse deflector. *Physical Review Special Topics - Accelerators and Beams*, 14(120701), 2011. doi: 10.1103/PhysRevSTAB.14.120701.

[25] S.P. Jamison, G. Berden, A.M. MacLeod, D.A. Jaroszynski, B. Redlich, A.F.G. van der Meer, and W.A. Gillespie. Electro-optic techniques for temporal profile characterisation of relativistic coulomb fields and coherent synchrotron radiation. *Nuclear Instruments and Methods in Physics Research Section A*, 557:305, 2005. doi: 10.1016/j.nima.2005.10.090.

[26] X. Yang, T. Tang, T. Rao, J.B. Murphy, Y. Shen, and X.J. Wang. Electron bunch length monitors using spatially encoded electro-optical technique in an orthogonal configuration. *Applied Physics Letters*, 95:December, 2009.

[27] B. Steffen, V. Arsov, G. Berden, W. A. Gillespie, S. P. Jamison, A. M. MacLeod, A. F. G. van der Meer, P. J. Phillips, H. Schlarb, B. Schmidt, and P. Schmuser. Electro-optic time profile monitors for femtosecond electron bunches at the soft x-ray free-electron laser flash. *Physical Review Special Topics - Accelerators and Beams*, 12:032802, 2009.

[28] Bernd Steffen, Sara Casalbuoni, Peter Schmuser, Stefan Simrock, Manfred Tonutti, Axel Winter, Timo Korhonen, Thomas Schilcher, Volker Schlott, Hans Sigg, and Daniel Suetterlin. Bunch length measurements at the sls linac using electro optical sampling. In *Proceedings of the 2004 FEL Conference*, 2004.

[29] M. J. Fitch, A. C. Melissinos, P. L. Colestock, J.-P. Carneiro, H. T. Edwards, and W. H. Hartung. Electro-optic measurement of the wake fields of a relativistic electron beam. *Physical Review Letters*, 87(3):034801, 2001. doi: http://dx.doi.org/10.1103/PhysRevLett.87.034801.

[30] A. L. Cavalieri, D. M. Fritz, S. H. Lee, P. H. Bucksbaum, D. A. Reis, J. Rudati, D. M. Mills, P. H. Fuoss, G. B. Stephenson, C. C. Kao, D. P. Siddons, D. P. Lowney, A. G. MacPhee, D. Weinstein, R. W. Falcone, R. Pahl, J. Als-Nielsen, C. Blome, S. Dsterer, R. Ischebeck, H. Schlarb, H. Schulte-Schrepping, Th. Tschentscher, J. Schneider, O. Hignette, F. Sette, K. Sokolowski-Tinten, H. N. Chapman, R. W. Lee, T. N. Hansen, O. Synnergren, J. Larsson, S. Techert, J. Sheppard, J. S. Wark, M. Bergh, C. Caleman, G. Huldt, D. van der Spoel, N. Timneanu, J. Hajdu, R. A. Akre, E. Bong, P. Emma, P. Krejcik, J. Arthur, S. Brennan, K. J. Gaffney, A. M. Lindenberg, K. Luening, , and J. B. Hastings. Clocking femtosecond x rays. *Physical Review Letters*, 94:114801, 2005. doi: http://dx.doi.org/10.1103/PhysRevLett.94.114801.

[31] H. Tomizawa, K. Ogawa, and et al. The first demonstration of eos 3d-bcd monitor to maximize 3d-overlapping for hhg-seeded fel. In *Proceedings of IBIC2013, Oxford, UK*, 2013.

[32] P.J. Phillips, W.A. Gillespie, and S.P. Jamison. Electro-optic diagnostics on the daresbury energy recovery linac. In *Proceedings of EPAC 2006, Edinburgh, Scotland*, 2006.

[33] R. Pan, A. Andersson, W. Farabolini, A.N. Goldblatt, T. Lefevre, M. Martyanov, S. Mazzoni, L. Timeo, S.Rey, S. P. Jamison, W. A. Gillespie, and D. Walsh. Electro-optical bunch profile measurement at ctf3. In *Proceedings of IPAC2013, Shanghai, China*, 2013.

[34] Vincent De Waelea, Uli Schmidhammera, Jean-Raphal Marqus, Hugues Monarda, Jean-Philippe Larbrea, Nicolas Bourgeois, and Mehran Mostafavia. Non-invasive single bunch monitoring for ps pulse radiolysis. *Radiation Physics and Chemistry*, 78:1099, 2009. doi: 10.1016/j.radphyschem.2009.06.027.

[35] C. M. Scoby, P. Musumeci, J. T. Moody, and M. S. Gutierrez. Electro-optic sampling at 90 degree interaction geometry for time-of-arrival stamping of ultrafast relativistic electron diffraction. *Physical Review Special Topics - Accelerators and Beams*, 13:022801, 2010. doi: http://dx.doi.org/10.1103/PhysRevSTAB.13.022801.

[36] M. Veronese, M. Danailov, and M. Ferianis. The electro-optic sampling stations for fermi@elettra, a design study. In *Proceedings of BIW08, Tahoe City, California*, 2008.

[37] R. Pompilia, A. Cianchib, Alesinia, M.P. Ananiaa, A. Baccic, M. Bellavegliaa, M. Castellanoa, E. Chiadronia, D. Di Giovenalea, G. Di Pirroa, G. Gattia, F. Giorgiannid, M. Ferrarioa, S. Lupid, F. Massimod, A. Mostaccia, A.R. Rossic, C. Vaccarezzaa, and F. Villaa. First single-shot and non-intercepting longitudinal bunch diagnostics for comb-like beam by means of electro-optic sampling. *Nuclear Instruments and Methods in Physics Research Section A*, 740:216, 2014. doi: 10.1016/j.nima.2013.10.031.

[38] A. Borysenko, E. Hertle, N. Hiller, V. Judin, B. Kehrer, S. Marsching, A.-S. Mller, M. J. Nasse, R. Rossmanith, R. Ruprecht, M. Schuh, M. Schwarz, and P. Wesolowski. Electro-optical bunch length monitor for flute: layout and simulations. In *Proceedings of IPAC2014, Dresden, Germany*, 2014.

[39] Q. Wu and X.-C. Zhang. Free-space electro-optic sampling of terahertz beams. *Applied Physics Letters*, 67:3523, December 1995.

[40] M. J. Fitch, A. C. A. C. Melissinos, and L. Colestock. Picosecond electron bunch length measurement by electro-optic detection of the wakefield. In *Proceedings of the 1999 Particle Accelerator Conference*, 1999.

[41] A. Galvanauskas, J. A. Tellefsen, A. Krotkus, M. Oberg, and B. Broberg. Real-time picosecond electro-optic oscilloscope technique using a tunable semiconductor laser. *Applied Physics Letters*, 60(2):145, January 1991. doi: 10.1063/1.107456.

[42] Z. Jiang and X.-C. Zhang. Electro-optic measurement of thz field pulses with a chirped optical beam. *Applied Physics Letters*, 72(16):1945, February 1998. URL `http://dx.doi.org/10.1063/1.121231`.

[43] Zhiping Jiang and X.-C. Zhang. Single-shot spatiotemporal terahertz field imaging. *Optics Letters*, 23(14), July 1998.

[44] J. R. Fletcher. Distortion and uncertainty in chirped pulse thz spectrometers. *Optics Express*, 10(24):1425, 2002. doi: http://dx.doi.org/10.1364/OE.10.001425.

[45] S.P. Jamison, G. Berden, W.A. Gillespie, P.J. Phillips, and A.M. MacLeod. Limitations of electro-optic measurements of electron bunch longitudinal profile. In *Proceedings of EPAC08*, page 1149, Genoa, Italy, 2008.

[46] Jie Shan, Aniruddha S. Weling, Ernst Knoesel, Ludwig Bartels, Mischa Bonn, Ajay Nahata, Georg A. Reider, and Tony F. Heinz. Single-shot measurement of terahertz electromagnetic pulses by use of electro-optic sampling. *Optics Letters*, 25(6), March 2000.

[47] T. Srinivasan-Rao, M. Amin, V. Castillo, D. M. Lazarus, D. Nikas, C. Ozben, Y. K. Semertzidis, A. Stillman, T. Tsang, and L. Kowalski. Novel single shot scheme to measure submillimeter electron bunch lengths using electro-optic technique. *Physical Review Special Topics - Accelerators and Beams*, 5:042801, 2002. doi: 10.1103/PhysRevSTAB.5.042801.

[48] Steven P. Jamison, Jingling Shen, A.M. MacLeod, W.A. Gillespie, and D. A. Jaroszynski. High-temporal-resolution, single-shot characterization of terahertz pulses. *Optics Letters*, 28(18), September 2003.

[49] G. Berden, A.F.G. van der Meer, S. P. Jamison, B. Steffen, E.-A. Knabbe, B. Schmidt, P. Schmuser, A.M. MacLeod, P. J. Phillips, and W.A. Gillespie.

Single shot longitudinal bunch profile measurements at flash using electro-optics techniques. In *Proceedings of EPAC 2006*, 2006.

[50] J. van Tilborg, D.J. Bakker, N.H. Matlis, and W.P. Leemans. Spectral sidebands on a narrow-bandwidth optical probe as a broad-bandwidth thz pulse diagnostic. *Optics Express*, 19(27), December 2011.

[51] M. H. Helle, D. F. Gordon, D. Kaganovich, and A. Ting. Extending electro-optic detection to ultrashort electron beams. *Phys. Rev. ST Accel. Beams*, 15:052801, 2012. doi: http://dx.doi.org/10.1103/PhysRevSTAB.15.052801.

[52] D.A. Walsh, W.A. Gillespie, and S.P. Jamison. A femtosecond resolution electro-optic diagnostic using a nanosecond-pulse laser. In *Proceedings of IBIC2013, Osxford, UK*, 2013.

[53] Jan-Patrick Schwinkendorf, Steffen Wunderlich, Lucas Schaper, Bernhard Schmidt, and Jens Osterhoff. Tadpole for longitudinal electron-bunch diagnostics based on electro-optic upconversion. *Nuclear Instruments and Methods in Physics Research Section A*, 740:222, 2014. doi: 10.1016/j.nima.2013.12.030.

[54] Axel Winter, F. Omer Ilday, and B. Steffen. Femtosecond yb-doped fiber laser system at 1 m of wavelength with 100-nm bandwidth and variable pulse structure for accelerator diagnostics. In *Proceedings of DIPAC 2007, Venice, Italy*, 2007.

[55] B. Steffen, V. Schlott, and F. Muller. A compact single shot electro-optical bunch length monitor for the swissfel. In *Proceedings of DIPAC09, Basel, Switzerland*, 2009.

[56] Jonas Breunlin. Commissioning of an electro-optic electron bunch length monitor at flash. Master's thesis, University Hamburg, 2011.

[57] F. Muller, P. Peier, V. Schlott, B. Steffen, T. Feurer, and P. Kuske. Electro-optical measurement of sub-ps structures in low charge electron bunches. *Physical Review Special Topics - Accelerators and Beams*, 15:070701, 2012. doi: 10.1103/PhysRevSTAB.15.070701.

[58] H. Tomizawa, H. Hanaki, and T. Ishikawa. Non-destructive single-shot 3-d electron bunch monitor with femtosecond-timing all-optical system for pump & probe wxperiments. In *Proceedings of FEL2007, novosibirsk, Russia*, 2007.

[59] H. Tomizawa, S. Matsubara, H. Dewa, A. Mizuno, T. Taniuchi, K. Yanagida, and H. Hanaki. Novel nondestructive shot-by-shot monitor to measure 3d

bunch charge distribution with femtosecond eo-sampling. In *Proceedings of FEL 2010*, Malmo, Sweden, 2010.

[60] H. Tomizawa, K. Ogawa, and et al. Non-destructive real-time monitor to measure 3d-bunch charge distribution with arrival timing to maximize 3d overlapping for hhg-seeded euv-fel. In *Proceeding of LINAC2012, Tel-Aviv, Israel*, 2012.

[61] Q. Chen, M. Tani, Zhiping Jiang, and X.-C. Zhang. Electro-optic transceivers for terahertz-wave applications. *Journal of the Optical Society of America B*, 18:823, 2001. doi: http://dx.doi.org/10.1364/JOSAB.18.000823.

[62] Lionel Duvillaret, Stphane Rialland, and Jean-Louis Coutaz. Electro-optic sensors for electric field measurements. ii. choice of the crystals and complete optimization of their orientation. *Journal of the Optical Society of America B*, 19:2704, 2002. doi: http://dx.doi.org/10.1364/JOSAB.19.002704.

[63] Nick C. J. van der Valk, Tom Wenckebach, and Paul C. M. Planken. Full mathematical description of electro-optic detection in optically isotropic crystals. *Journal of the Optical Society of America B*, 2004.

[64] S. Casalbuoni, H. Schlarb, B. Schmidt, P. Schmser, B. Steffen, and A. Winter. Numerical studies on the electro-optic detection of femtosecond electron bunches. *Physical Review Special Topics - Accelerators and Beams*, 11: 072802, 2008. doi: http://dx.doi.org/10.1103/PhysRevSTAB.11.072802.

[65] G. Gallot and D. Grischkowsky. Electro-optic detection of terahertz radiation. *Journal of the Optical Society of America B*, 16(8):1204, 1999. doi: http://dx.doi.org/10.1364/JOSAB.16.001204.

[66] S. P. Jamison, A. M. MacLeod, G. Berden, D. A. Jaroszynski, and W. A. Gillespie. Temporally resolved electro-optic effect. *Optics Letters*, 31:1753, 2006.

[67] S.P. Jamison. The electro-optic effect for intense terahertz pulses. *Applied Physics B*, 91:241, 2008.

[68] J. D. Jackson. *Classical Electrodynamics*. John Wiley and Sons, Inc., 3rd edition, 1999.

[69] Robert W. Boyd. *Nonlinear Optics*. Academic Press, 3rd edition, April 2008. Chapter 2.

[70] Bernd Richard Steffen. *Electro-optic methods for longitudinal bunch diagnostics at FLASH*. PhD thesis, Hamburg University, 2007.

[71] S.P. Jamison, G. Berden, A. M. MacLeod, JinglJingling Shen, D.A. Jaroszynski, B. Redlich, A.F.G. van der meer, and W. A. Gillespie. Temporal limitations of single-shot electro-optic thz detection techniques. Unpublished, 2006.

[72] A. Yariv. *Quantum electronics*. John Wiley and Sons, Inc., 2nd edition, 1989.

[73] G. Bernden, G. Knippels, A.F.G. van der Meer D. Oepts, S.P. Jamison, X. Yan, A.M. MacLeod, W.A. Gillespie, J.L. Shen, and I. Wilke. Chirped-laser based electron bunch length monitor. In *Proceedings of the PAC 2003*, page 519, 2003.

[74] Schott optical glass data sheets 2012-12-04, 2012.

[75] Javier Alda. Laser and gaussian beam propagation and transformation. *Encyclopedia of optical engineering*, pages 999–1013, 2003.

[76] D. A. Walsh, M. J. Cliffe, R. Pan, E. W. Snedden, D. M. Graham, W. A. Gillespie, and S. P. Jamison. Role of misalignment-induced angular chirp in the electro-optic detection of thz waves. *Optics Express*, 22(10):12028–12037, 2014. URL `http://dx.doi.org/10.1364/OE.22.012028`.